Abstract

One of the third-generation solar cell concepts is the intermediate band solar cells (IBSCs), which are based on a new type of semiconductor materials, that has an intermediate band (IB) within the forbidden band gap. IBSCs have a simple structure and a theoretical efficiency 50% higher than conventional single-junction solar cells. A challenge in the realization of IBSCs is to develop sustainable IB materials. At NTNU, our group is researching titanium oxide, TiO_2, as the basis for IB-materials, and the aim is to fabricate doped TiO_2 as thin films. It is known that high-quality TiO_2 can be achieved on $LaAlO_3$ (LAO) substrates.

This work is based on work of a previous master student [1], who studied the LAO surfaces. He found that the LAO substrates are not atomically flat due to the twin formation during the substrate fabrication. The LAO surface is thus very inhomogeneous, and it is interesting to find out if the local topography affects the topography of the TiO_2 films. I have studied the surface of a set of seven TiO_2 films grown on $LaAlO_3$(LAO) and on other substrates. I studied the surface by using the 3D Optical Profiler and atomic force microscope (AFM). By combining the two techniques I could image the same location on the film, from the nm to the mm scale. I could image the whole film on the 10 x 10 mm^2 substrates as well as terraces in the TiO_2 film on the nm scale. I also used the 3D optical profiler to image TiO_2 films deposited on other substrates; $SrTiO_3$(STO), sapphire, and silicon substrates.

The 3D Optical Profiler images showed, as expected, that the films on the STO, Si and sapphire substrates were very flat, compared to the films on LAO. From the 3D Optical profiler images of the films on LAO we defined three types of topographies; twinned, flat, and mixed, that originated from the LAO twin domains formed during preparation and annealing of the substrates. For two of the TiO_2 films, deposited for low and high oxygen partial pressure, I studied the films surface topography using AFM, sample B1 and B5, respectively.

From the AFM images of B1 I saw a high density of hillock-like features protruding out of the films, while the B5 film had a flatter topography, clearly showing terraces of various widths. From the AFM images, I obtained values for the average and RMS roughness of the B1 and B5 films, for twinned, flat and mixed regions in the films, to investigate if the roughness varied with the LAO substrate topography. From the data it seems like there is no big difference in the topography of the TiO_2 film depending on the local topography of the LAO substrates. I could see some variation in the roughness, but the variation seems not to depend on the location/region, i.e., the roughness could vary a similar amount within each region, and no so much from region to region. For the two films investigated the difference in roughness is caused by the difference in the deposition parameters.

Preface

This thesis is submitted to the Norwegian University of Science and Technology (NTNU) to fulfill the Master of Science degree in Physics.

First of all, I appreciate my supervisor, professor Turid Reenaas, with all of my heart, who accepted me in her research group, teaches me, and guides me with kind encouragement. Without her irreplaceable help, I would have never completed this journey. I also would like to thank Thomas Vågenes Brakstad, Marina Jorge, and Hogne Lysne for their precious help during this work. I have learned some techniques – characterization of samples at NTNU NanoLab, and I would like to thank all of the engineers that have helped me in my training.

I want to thank my dad. You are the one who makes me feel that even if no one thinks that I am good enough, I am the best in your eyes. I am also very grateful to my sister Yuna, brother-in-law Dongwook, lovely niece Dan, and all of my family members. I would also like to thank all of my friends in Trondheim, Korea or other places for being with me in all the difficult times during the journey of my Master's in Physics.

Thanks to God and praise to Jesus, who has blessed me and has given me the spirit and the ability to complete the thesis.

Thank you all for your unwavering support.

<div align="center">

2021 summer

Han Na Choi

</div>

Table of Contents

1 Introduction

1.1 Use of fossil fuels has negative consequences

In the summer of 2020, earth experienced abnormal weather phenomena. Due to the heatwave, it was recorded that the temperature in Siberia was 38°C[2]. Earth experienced strange weather phenomena. Due to the heatwave, it was recorded that the temperature in Siberia was 38°C [3]. Many Asian countries suffered from heavy deluges. India had three times the amount of rainfall compared to 2019; in China, many rivers and lakes swelled to record-high levels because of heavy rain. Also, Japan recorded the most significant precipitation during the last three decades. [4] Similar events have happened more and more frequently in the previous decade; all these natural phenomena are a horrifying threat for millions of people and for nature.

Climate change is no longer a distant story told by books, the media, or a handful of scientists; it is happening right here, right before our very eyes.

It is common knowledge that climate change is the increase in the greenhouse effect due to man-made carbon dioxide emissions, and the main reason is the use of fossil fuels. Moreover, the emissions from the use of fossil fuels can also affect air pollution. According to the World Health Organization (WHO), air pollution alone led to 4.2 million deaths in 2016.[5]

Climate change and pollution, together with fossil fuels being a non-renewable energy source, have led to people not using fossil fuels directly.

1.2 Necessity of increased use of solar energy.

The study of renewable energy, which can replace fossil fuels, has been researched for decades. There are many types of renewable energy, but this masterwork is related to the use of solar energy in solar cells. As illustrated in Figure 1, the sun supplies a massive amount of energy every year compared to other energy sources. It is a renewable energy source with the most significant potential. [6]

A solar cell converts solar energy directly into electricity, and currently, 713970 MW of the annual electricity generation is from solar cells[7]. It would be a great boost if the power could be increased.

Meanwhile, the study of solar cells has been continued; the efficiency of commercialized solar panels is around 20~30%, which is not enough for electricity demand. The amount of solar energy lost every day is tremendous, and it is a shame that we cannot use it.

1.3 Solution: third-generation solar cells

Solar cells can be classified into three generations. Every generation of solar cells is pursued at low cost and high efficiency, but it aims for more efficiency at the beginning. So, the first-generation solar cells used single crystal silicon. Although it was expensive, it

has better efficiency than the 2nd generation solar cells. After the 2nd generation, the focus was shifted to low cost, which resulted in the use of multi-crystalline silicon, so it was cheaper than the 1st one; but of course, it was less efficient. The 1st and 2nd generation solar cells have been studied intensively. Finally, the price is much lower, and the efficiency is much higher than before; and the technology has almost reached the ideal values, at least in the lab. However, there is a limit for using a single bandgap in a solar cell, and the efficiency maximum is achieved roughly at 33%. People want to increase the efficiency even more and decrease the cost of the electricity. Therefore, the 3rd generation solar cells have emerged for higher efficiency and lower electricity price than the first and second generation solar cells. To use enough solar energy to remove the need for fossil energy, the study of 3rd generation solar cells should be accelerated. The expected efficiency limit for the 3rd generation solar cells is just under 70%. However, this result can be seen only in the lab work, so the study should be maintained.
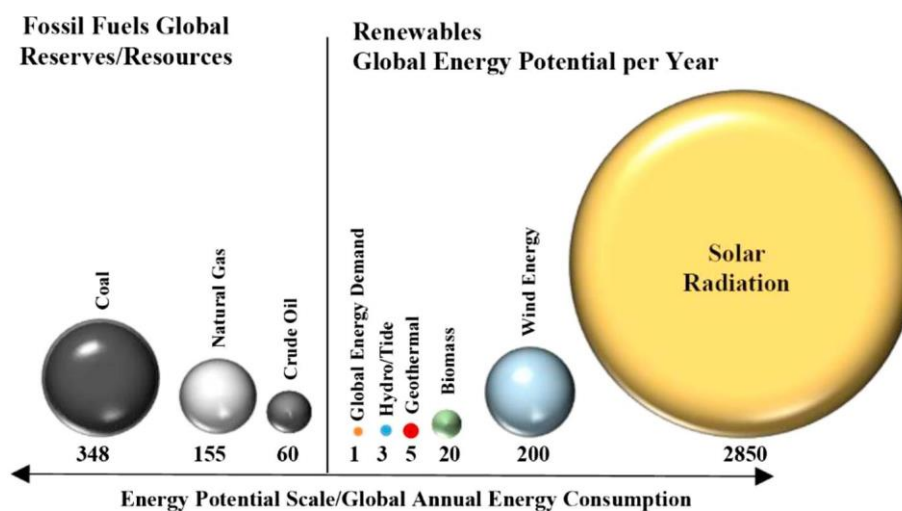

Figure 1.1. potential of the renewables and fossil fuels compared to energy demand.[6]

1.4 Focus on Intermediate Band Solar Cells (IBSCs) at NTNU

In this project, we at NTNU focus on IBSCs. Among the 3rd generation solar cells, multi-junction cells (tandem cells) are actively researched. Multi-bandgap solar cells use more layers to make the multi-junction absorb more solar spectrum than the single bandgap so that the efficiency will rise. However, due to its complex structure, it might be costly; moreover, it also has toxic materials such as P or Ga.[8]

On the other hand, IBSCs are simple structures compared to other tandem cells. Its structure is such that between conduction band (CB) and Valence band (VB), intermediate band (IB) is inserted, which can absorb more of the spectrum compared to conventional single junction solar cells. The IB can increase efficiency, and the materials should be sustainable; stable, non-harmful for both humans and nature, abundant, economical, and feasible.

The multi-junction solar cells' efficiency is roughly 50%, and this has reached almost 65% of the ideal lab results; however, IBSCs cannot be reached like other multi-junction solar cells. So, we at NTNU want to study further on IBSCs, which are more simple structures, cheaper, and non-toxic than other multi-junction solar cells.

2

1.5 This project is a small piece of the big puzzle.

This master work studies TiO_2 films on diverse substrates (LAO, STO, sapphire, and silicon) and characterizes surface features of the films. Our team found that it might be possible to link the sub mm to cm scale images of the 3D Optical Profiler with the nm to sub-mm AFM images in a previous work.[1] These ideas were carried out by me. Mainly, the project focuses on the topography and properties of TiO_2 films on LAO substrates. Therefore, an aim for this project was to link the measurement of the AFM and the 3D Optical Profiler. Then we could measure the film properties on a macroscopic location that could be identified using the 3D optical profiler, to see if the growth of the TiO_2 was affected by the substrate topography or not.

This study is a small piece in a big puzzle of the research on TiO_2 as a suitable material for IBSCs. Although this project is not directly searching for appropriate materials for IBSCs, it is a small contribution in understanding growth of TiO_2 on LAO.

1.6 Outline of thesis

In Chapter 2, the experimental techniques are briefly presented and in chapter 3, the basic properties of TiO_2 and the substrates. The experimental details are found in chapter 4 and the results are presented and discussed in chapter 5. In chapter 6, the thesis will be concluded; and lastly, future work will be suggested in chapter 7.

2 Experimental techniques

This chapter introduces the techniques used for the fabrication and characterization of the samples studied.

2.1   Fabrication tool

2.1.1 Pulsed Laser Deposition (PLD)

Pulsed Laser Deposition is a technique for film growth and is a physical vapor deposition (PVD) method. PLD has proven itself to be very good to deposit oxide thin films.[9-11] Figure 2.1 illustrates the schematics of PLD: a high-power pulsed laser (external laser) is shot on the target material to evaporate or vaporize it. High laser energy density creates a plasma plume by ablating the material of the target and exciting it to a plasma. After that, the ablated plume moves toward the substrate quickly (normally ~4µs) to be deposited. The film properties depend on the deposition parameters, especially the substrate temperature, but also the laser parameters and the use of a process gas, oxygen for oxides. Crystalline films can be made on suitable (lattice matched substrates). [10]
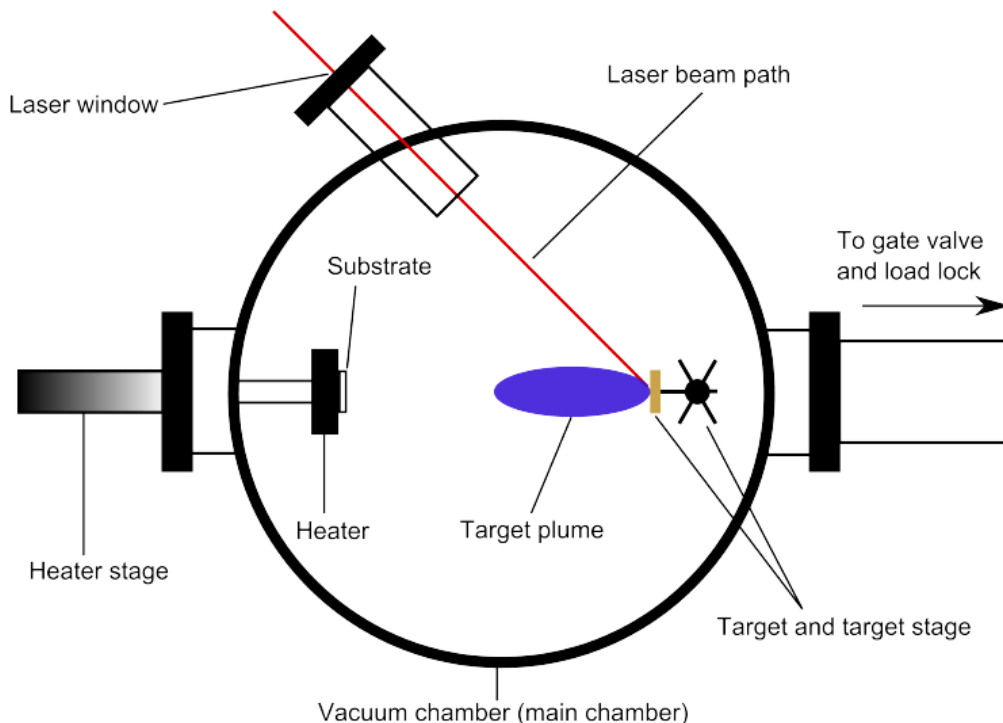
Fig.2.1. Schematic diagram of a PLD setup. The external source (laser) hits the target in a vacuum chamber; thereby, the plasma plume is made and deposited on a substrate.[12]

In PLD, a background gas is often used for two purposes. First, it plays the role of a reactive species, for instance, molecular oxygen for oxide. Lastly, to reduce the kinetic energies of the ablated species, the background gas is also used. The surrounding background gas is compressed by the vapor formed by laser ablation. The condensed gas results in the formation of a shock wave. The ablation plume expansion has slowed the interaction with the ambient.[13]

As I have mentioned above, PLD has some attractive properties for complex material-growing films. The first is that PLD can be actualized to transfer stoichiometric materials and ablated material from multication targets for various materials. Because it is absorbed by high laser energy density, it can occur from the nonequilibrium nature of the ablation process itself. Furthermore, it is able to create films quickly. Secondly, it is a simple structure, which means that it is easy to handle because of the laser source located outside the reaction chamber compared to other methods. Lastly, during the deposition, the fluence plays a crucial role in layer formation; therefore, it can be grown to epitaxial films and adhere at a lower temperature than other processes.[10, 14]

On the other hand, PLD has disadvantages - particulate deposition on the surface or splashing is the main problem. Breaking of surfaces because of thermal shock and liquid material splashing because of surface superheating are two prominent cases during particle formation when laser vaporizes. There are three methods for solving them: firstly, it can be used to filter the mechanical particle that composed a velocity selector. The filter plays the role of a high-velocity pass filter to remove slow-moving particulates. The second method is that the surface of the target is made smooth, such as polishing the target surface, to improve effectiveness. Lastly, it can be used to lower energy density and deposition rate.[13]

Another problem is that we cannot know the behavior inside of the plume, so it is tough to control the plume. Therefore, it might cause a lack of uniformity over a large area on the film. However, Rastering the laser on the substrate can be fixed by rotation and translation in an engineered vast area scale-up.[13, 14]

2.2 Characterization tool

2.2.1 3D Optical Profiler

This characterization tool serves as a non-contact, rapid, and reproducible technique to measure accurate surface topography, including shape, waviness, and roughness. Firstly, a significant advantage is that it is easy to measure even large-scale areas, up to 150mm*150mm, using stitching function. Secondly, it can maintain a sub-nanometer vertical resolution with a 0.1 nanometer RMS (Root Means Square) repeatedly, regardless of the field of view or magnification. Lastly, it can also provide scan speeds up to 100 microns per second vertically, with the entire area of view image in a fraction of a second.[15]

Figure 2.2 shows a schematic diagram of the 3D Optical Profiler. The 3D optical profiler uses white light interferometry (WLI). The interferometer is a device that splits a beam from a single source into two beams and then recombines them to make an interference pattern. The combined pattern results from the difference in the path of the two beams

traveled. Lastly, the charge-coupled device(CCD) camera captures the image of the interferogram using the imaging lens.
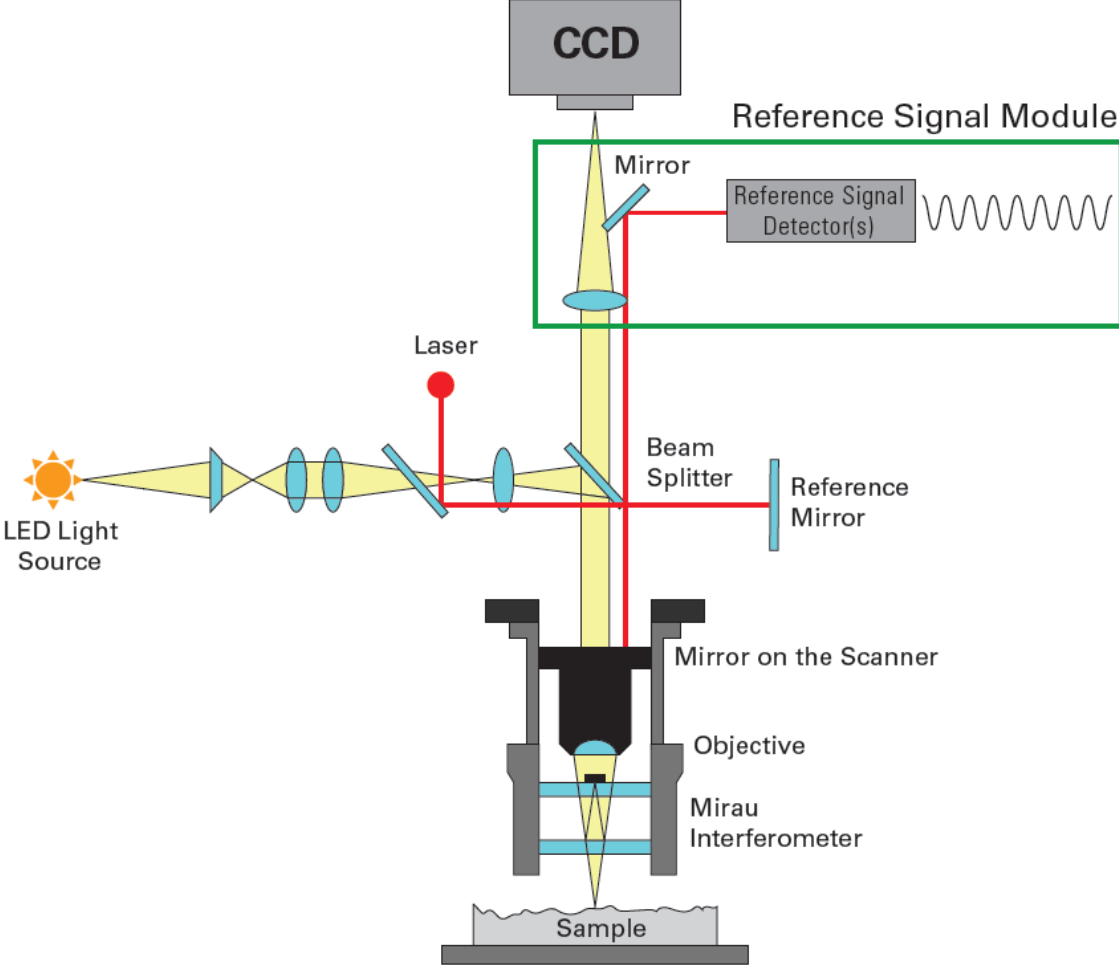
Figure 2.2. Schematic diagram of 3D Optical Profiler[15]

2.2.2 Atomic Force Microscopy (AFM)

In 1985, Binning, Quate, and Gerber explained Atomic Force Microscopy (AFM), a high-resolution non-optical imaging technique. After that, it was developed for surface analysis as a powerful measurement tool. The tool can be non-destructive and can make accurate measurements of the topographical, electrical, magnetic, chemical, optical, or mechanical features of the sample surface with very high resolution in air, liquids, or ultrahigh vacuum.[16]

AFM is a kind of SPM (Scanning Probe Microscope) that scans through a probe. The probe is moved up and down by the Van Der Waals force, which varies depending on the interaction or the distance between the probe and the sample. A microscope measures the atomic structure and shape of the surface by measuring the force between atoms when an insulated fine probe is brought close to the surface of an insulating sample to the microscopic size of an atomic unit. Unlike STM or SEM, it is not related to the movement of electrons, so there is no need to deposit metal on the sample surface, and no vacuum device is required.

In addition, the shape of the sample can be accurately measured in both horizontal and vertical directions, and the physical and electrical properties of the sample can also be found. The magnification can be up to tens of millions of times compared to the maximum of several thousand times from that of an optical microscope and hundreds of thousands of times from that of an electron microscope, enabling detailed observation of individual atoms.

Van Der Waals Force refers to the attraction or repulsive force between molecules or parts within a molecule, not between covalent bonds or electrical interactions of ions in physical chemistry. In other words, when an instantaneous dipole is formed by the movement of electrons in a nonpolar molecule, the molecule next to it is also temporarily polarized, and an induced dipole is created. The attraction between the instantaneous dipole and the induced dipole is called the van der Waals force.

The Van Der Waals Force acts as a repulsive force and attractive force depending on the distance between the cantilever and the sample surface. The closer the distance, the stronger the repulsive force, and the greater the distance, the greater the attraction force. AFM also has different modes depending on what kind of force is applied. There are three modes: contact mode, non-contact mode, and tapping mode, depending on the tip type.

In this project, tapping mode was used.

Tapping mode is a method designed to minimize the damage to the sample that occurs in the non-contact mode. It has the advantage of obtaining the exact resolution as the contact mode in samples with a significant surface height difference or easily damaged samples without damaging the sample by giving a certain vibration to the tip.[17]
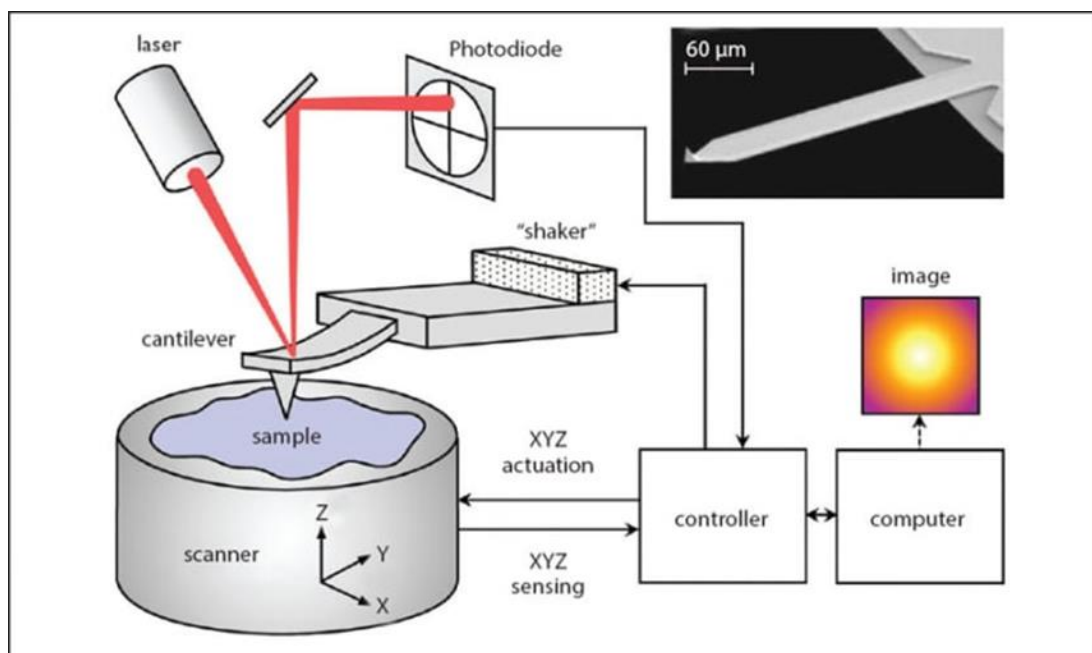
Figure 2.3. Schematic of AFM components. The right upper image is SEM image of a cantilever.[18]

3 Materials

This section presents the properties of substrate materials for LAO, STO, Sapphire and Silicon, and titanium dioxide as films.

3.1 Substrates

3.1.1 Lanthanum Aluminate_LaAlO$_3$ (LAO)

Lanthanum Aluminate (LAO) is commonly used substrates as epitaxial growing oxide thin films since it has resembling structures and fewer mismatches with lattice constant for some oxides. Figure 3.1 shows the unit cell of the LAO structure, and it is a rhombohedral perovskite structure. The lattice constants are a=3.792Å[19], and the angle is 90.066°[20]. Below 544°C, LAO is rhombohedral with the point group $\bar{3}m$ and the space group $R\bar{3}c$. The rhombohedral primitive unit cell l a=b=g=60.113°[21].
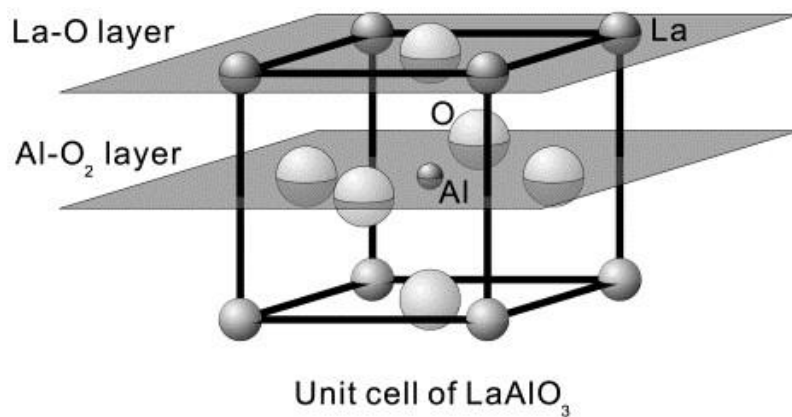
Figure. 3.1. The unit cell of LAO, image taken from [20]

The LAO structure exhibits a phase transition to rhombohedral perovskite structure at room temperature which transforms from the cubic structure at a critical temperature above T_c=544°C[21, 22]. Figure 3.2 illustrates the transition from rhombohedral to the cubic structure. When the LAO cools down, so-called twin domains are formed due to the phase transformation. The twin domains can be seen by the naked eye.
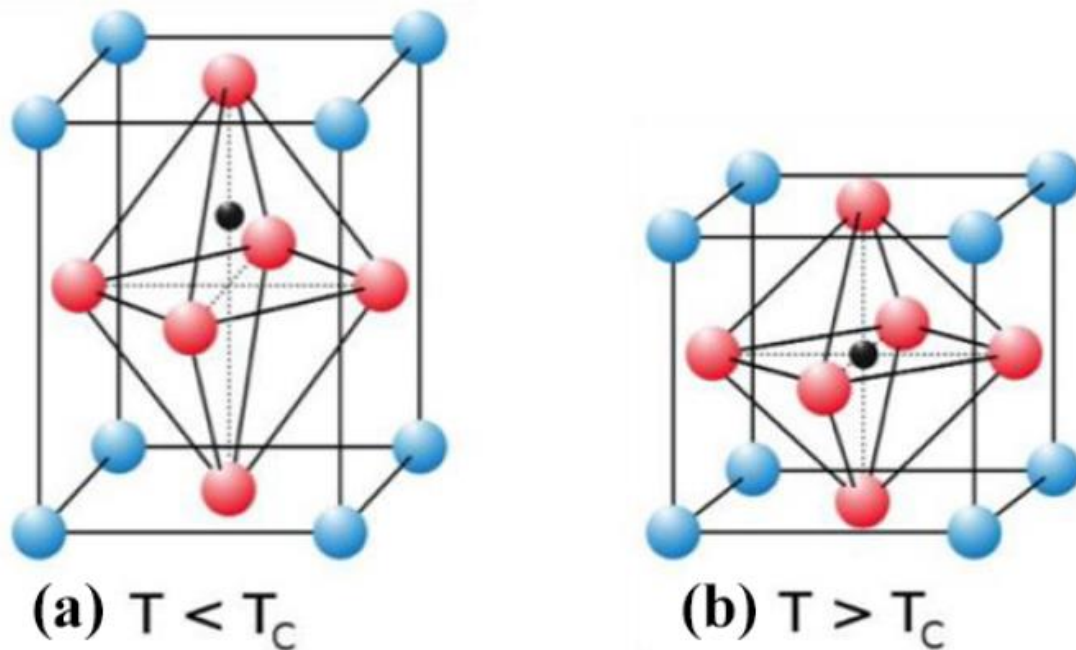
Figure 3.2. LAO structure transitions from the rhombohedral to cubic. Image is taken from[23] - (a) is the rhombohedra and (b) is cubic structure. The blue cation is La, the red cation is oxygen, and the black cation is Al.

Twin domain in LAO

It is reported that the oriented domain-wall between lamellar twins was perpendicular to the original cubic cell (100) and (110) directions. The transition temperature is around 530-550°C [24-26]. From higher to lower symmetry phase, the transition causes stress, which results in the formation of twin. The twin planes may show two regions with different reciprocal lattices, as in Figure 3.3. Basically, the twin domains have lamellar structure or tweed-like meeting in lines on the LAO surface.

Footprint domain in LAO

Twinning occurs when the LAO is cooled below T_c to room temperature. Afterward, cutting and polishing crystals near a rational crystallographic plane of the cubic – (001)cub. There are two reasons, the macroscopic plan will change from the true crystallographic plane: firstly, unavoidable misorientation of the cut, and secondly, twinning the corrugation of the true lattice planes (in Figure 3.3 (a)-(c)). Figure 3.3 illustrates the mechanism. The polished crystal is heated up over T_c, and then the twinning disappears again. However, due to polishing on diverse oriented domains, "negative traces" or "footprints" of preceding twin-domain patterns causes a surface relief. Heating mainly redistributes or relaxes the thermal strains or other defects. Thus, the twin domain might transpire in other positions and orientations when the crystal loses heat at room temperature. Therefore, the new topography of the surface will be an overlay of footprints of previous domains and actual twin domains.
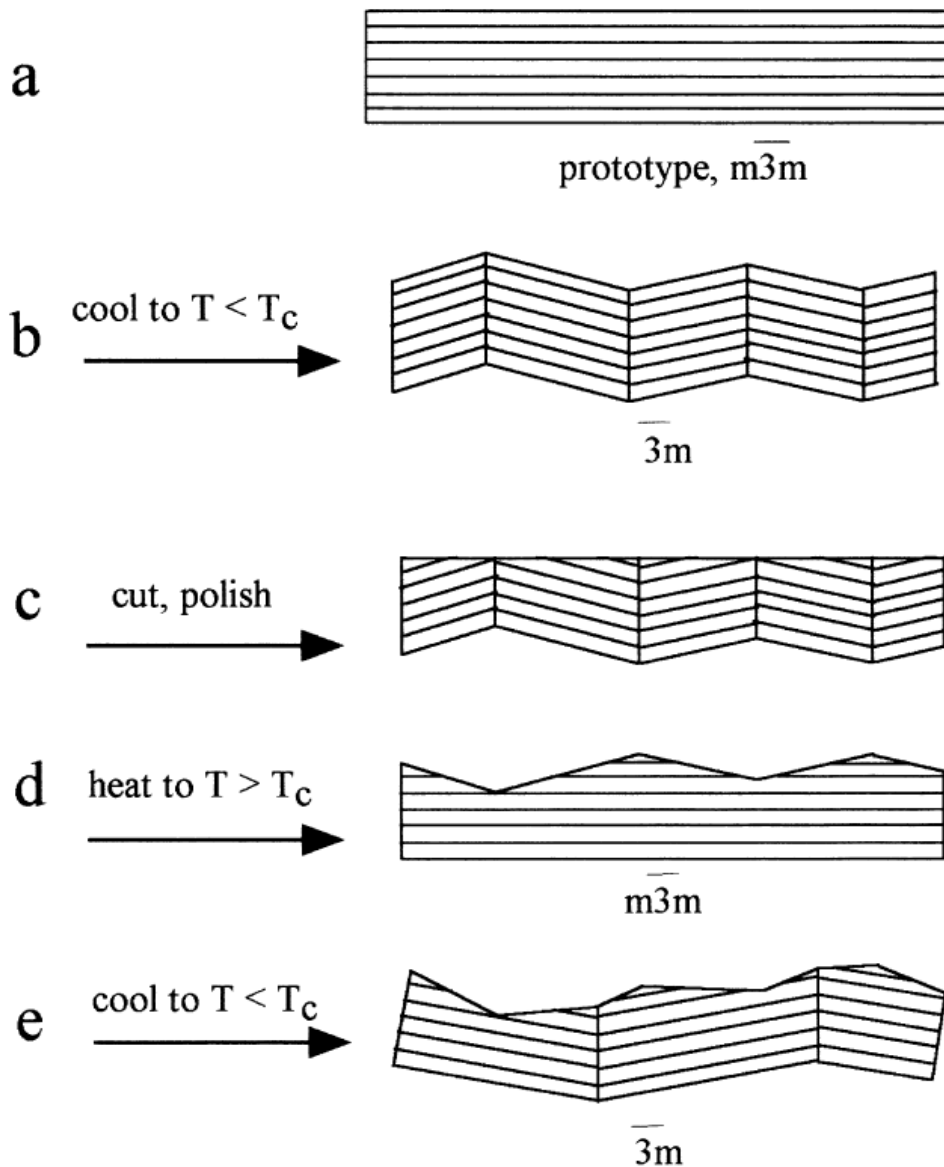
Figure 3.3. Schematic mechanism leading to the existence of surface kinks indicating vanished domain structure (domain footprint), image taken from [21]

3.1.2 Strontium titanate_SrTiO₃ (STO)

Strontium titanate ($SrTiO_3$, STO) is a cubic structure, and it is a perovskite, with lattice constant a=3.905Å.[27] As we can see from figure 3.4, the STO is stacked on two possible surface terminations alternately, namely strontium oxide (SrO) layers and titanium dioxide (TiO_2) layers. In the structure of STO, the SrO layer is bound with an ionic bonding in nature. Since the SrO layer has water-soluble features[28], we might think the layer can be removed chemically by deionized water (DI water). Thus the STO substrates can terminate TiO_2 layers by using DI water. It can be assumed that in the lattice constant, the surface lattice should match with anatase TiO_2. The TiO_2 can have rutile, anatase, and brookite structures. The anatase and rutile have tetragonal structures. The brookite has an orthorhombic structure. We found out that the lattice constants are pretty similar to the

13

lattice constants, both STO and anatase TiO_2. It can be available to fabricate thin films by deposition of one material onto the other[29]
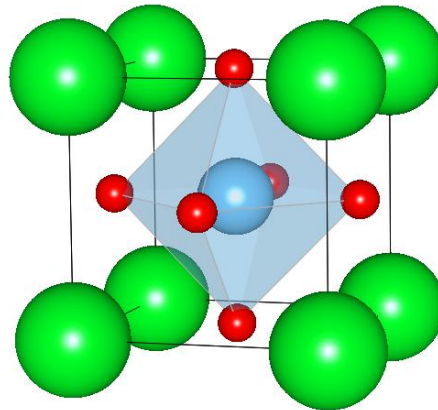

Figure 3.4. The structure of $SrTiO_3$, where the red ones are oxygen, the light blue one is titanium, and the green atoms are strontium.[27]

3.1.3 Sapphire

Sapphire can be used as a substrate; it has benefits, such as the same structure with GaN crystals, high-temperature stability, heat dissipation, and good chemical properties. Sapphire also enables larger wafers at a relatively low cost. At present, high-quality GaN crystals can be epitaxial on the sapphire wafer with the development of technology. The sapphire surface has become one of the ideal practical applications of the substrate[30, 31].

Sapphire has a hexagonal crystal structure, and the crystallographic structure of the plane is similar to each other. In addition, sapphire has a Mohs hardness of 9, and its melting point is exceedingly high at 2050°C, so it is suitable as a substrate for thin films that need to be deposited at high temperatures like GaN. Additionally, because it is not easily corroded by acid or alkali, it can withstand various wet etchings required for the LED manufacturing process and has the advantage of low price.[31, 32]

3.1.4 Silicon

Silicon wafer is the most common substrate in the semiconductor field. The most important reason for using a silicon substrate is that an excellent silicon oxide film (SiO_2) exists. When silicon is heated in an oxidizing gas, it is oxidized to become silicon oxide, an oxide film. This is a very stable insulator, which fortunately does not exist in other semiconductors. This silicon oxide film is a material that is used tremendously usefully in semiconductor devices and processes. Silicon is the second most abundant element on Earth after oxygen. Silicon oxide is the main component of all sand and rocks that can be easily found around us. Therefore, silicon can be made by reducing sand through an appropriate process. That is, the advantage of elemental semiconductors lies in their stability. Silicon has an excellent oxide film, is abundant on Earth, has strength as an elementary semiconductor, is easy to manufacture, and has excellent temperature characteristics.[33]

3.2 Films _ TiO₂

Titanium dioxide has a wide band gap[34], intensively researched during past years because it had possible applications such as biocompatibility, photovoltaics, batteries, and high photocatalytic properties for many decades. It has a vast number of valuable features and an extensive range of applications[19]. Titanium dioxide is called titania or titanium (IV) oxide, TiO_2, significantly beneficial due to its non-toxicity, low cost, abundance, stability and optical-electronic properties, and other benefits. [35]

Titanium dioxide can be classified into three different crystal polymorphs: anatase, rutile, and brookite by deposition method and nature pure or mixed phase. In the three polymorphs, the most stable phase is rutile[36] under ambient conditions. In nature, the rutile phase of TiO_2 is the thermodynamic equilibrium, but two other isomorphs, anatase and brookite, also exist naturally. Anatase and brookite can be formed at all temperatures; moreover, they will change rutile when they are heated[19]. The central studies of TiO_2 have been performed on the rutile phase. Crucially anatase appears to be the equilibrium phase for small particles. Thus, it is generally claimed that anatase is the active component in many titania-based heterogeneous catalysts and current solar cell applications based on nano-crystalline material. As such, there is a clear need to gain a better understanding of the anatase surface structure and the role of the TiO_2 growth conditions (e.g., substrate temperature, oxygen pressure during growth and annealing, etc.[19])

The space groups of anatase, rutile, and brookite TiO_2 are I41/amd, P42/mnm, and Pbca, respectively. [37] The crystal bulk structure of each phase is that anatase and rutile are tetragonal, and brookite is orthorhombic. Figure 3.1 illustrates the schematic unit cell of each structure. The lattice parameters of anatase, rutile, and brookite TiO_2 lattice parameters are summarized in Table 3.1.

Table 3.1 The lattice parameters for rutile, anatase, and brookite TiO_2 [37]

Species	a (Å)	b (Å)	c(Å)	$\alpha=b=\gamma$(°)
rutile	4.602	4.602	2.956	90
anatase	3.796	3.796	9.44	90
Brookite	9.166	5.436	5.135	90

The band gap energy of anatase, rutile, and brookite TiO_2 is 3.20~3.53 eV, 3.01~3.37 eV, and 3.13~3.56 eV,[22] respectively. It has been decided that in other forms like TiO_{2-x} as stated in the band gap, the origin of 'Ti 3d-gap states' in the band gap presents a correlation with oxygen vacancies and/or interstitial titanium in the host TiO_2.[38]
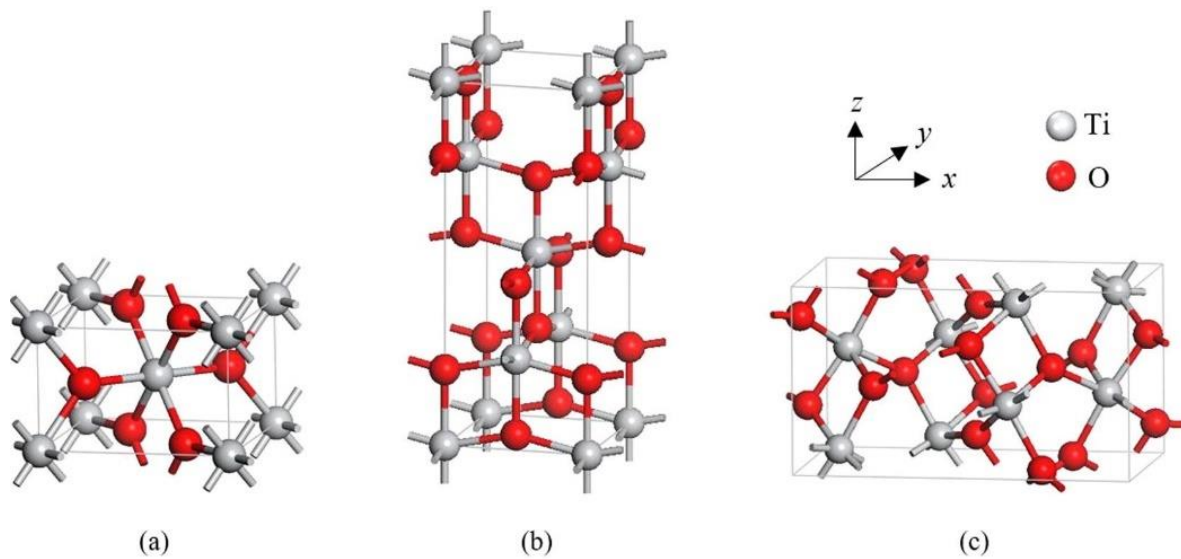
Fig.3.5. The primitive unit cell of (a) rutile, (b) anatase, and (c) brookite TiO_2.[39]

On the other hand, the morphology of the surface is an essential factor for the features of the TiO_2 thin films. For instance, surface nanostructures have been verified to be remarkable in achieving performance in many applications because of a vast surface area for effectively gathering electrons and/or photons. Therefore, creating fine quality pure phase anatase TiO2 thin films with editable surface morphologies is crucial to their applications[40].

3.3 TiO_2 on LAO

TiO_2 thin films can be created on diverse substrates, like oxide surfaces, such as MgO, $SrTiO_3$, and $LaAlO_3$. From all the substrates examined, $LaAlO_3$(LAO) has the best coherency thanks to its minor lattice mismatch with anatase TiO_2. In the bulk phase, anatase TiO_2 is a tetragonal structure at a = 0.3776 nm and c = 0.9486 nm, and this mismatch is only 0.4% growing epitaxially on the (0 0 1) surface of LAO. On the other hand, studies have mainly concentrated on the bulk structure of the anatase films. Moreover, it has also explored optimizing a parameter of growing conditions to procure fine surface properties of anatase TiO_2 (0 0 1), in other words, smooth terraces atomically with well-defined monoatomic step-structures[19].

4 Experiment detail

This chapter presents how to prepare the series of samples, and it will explain all of the tools for creating and characterizing samples. All the series are created by Ph.D. students Thomas Vågenes Brakstad and Marina Jorge. I got the samples from them and characterized them by 3D Optical Profiler and AFM to study the topography of the surface.

4.1   Fabrication samples

4.1.1 Substrate selection and preparation

For this project, we deposited TiO_2 films simultaneously on four different substrates (LAO, STO, Si, and sapphire). Seven different sets of films were made in total, but only a few of them were studied here. The deposition parameters were varied. Prior to deposition the LAO substrates were annealed at 1025°C for two hours; the STO substrates were baked at 950°C and leached in deionized water in an ultrasonic bath for 2 minutes; the whole process is done twice. However, sapphire and silicon substrates were not heated. In ultrasonication, it is used to wash acetone, followed by isopropanol, and deionized water for the substrates. After that, all the substrates were ready to be deposited in the PLD chamber; each substrate size is 10 x 10 mm^2.

4.1.2 PLD setup and deposition parameter

After cleaning and heating the substrates, TiO_2 films were deposited using PLD. A KrF excimer laser(Lambda Physics COMPex Pro, 248nm, 20ns) was used as a laser at 5 Hz to ablate a titanium oxide target (TiO_2 compressed ceramic powder). The target was pre-ablated with 1000 pulses before each deposition, and four different substrates were deposited on simultaneously.

In a vacuum chamber with a base pressure of 10^{-9}mbar, the films were deposited. Either only oxygen, a mix of oxygen and argon, or only argon, were back-filled in the chamber during the deposition. The pressure in the vacuum chamber varies from 10^{-6} to 10^{-2}mbar during deposition for the various films. Except for one film (B1), oxygen gas is supplied for all depositions. The deposition took place at $\sim$ 700°C; the substrates and target kept a distance of about 3.6cm.

Two PhD students (Marina and Thomas) characterized the samples using other techniques. The films were split into two different series, A and B, by laser energy density, i.e., laser fluence, and series A (A1 and A2) were created at a low fluence at 0.8J/cm^2. On the other hand, series B (B1 to B5) was fabricated at a higher fluence than series A at 2J/cm^2. They were kept at the same total pressure at $\sim$ 9 x 10^{-3} mbar; however, the background atmosphere was a various mix of argon and oxygen between 0% oxygen and 100% oxygen. The deposition parameters are listed in Table 1.

Table 4.1 Growth parameters for the TiO$_2$ films divided by fluence into series A and B. The background pressure was ~ 1×10^{-9} mbar for all depositions.

Sample label	O$_2$(sccm)	Ar(sccm)	P$_{dep}$(mbar)	Fluence(J/cm^2)
A1	1	0	4×10^{-6}	0.8
A2	50	0	2×10^{-2}	
B1	0	100		
B2	1	99		
B3	2	98	2×10^{-2}	2.0
B4	10	90		
B5	100	0		

Figure 4.1 shows the inside of the chamber during deposition and the substrate holder, that can take up to 5 substrates at once. For our films, the center place was not used.

Figure 4.1. The left picture is inside the PLD chamber during the plume deposition, substrate holder, and TiO2 target. The right image is the substrate holder, and it is four-hole for substrates.

4.2   Characterization

4.2.1 3D Optical Profiler setting used

3D Optical Profiler is used to measure the surface topography for large areas and determine film thicknesses using white light interferometry (WLI). Four different corners, such as left high and low, and right high and low, were measured on the TiO2 films on LAO. All the samples were measured using 2.5x magnification Michelson objective lens with 0.55x and 1x zoom lens. Figure 4.2 illustrates the Michelson lens. In addition, some specific areas of B1 and B5 on LAO sample were also measured under the same condition. Vertical Scanning Interferometry (VSI) mode was used for the processing method with 1x scan speed, back scan 20μm, total length 30μm, a threshold of 2%. The force intensity was 50%, and the

home scanner after measurement was based on 50% of pixels. The stitching function is also used to understand the entire image, and other measurement conditions were equal as above.

Figure 4.2. Michelson lens.

4.2.2 3D Optical Profiler image and data extraction

All those data could get using a program called 'Vision 64' by Bruker and analysis used by a program called Gwyddion. Gwyddion processed all the images and data taken from Vision 64. 3D Optical Profiler images proceeded four various functions by Gwyddion.

(function names in italic):

1. Flatten the raw image using the function of "*Level data by mean plane subtraction excluding mask region*."
2. The images "*Shifted the minimum data value to zero.*"
3. Decide the color of the surface using the "*Stretch color range to part of the data.*"

4.2.3 AFM setup and setting used

The name of AFM is AFM Dimension Icon supplied by Bruker, which was used in this project; the scanning mode is contact mode. After figuring out a large area using 3D Optical Profiler, I decided to zoom in on the same regions to see the topography or morphology more specifically using AFM, especially B1 and B5 on LAO samples; the specific locations are shown in Figure 4.3 in more detail. I took the images $2x2\mu m^2$, $10x10\mu m^2$, $20x20\mu m^2$, $40x40\mu m^2$, and $80x80\mu m^2$ to figure out how different the topography of the surface is by zooming in or out. Although some images had errors, I could distinguish the difference by the size or location of the image.
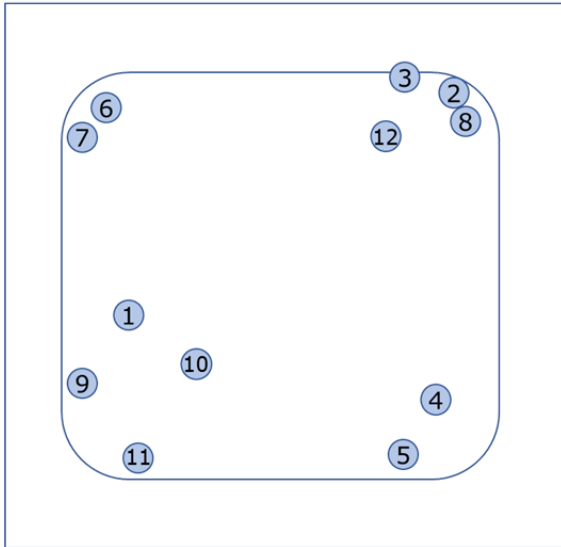
B1 on LAO   B5 on LAO
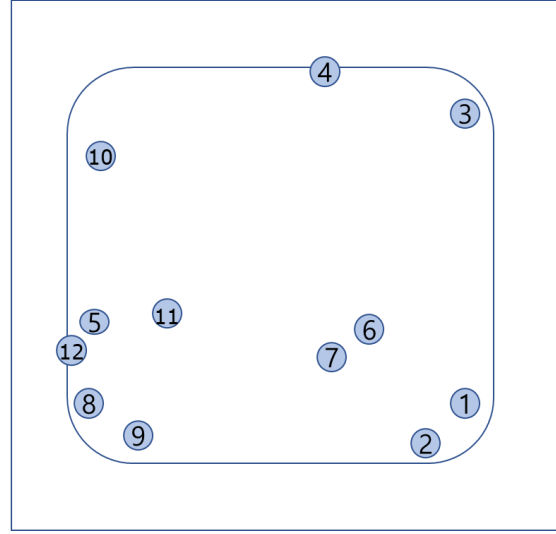
Figure 4.3. B1 and B5 films on LAO substrate where I measured the surface topography using AFM. The blue colored circles are the specific regions that were measured by AFM, in 12 different locations for each of them.

4.2.4 Image processing and data extraction

All the images and data of B1 and B5 TiO_2 films on LAO were taken using AFM, and the Gwyddion software was manipulated for image processing.

AFM images are also similar to 3D optical Profiler images analyzed using four fundamental functions in a sequence by Gwyddion. The first step in the image analysis is the background leveling/removal, and this consists of 5 steps (function names in italic):

1. The raw images were flattened using *"Level data by mean plane subtraction."*
2. The images were "*Aligned rows using the median methods.*"
3. Remove scars using the function "*Correct horizontal scars(strokes).*"
4. The images were "*Shifting minimum data made the value to zero.*"
5. Decide the color of the surface using the "*Stretch color range the part of the data.*"

I decided the color range of the AFM images was 2x2μm² and10x10μm² which covers 0-10nm, and for 20x20μm², 40x40μm², and 80x80μm², which covers 0-30nm in broad outline. If the 20x20 μm² image were too dark, I would change the color range to 0-10nm.

4.2.5 Meaning of RMS roughness(R_q) and average roughness(R_a)

The RMS(Root Mean Square) roughness means "The average of the measured height deviations taken within the evaluation length and measured from the mean line." The formula is

$$R_q = \sqrt{\frac{1}{N}\Sigma_{j=1}^{N} r_j^2} \ [41].$$

The RMS roughness means that it measures height peaks and valleys, and each of them is calculated as a square. Then, those numbers have calculated the average, finally find

the square root of the number. Thus, the RMS roughness is affected more a prominent peaks the microscopic surface texture, and thins means the R_q is larger than the R_a value.[42]

On the other hand, the average roughness means "Arithmetical mean deviation. The average deviation of all points roughness profile from a mean line over the evaluation length". The formula is

$$R_a = \frac{1}{N}\Sigma_{j-1}^{N}|r_j|.[41]$$

The R_a is calculated as the entire measured length or area, so it is smaller than R_q. Figure 4.4 shows different surfaces, yet all the R_a value is the same. Therefore also the rms. Roughness can be useful to calculate.
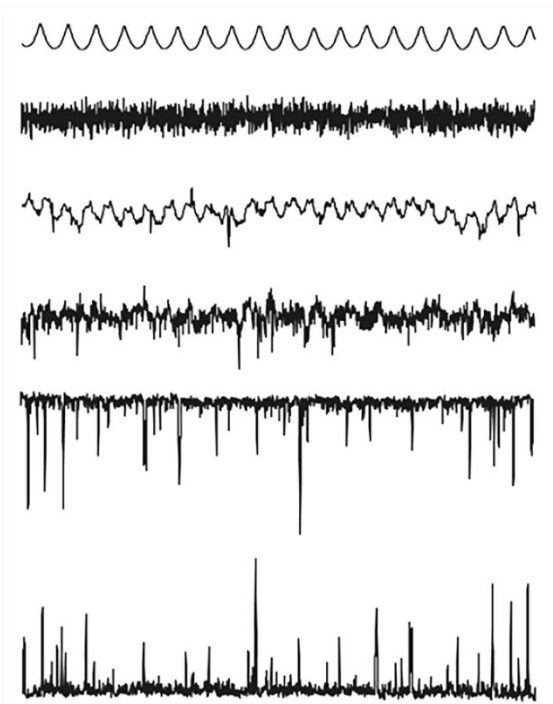
Figure 4.4. Even though the six surfaces seem all different, the Ra is all identical. Image is taken from[43].

Therefore, the R_a cannot care about some critical aspects of the surface, though R_a measures the absolute deviations from the average height.

4.3   Previous results of the samples

In this section, I will introduce the previous work.[1]

The previous master student measured the LAO substrates after annealing at 1025°C; Figure 4.5 is the 3D Optical Profiler images for two substrates.   The substrate seems disorderly, yet we can find some twins and flat areas. It is not precisely similar after deposition; however, we could compare the before and after deposition. I measured all the samples after deposition; and this might be useful for comparison.
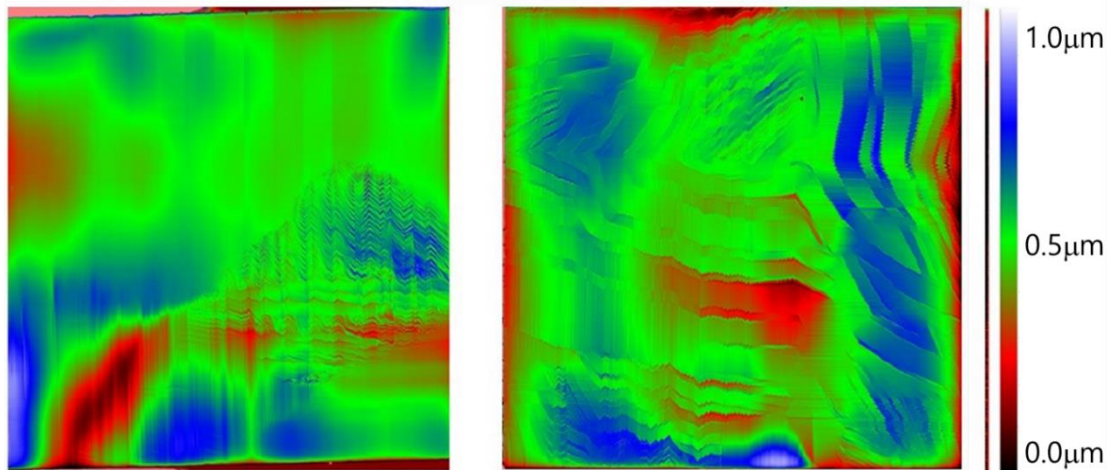
Figure 4.5. 3D Optical Profiler images of LAO substrates surface after annealing. It is taken from previous work.[1]

Also, Figure 4.6 is also the LAO substrates without any film on them, but they are the AFM images. We see narrow terraces that are rather flat, except that some have islands on the step edges. I will present my results from the AFM images of the films on LAO in the next chapter, and they are a pretty different topography than the flat steps seen on the bare LAO substrates.
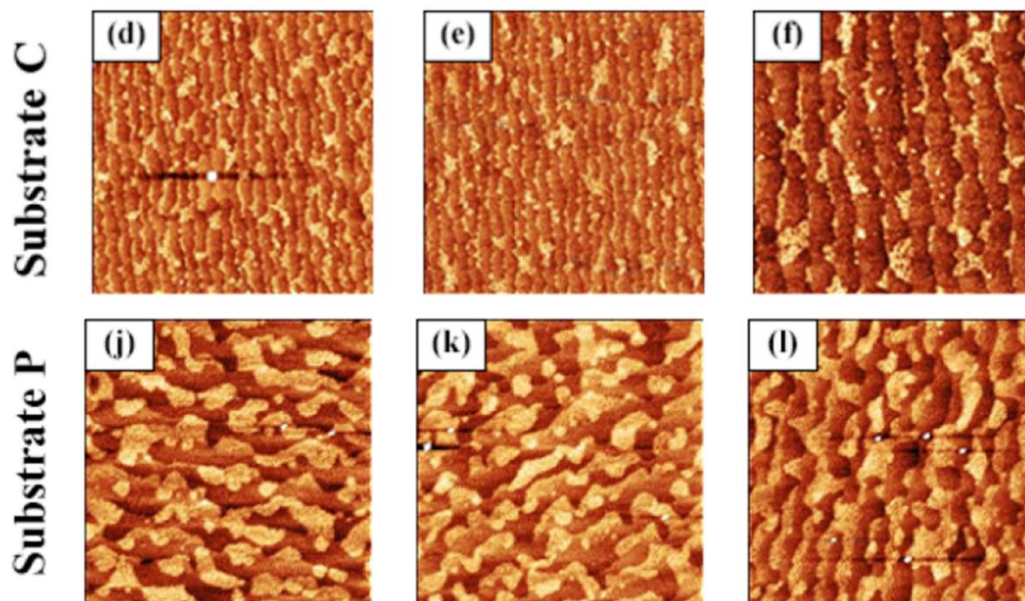
Figure 4.6. After annealing the LAO substrate of the AFM images.

4.4 Films deposition

As mentioned above, I got samples from Ph.D. students of Marina Jorge and Thomas Vågenes Brakstad. Figure 4.7 shows photography images of all the series of films on the four different substrates.

Figure 4.7 illustrates all the samples, and from the left high corner series are substrates on LAO, STO, Si, and Sapphire(clockwise). Unfortunately, B4 of LAO was broken, A1 of STO and Si were missed.
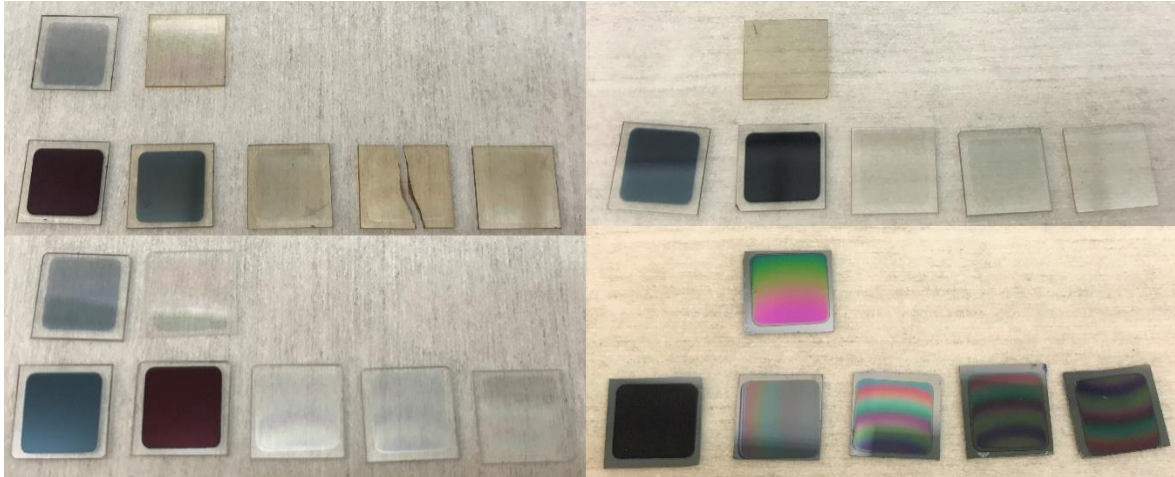
Figure. 4.7. After deposition of film samples; upper left panel shows seven films on LAO, upper right on STO, lower left on sapphire and lower right on Si. The first row is A1, and A2 last low is B1 to B5, in each panel.

5 Results and discussion

In this chapter, I will present and discuss the results of the experiment. First, I will describe the overview image of the larger size, which is the image of the 3D Optical Profiler from the beginning. After that, I will show an in-depth detail with the image of the AFM. Finally, from the AFM images, I will demonstrate the roughness and volume of hillocks.

Overview chapter 5

- Overview image of all the series on all the substrates by 3D Optical Profiler
- Four corner images of all the series on all the substrates by 3D Optical Profiler
- A1, B1, and B5 on LAO overview and four corner images by 3D Optical Profiler
- B1 and B5 on LAO AFM and 3D Optical Profiler images - results and discussion
- Measurement of roughness by AFM on B1 and B5 on LAO

5.1 3D Optical Profiler images

This section will describe the larger size of the images measured by the 3D Optical Profiler. One of the advantages of the 3D Optical Profiler is that it can rapidly scan both complete and specific areas. All the films scanned full images using stitching function image tool, and four corners left high and low, right high and low, and some particular areas were also scanned.

5.1.1 Overview of all films on all substrates

In this part, We will see an overview of all the series on all substrates. I have divided them into the A and B series.

Results

Although the stitching images have some stitching lines, they could be discovered in the entire area and can be compared to each substrate or each series. Figure 5.1 illustrates full stitching images for A series on all substrates; the size of the films is approximately 8.5mm x 8.0 mm; this is similar to all of the samples (or 8.0mm x 8.5mm in the opposite direction) because of the sample holder size (The figure on the right in Figure 4.1). The substrate size is 10.0mmx 10.0mm. As we can see, LAO samples have twins, and the surface is not uniform; meanwhile, other surfaces of substrate samples are pretty flat. Regrettably, A1 on STO and silicon were missing. The substrate and the film are a bit tough to distinguish in series A on LAO.
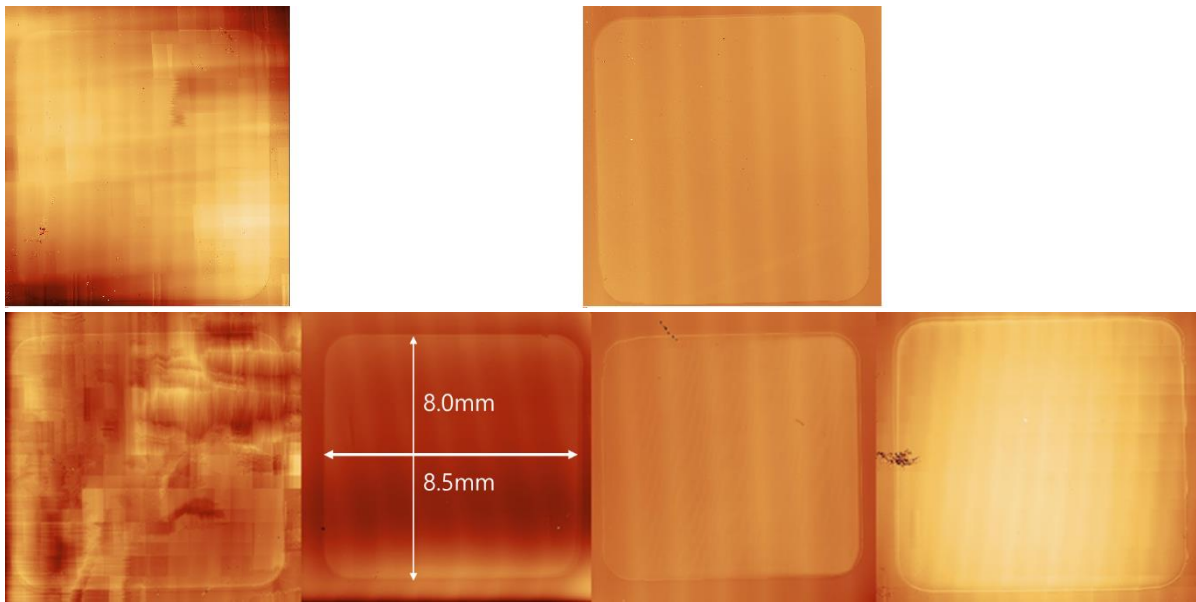
Figure.5.1. Overview images are based on the stitching of 3D Optical Profiler images of A1 (upper row) and A2 (lower row) on LAO, STO, sapphire, and silicon substrates - left to right. The color scale covers 0-3 μm. The films can be seen as squares with round corners. The image area varies from image to image, but the film is approximately 8.5mm x 8.0mm, as indicated for the A2 film on STO.

On the other hand, the B-series are more easily identified films and substrates in contrast to the A-series. Figure 5.2 describes the overview image of the B-series; unfortunately, the B4 film on LAO is broken, so I could not image the damaged region. From the images, we can see the estimated topography, such as twin or flat, despite how huge the size of the image is. Like the A-series, the B series on LAO topography has twin, flat, and a mixture of two, but other series look flat similar to A series.

Discussion

We knew the thickness of the A series is thinner than the B series from the previous work.[44]. For the LAO series, A1 and A2 are a bit challenging to distinguish the difference between substrate and film because LAO substrate is not very flat. On the other hand, as we can see, others can easily differentiate substrates and films or morphology features. Some series show some repeat patterns, for instance, stitching lines, or dark and bright films. I think this is due to massive size of the images. If I were to zoom in on them in this report, the pattern might not be displayed. However, for the silicon series, there are repeat depths; this is because of the errors in measurement (except B3). In the case of the substrate, LAO can exhibit significant twins, and other films look flat. All series can distinguish the difference between films and some scratches and contamination can be seen due to handling or other reasons. Since there are various morphology and topography, scratches, and measurement errors, I decided to zoom in on four corners of the surface and some specific areas.

26
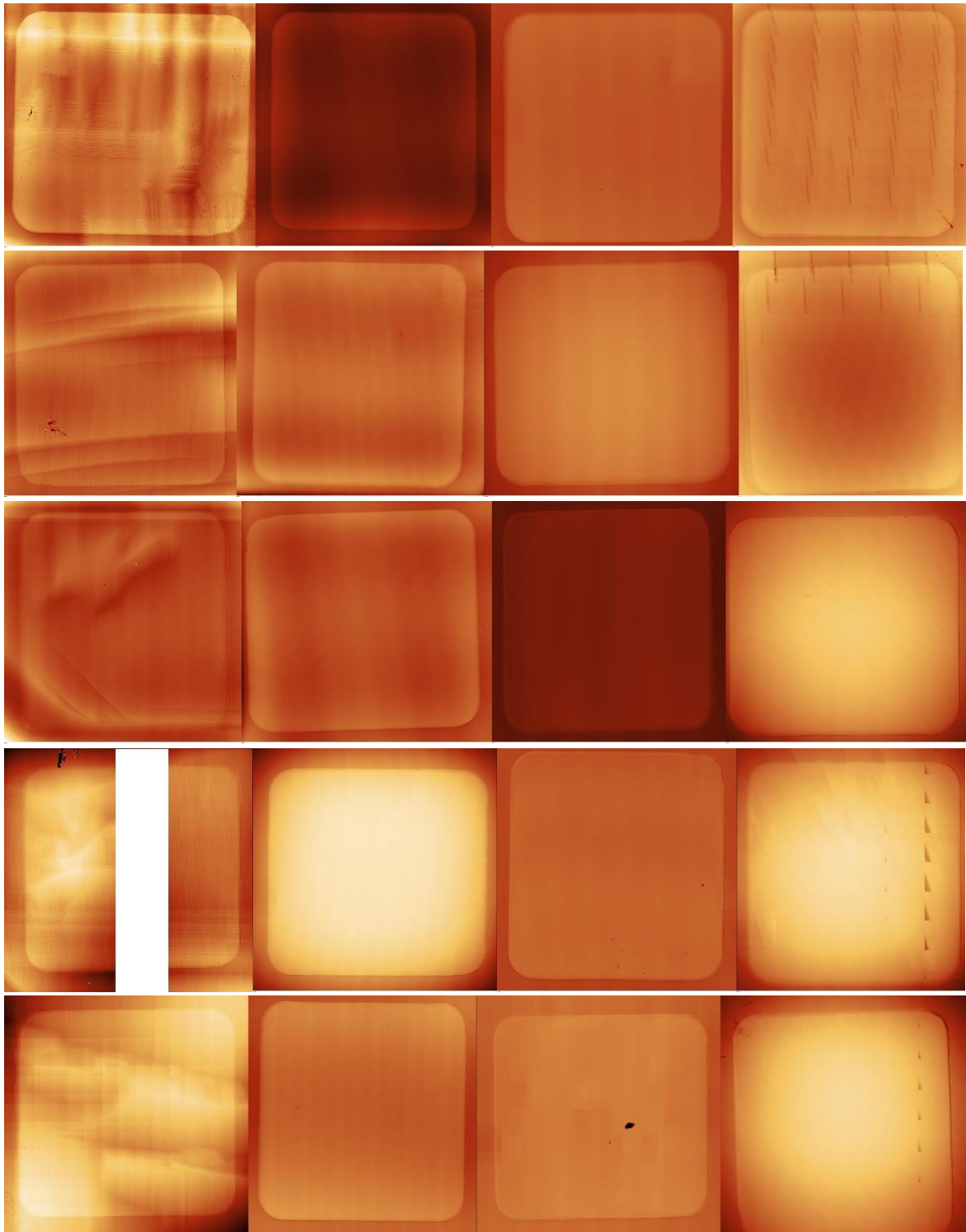
Figure 5.2. The overview image of the B series, from B1 to B5 (up to down) on LAO, STO, sapphire, and silicon substrates left to right, respectively. The color scale covers 0-7 μm for the B series' films. The films can be seen as squares with round corners. The image area varies from image to image, but the film is approximately 8.5mm x 8.0mm, as indicated in the A2 film on STO (Figure 5.1). B4 on LAO is broken, so the broken part was removed. The films on silicon have unexpected patterns (except B3); those are errors.

5.1.2 Zoomed in images of the corners of all films on all substrates

Results

I decided to measure four corners of the films in all the series to see more details, omitting the use of the stitching function. To compare the A series and the B series, I chose A2 (because the A2 series has all the substrate samples) and B1 and B5. B1 and B5 films have identical deposition parameters except for the oxygen and argon ratio.

Figure 5.3 to Figure 5.6 illustrate the four corners of the A2, B1, and B5 series on each substrate. As you can see, it is much more detailed than full stitching images, as the LAO substrates can figure out twins, and all substrates also have discerned contaminations and scratches. The unique thing is that all the regions near the edge of the films seem thicker than other areas of film. All A2 series seem thinner than B1 and B5.

B5 on LAO has a pretty constant vertical twin, except the left low corner, which is similar to B1. Although the B1 has haphazard twins, the left low corner looks pretty flat. On the other hand, A2 on LAO has twins on all four corners randomly.

Silicon series have more scratches or contaminations than other films, and it is shown more specifically in B5. Meanwhile, B5 on silicon on the right low corner has a small square thinner than other regions since it is taken for measuring the X-ray Photoelectron Spectroscopy (XPS). Other films were measured before using the 3D Optical Profiler, but only B5 was taken at a later time.

Discussion

A2 series cover 0-1 µm, and B1 and B5 series cover 0-2 µm, and the A series color gap is more extensive than B series, so I could understand that A series is thinner than B series. The thickness of the sample is cross-checked with the previous work.[44]

Also, near the edge of the films, the area seems thicker than other regions or they are layered on the edges. It has been deduced that the substrate could move or wiggle in the substrate holder during the deposition. In addition, I believe that the edge effect and shadow effect might be affecting the substrates.

Meanwhile, in the B5 on silicon on the right high corner, the edge seems even more thinner than the substrate. However, while measuring with the 3D Optical Profiler, the stage or sample might have been tilted. Thus, the border looks deeper than the substrates, so it would not have depth if measured again.

On the other hand, there are six and four somewhat-vertical lines in A2 on LAO left low corner and right low corner, respectively. Those lines are the errors during the measurement.
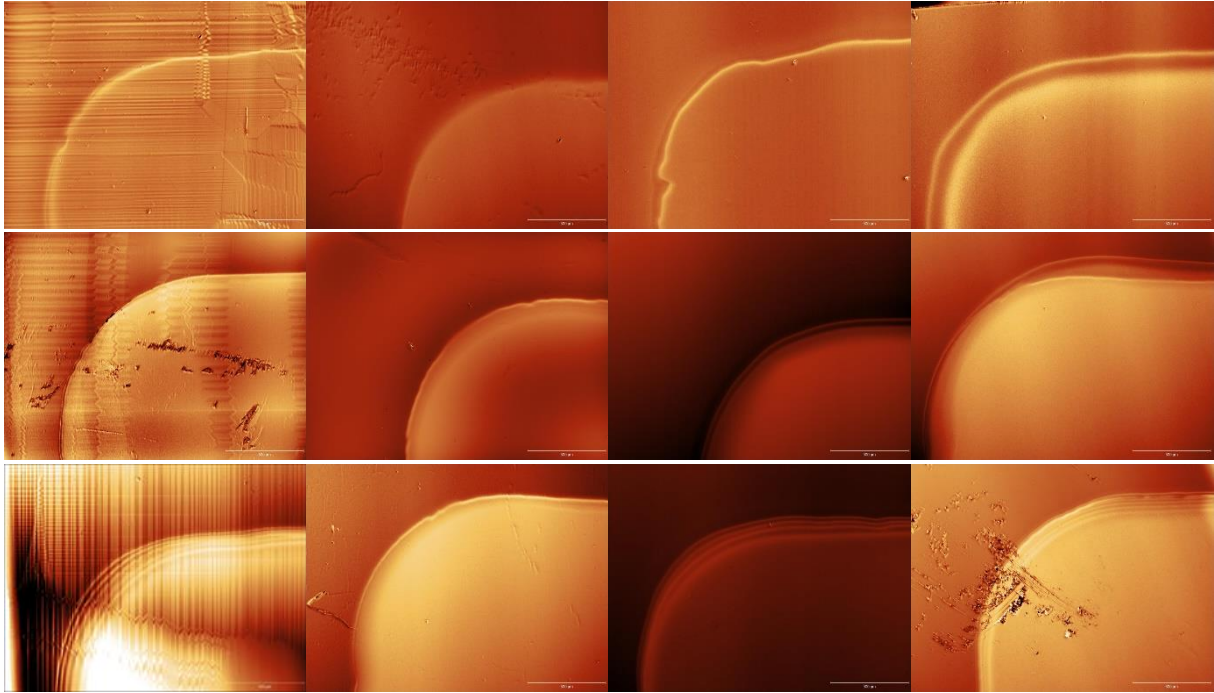
Figure.5.3. (1.5 mm x 1.9 mm) 3D optical profiler images of the left high corners of the series for all substrates A2, B1, and B5. (LAO, STO, sapphire, and silicon substrate from left to right). The color scale covers 0-1μm for the A2, and 0-2μm for the B1and B5, respectively.
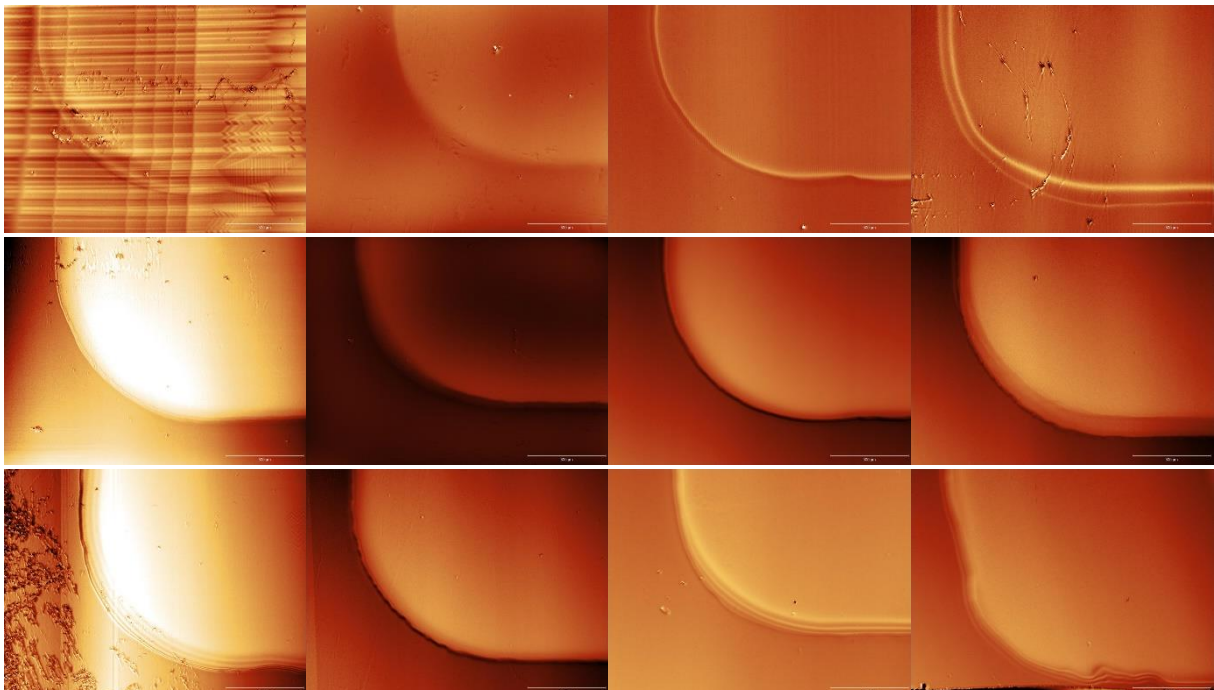
Figure.5.4. (1.4 mm x 1.9 mm) 3D optical profiler images of the left low corners images of all substrates A2, B1, and B5. (LAO, STO, sapphire, and silicon substrate from left to right).
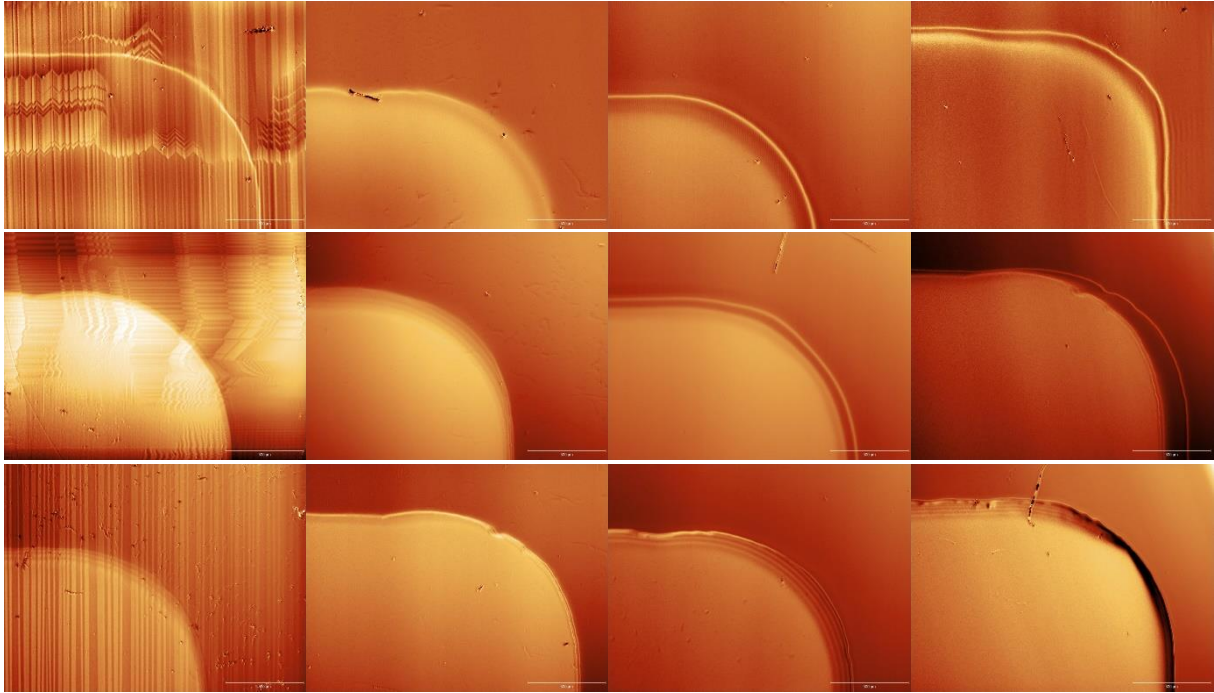
Figure.5.5. (1.4 mm x 1.9 mm) 3D optical profiler images of the right high corner images of all substrates A2, B1, and B5. (LAO, STO, sapphire, and silicon substrate from left to right).
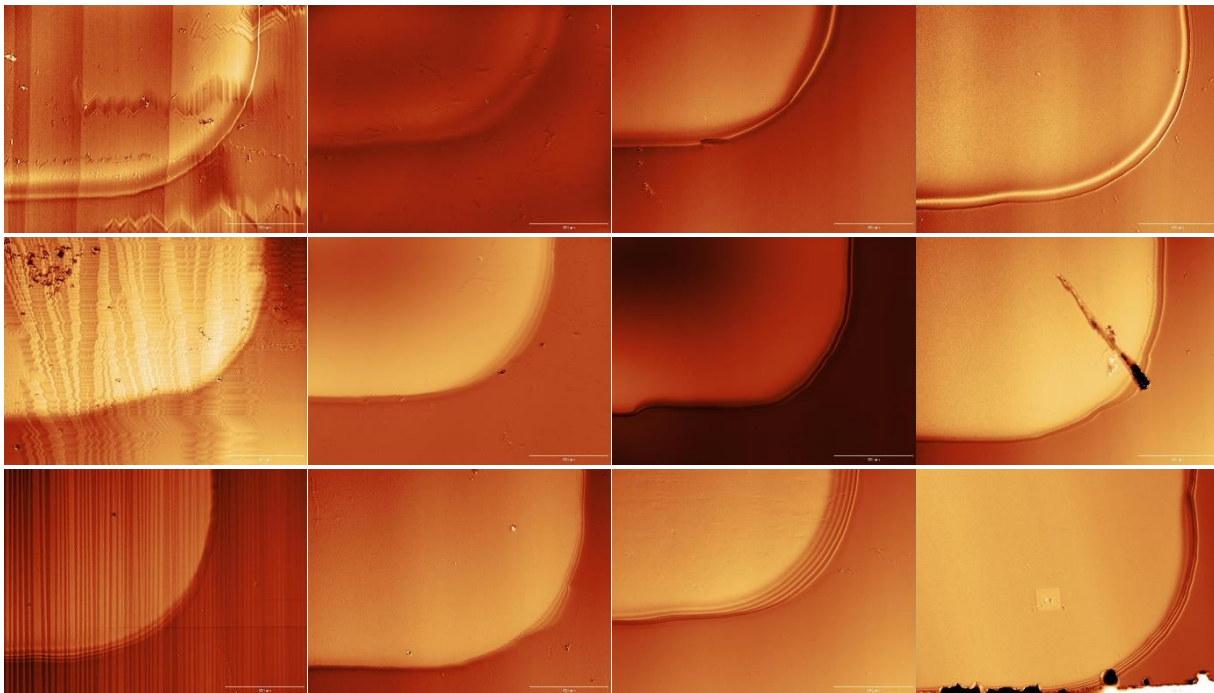
Figure.5.6. (1.4 mm x 1.9 mm) 3D optical profiler images of the right low corner images of all substrates A2, B1, and B5. (LAO, STO, sapphire, and silicon substrate from left to right).

Figure 5.7 is the image of previous work[1] A2 on LAO. The left high corner of image (a) looks to be the same as mine and the right low corner of image (b) looks to be the same as mine.
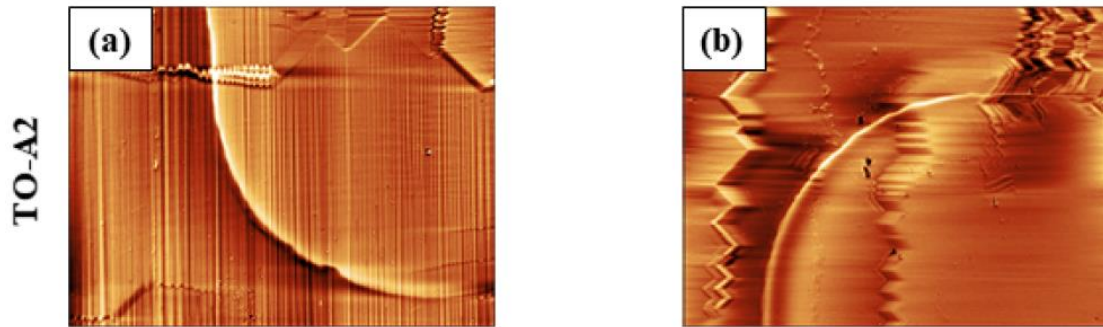
Figure 5.7. Previous results for A2 on the LAO[1]

5.1.3 3D optical profiler images of A2, B1, and B5 on the LAO

Since the LAO series have a lot of variation in the topography, I decided to compare the A2, B1, and B5 on the LAO series as complete and four corners.

Results

Figure 5.8 is an overview image of the A2, B1, and B5 on the LAO, using a "normal" color scale and a "repeated black and white" color scale to highlight the variation in topography.

For the A2, the topography is exceedingly random, such as vertical, horizontal, and mixed twin, and flat regions. The size of the twin is also diverse. It is a bit tough to discriminate A2 from substrate and film.

On the other hand, we can distinguish B1and B5 more accurately than A2 between films and substrates. B1 also has random patterns. It looks like a hill on the upper side of the sample, and the left low corner looks flat. Compared to A2, it has fewer twins. The sample of B5 has the most regular vertical twins, except the left low corner. Overall, there are two diagonals: the hills or the valleys.

Figure 5.9 shows only four corners of the samples, so the image is more specific and detailed without stitching lines. A2 on LAO has twins very randomly, and B1 and B5 left low corner has flat regions. B1 film also has a random shape of twins; however, the B5 film has pretty uniform twins – vertical lines. The twins of A2 are the most varying among them. The red arrows indicate flat areas, the white arrows point to the damage caused by the polishing when the substrate was prepared by the manufacturer, the green arrows indicate the twin footprints (I will explain more in detail in the discussion section), and the black arrows show twin regions.
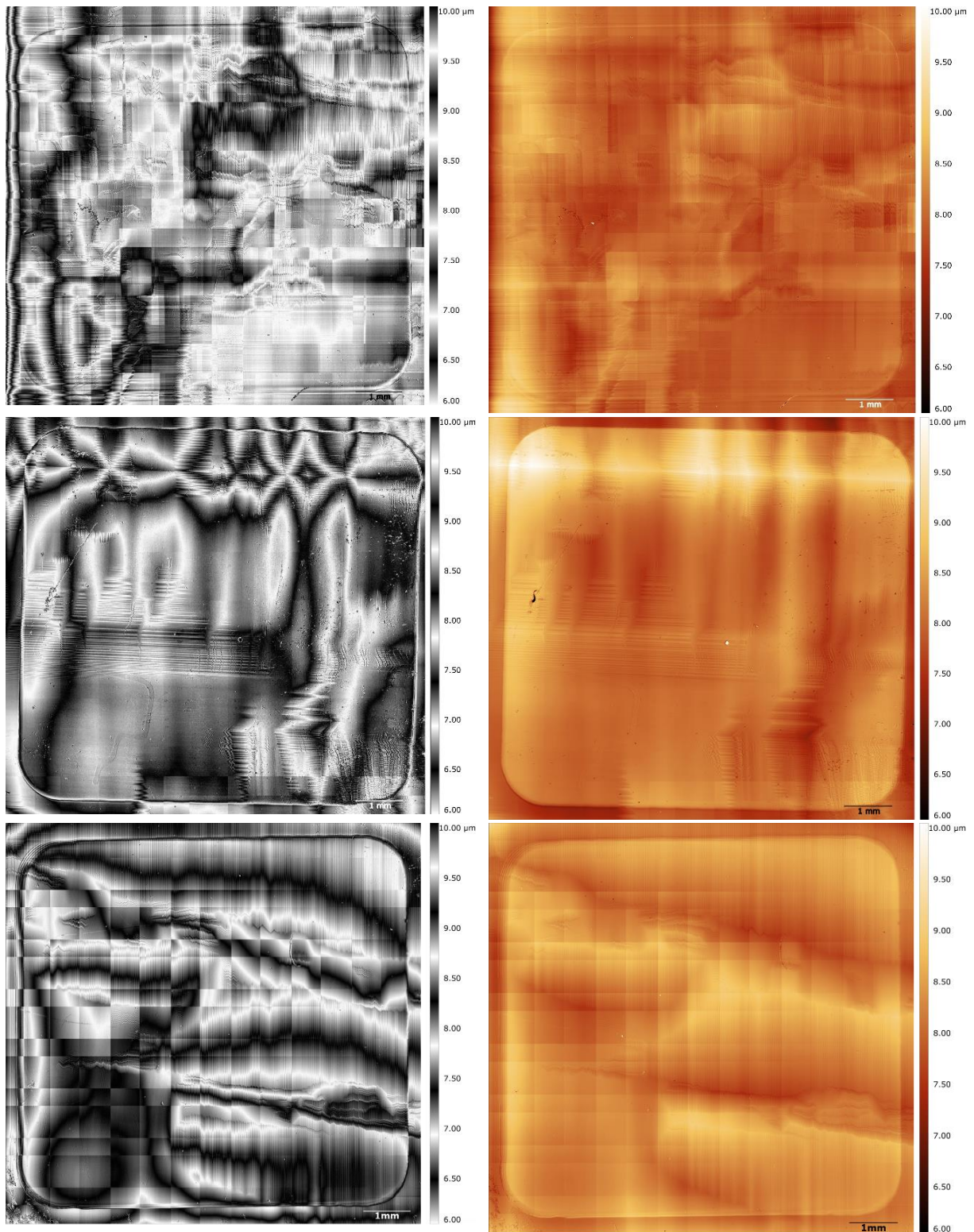
Figure 5.8. 3D optical profiler overview images of the A2, B1, and B5 on LAO, using two different color scales, showing the whole 10 mm x 10 mm substrates with the films. We can see twin, flat, scratch, unique pattern (looks like a snake) regions, and stitching lines that are thin horizontal and vertical lines that are artifacts due to the imaging processing
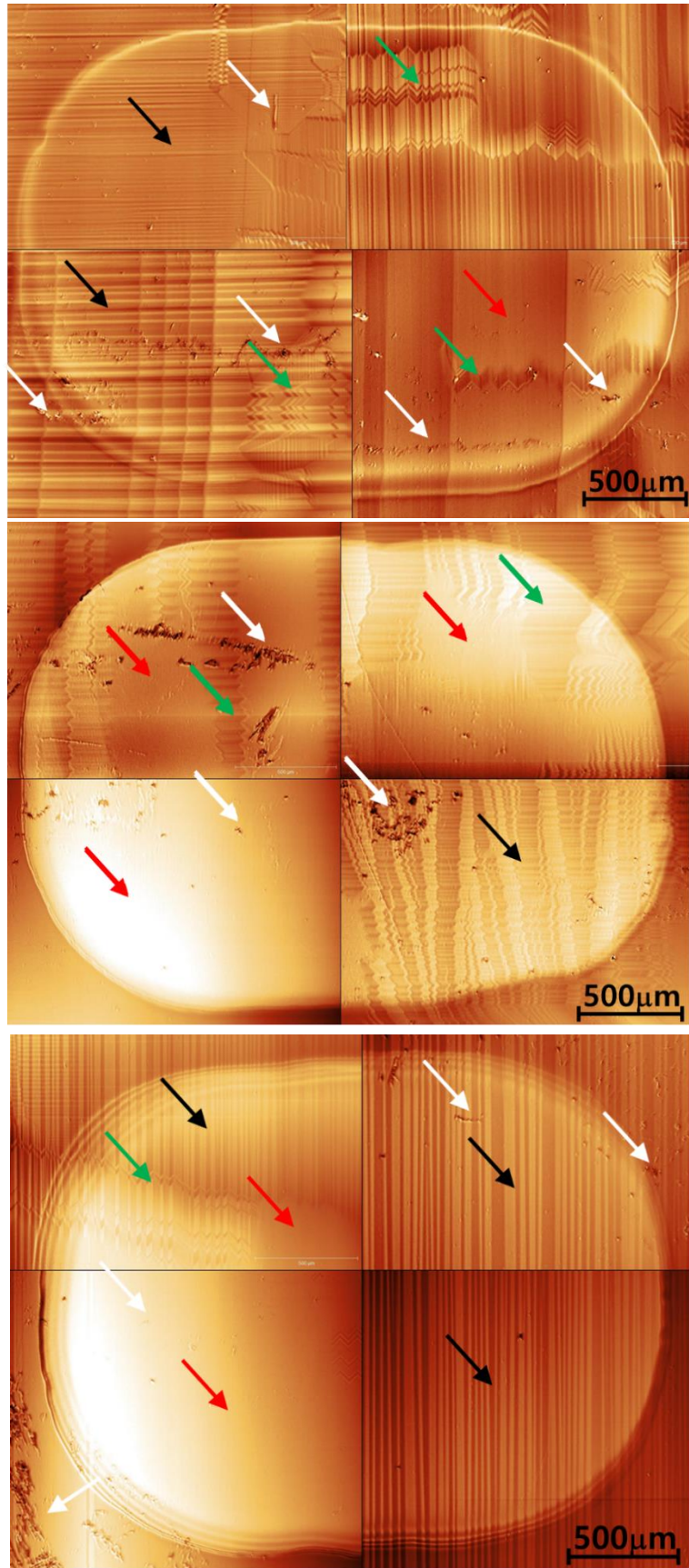
Figure 5.9. (1.4 mm x 1.9 mm) 3D optical profiler images of the A2, B1, and B5 on LAO, on the four corners. The red arrows indicate flat areas, the black twinned areas, and the green mixed areas.

Discussion

The substrate on the left edge of A2 is very dark; I believe it might not have been stable on the sample stage during the measurement. Thus, it seems very thin.

B1 on the left low side has contaminations that look like a snake, and I think it was contaminated before deposition.

According to Figure 5.9, there are four vertical lines in A2 at the right low corner, and this is due to measurement errors. They are not twin areas; likewise, the five lines on the left low corner are the result of errors in the measurement. The edge of B5 seems to have several layers, and I believe that the substrates were moved in the substrate holder. Because the substrate was not mounted firmly enough, it moved during the deposition due to it being lighter or smaller than the substrate holder.

To see how different the twin area and flat area are for the case of the LAO series, we measured the B1 and B5 on the corners and some other specific regions. They are all equal deposition parameters except the background gases of argon and oxygen ratio; the background gas of the B1 is 100% argon, and for the B5 is 100% oxygen. The following section will present AFM images with 3D Optical Profiler images.

As a received substrate LAO (commercially) is illustrated in Figure 5.10 a), the LAO substrates were annealed over T_c and cooled down to room temperature, and it was polished.

Before deposition, we prepared the substrates, baked them to 1025°C (over T_c), and cooled them down again. During this process, the substrates gained another twin. Bueble [21] called it 'footprints' or 'negative traces', which is described in Figure 5.10 b). We are able to find both the original twin (footprints from it) and the new twins. In Figure 5.9 the footprint is found in A2 left high and right low corners, B1 left and right high corners, and B5 left high corner. When they are heated again, the origin twin domain gets bigger, so we could compare Figure 5.10 a) and Figure 5.10 b). Since repeat heating makes the twin domain larger, the origin twin areas might look like flat regions[21].

a)

b)
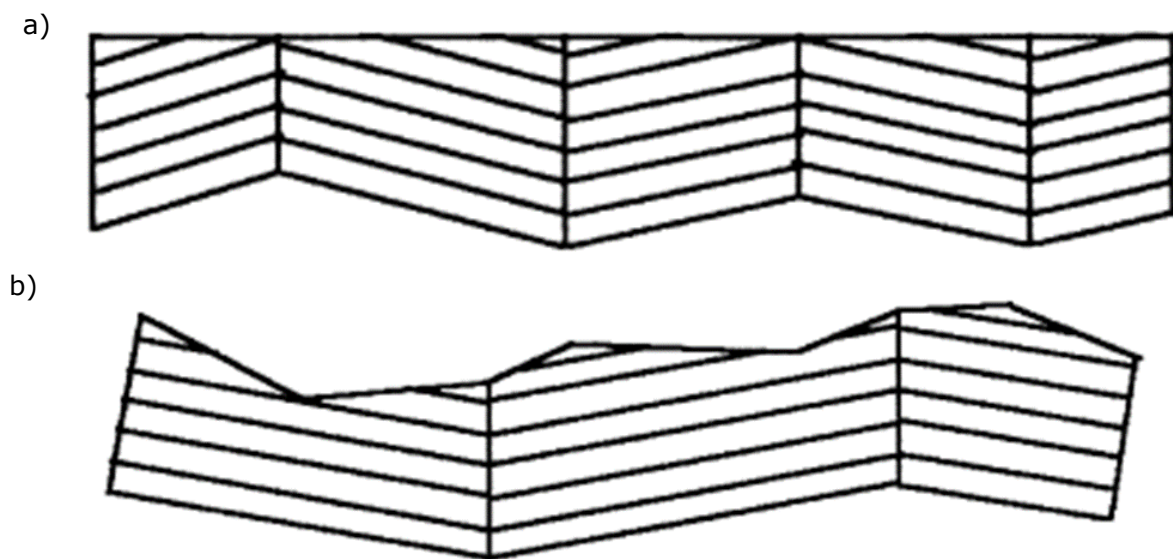
Figure 5.10. a) is as a received substrate surface, b) again annealing and cooling down the substrates, prior to deposition.

When the substrates were ready for deposition, Figure 5.10 b) entered the chamber to deposit TiO_2 using PLD. Then the substrates are heated to 750C (i.e., above Tc) and then the substrate and film lose down to room temperature again, and we end up with something like in Figure 5.11, where the film thickness is not to scale. Here the arrows illustrate the twinned, flat and mixed regions we saw in Fig. 5.9.

Since the film is thin – A series is 100-300 nm, B series is 650-750nm, we could see the topography of substrates in/through the films. During the deposition, not only the LAO but also STO, sapphire, and silicon were also deposited simultaneously. As we saw from the above figures, the other series on other substrates are flat. Thus, I believe the topography of the films is affected by the substrate topography.
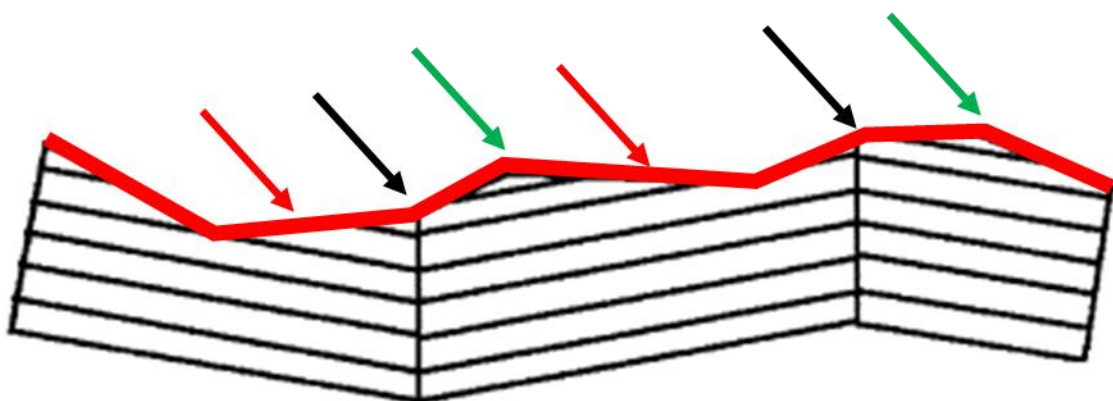
Figure 5.11. Schematic drawing of the TiO_2 film deposited on the LAO and cooled down to room temperature again. The thin red line is the TiO_2 film. The red arrow indicates the flat region, the black arrow manifests the twin area, and the green arrow point to the footprint of a previous twin.

5.2 AFM characterization

This chapter will be divided into two parts for AFM images combined with 3D Optical Profiler images of B1 and B5 on LAO, and roughness obtained from AFM images for B1 and B5 on LAO. We decided to study these two because they had a similar thickness, and almost identical deposition parameters except for the background gas during deposition: B1 had no oxygen, but only argon, while B5 had only oxygen, to the same background pressure as for B1. We can then try to make conclusions on what makes the topography of the TiO2 films vary; the film deposition parameters or the topography of the LAO surface, or both.

5.2.1 AFM images and 3D profiler images from the exact location of the film/sample

This section will explain how I linked the images obtained using the 3D Optical Profiler with the AFM images, to be able to couple the macroscopic properties (twinned, flat or mixed) with the nanoscopic ones (roughness, surface features and terraces on the nm scale).

Firstly, I will explain where and why I measured some specific areas using AFM.

Figure 5.12 shows the 12 different locations where I measured on films, approximately. Even though it seems like the locations are randomly chosen, they were chosen based on being twin, flat, and mixed areas as observed from the 3D profiler images.

B1 on LAO
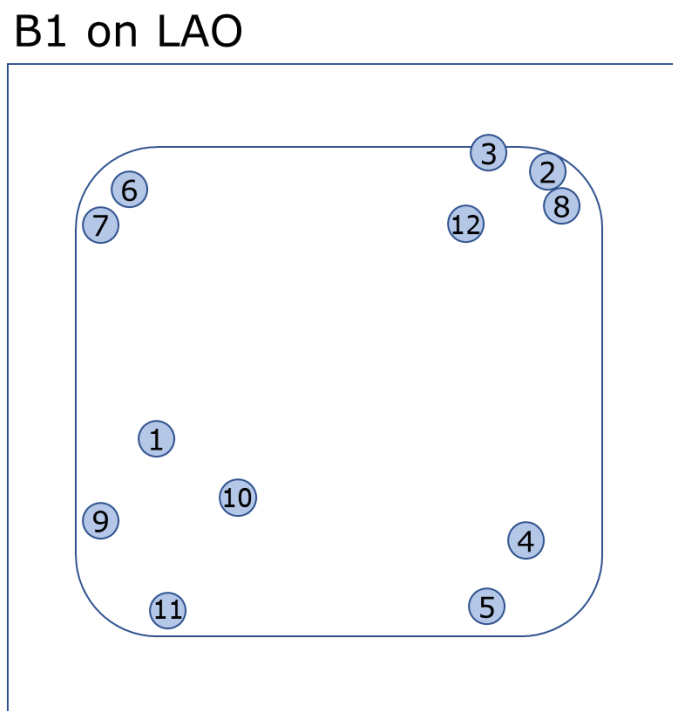
Figure 5.12. Schematic drawing showing the 12 locations (approximately) on the B1 film on LAO substrate where I measured surface topography using AFM. The blue colored circles are the locations. For B1, 1-4 are twins, 5-8 are mixed, and 9-12 are flat areas.

Figure 5.13 illustrates how I figured out the area using the AFM microscope and linked the 3D optical profile image. First, when I decided to measure a specific location), I used the AFM optical microscope to picture the area, see Figure 5.13 a). This picture has a built-in

red crosshair, and this image was then made partly transparent and overlaid on the 3D Optical Profiler image as shown in Figure 5.13 b), so that the features in the two images overlapped completely. The red crosshair was then transferred to the 3D profiler image at the exact same point, by simply drawing a new crosshair on top of the one from the AFM picture, and then the AFM picture was deleted. see Figure 5.13 c). Next an 80x80 μm^2 AFM image (maximum scan size) taken in the chosen location was measured and compared to the features in the 3D optical profiler image. We can clearly see that the area images in the 80x80 μm^2 AFM image, matches nicely with the zoomed in image from the region indicated by the cross-hair, in Figure 5.13 d).
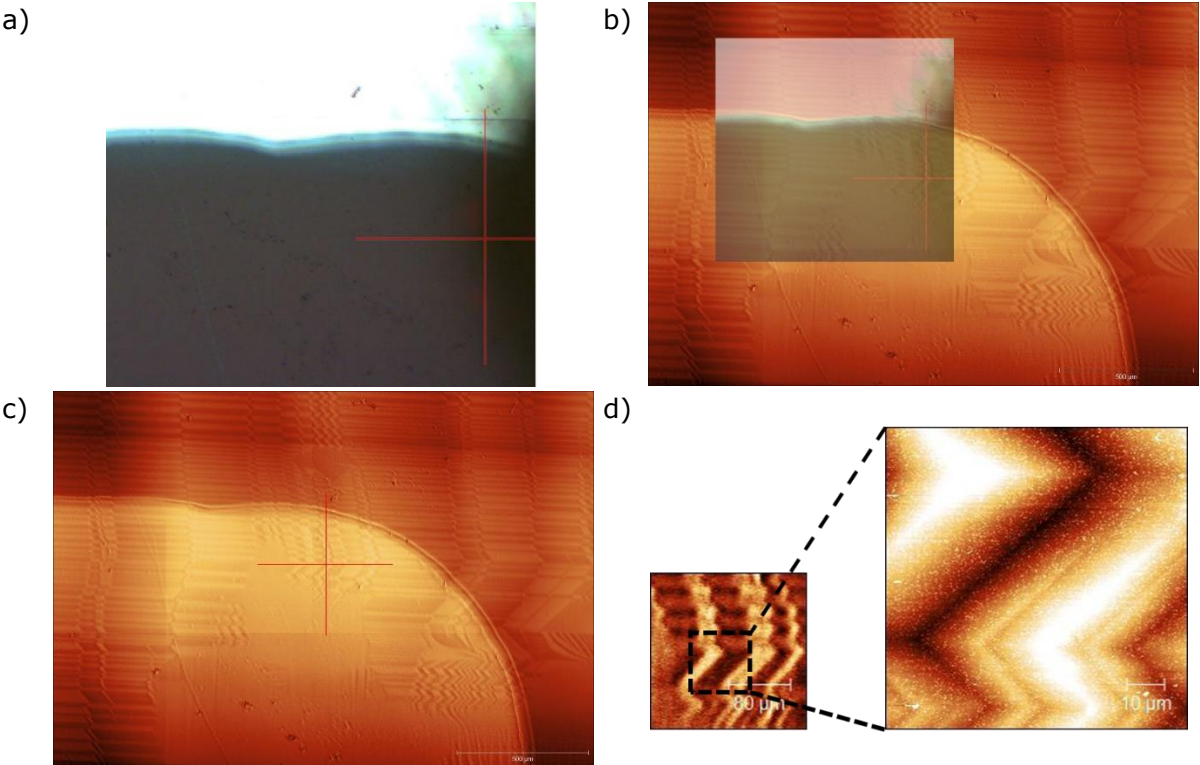
Figure 5.13. AFM image of the right high corner on many twins region for B1. a) is AFM microscopy image. The red cross line is the location where I measured by AFM b) is the layered AFM microscopy image on the 3D Optical Profiler Images before drawing a red cross at the measurement area. c) is the 3D optical profiler image with only the red cross which indicated the measurement region. d) images are a zoomed-in part of the 3D optical image and the AFM image of 80x80 μm^2. for the location indicated by the crosshair. The left one is the 3D Optical Profiler image cropped, the black dash line is the actual size for 80x80 μm^2 at the measured region, and the right one is the AFM image for 80x80 μm^2. They are exactly matched.

5.2.2 AFM images and 3D profiler images on B1

In the previous section explained how I was able to find the exact location using the AFM optical microscope and the 3D optical profiler. In this section and the following, I will present AFM images overlaid on the 3D profiler images to clearly show what positions on the sample the AFM images were taken.

In Fig. 5.14 AFM images are shown on top of the 3D optical profiler images taken on the same part of the sample; the upper two AFM images on the right-hand side are 2x2 µm^2 and 10x10 µm^2 images, and the lower three images are 20x20 µm^2, 40x40 µm^2 and 80x80 µm^2. I have also included a zoomed-in 3D Optical profiler image with the crosshair in a black and white color scale. The black and white color scale is chosen because it emphasizes the surface topography better than the other color scale.

As we can see, 2x2 µm^2 AFM image shows some hillocks like rods or clusters, on top of a smoother background. As the image size gets bigger, the hillocks naturally get smaller, and the number of hillocks rises. Finally, the hillocks can hardly be seen in the image size at 80x80 µm^2, and the background (i.e., except hillocks) appears as (tweed like) twin domains.

I classified three types of location such as twin, mixed, and flat. This section will explain the features of the three different areas.

Results from the twinned regions on B1

In this section, I will present AFM images from the twinned areas.

Figures 5.15 to 5.17 show images from the twin areas. The location number is from Figure 5.10, and it makes understanding the location easier. We can see the twin from 40x40 µm^2 AFM images, even 10x10 µm^2 for location number 2 image. Because of this, we could comprehend that these regions are twin areas. Unfortunately, in the location number 4 image, 2x2 µm^2 image could not be taken due to the measurement error. Figure 5.15 exhibits some dots; they are higher and larger than hillocks at 40x40 and 80x80 µm^2. Some AFM images have a white dash line on the image, and this means that the area only calculates roughness. In Figures 5.13 and 5.14, the size of 20x20 µm^2 images illustrates the different methods from 5.12. Since the images are too dark, they cover the color scale of 0-10nm instead of 0-30nm. Furthermore, for Figure 5.13, 20x20 µm^2 actual size is smaller than 20x20 µm^2 in that it has errored during the measurement. The locations number 1 and 4 for 10x10 µm^2 images have striped patterns in the background. Figure 5.13 for 10x10 µm^2 has diagonal stripes from the top right to the bottom left, and Figure 5.15 for 10x10 µm^2 has two types of strips. The upper area has diagonal stripes from the top left to the bottom right, and the lower stripes are horizontal. In Figure 5.14 for 40x40 and 80x80 µm^2, the actual size is different at 40x33.8 µm^2 and 80x53.8 µm^2, respectively, as I cropped the images because of a hole in the films.
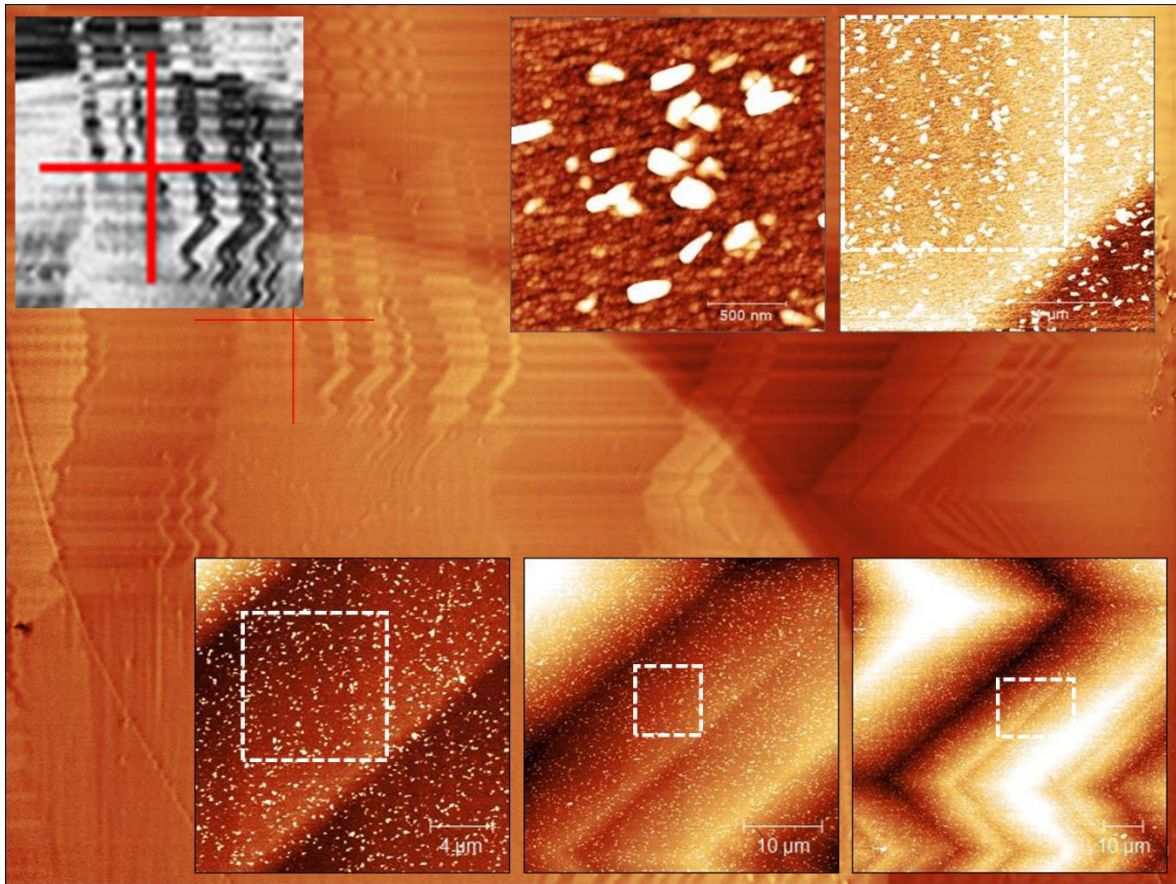
Figure 5.14. illustrates AFM images 2x2 μm^2,10x10 μm^2, 20x20 μm^2, 40x40 μm^2, and 80x80 μm^2 on top of the 3D Optical Profiler image with the red cross at the measurement region. The small black and white image is the 3D Optical Profile image, in which I wanted to show the twins or flat areas more emphatically. The upper row are 2x2 μm^2,10x10 μm^2 AFM images, and the lower row three images are 20x20 μm^2, 40x40 μm^2, and 80x80 μm^2, respectively. The AFM 2x2 and 10x10 μm^2 images have 0-10nm color range. The lower row three images are 20x20, 40x40, and 80x80 μm^2 images covering the 0-30nm. The 3D optical profiler image covers 0-4 μm, and the size is 1.9mm X 1.5mm. For the white dash line on the AFM images, I used the area when calculating the roughness. This image is location number 2 of B1.
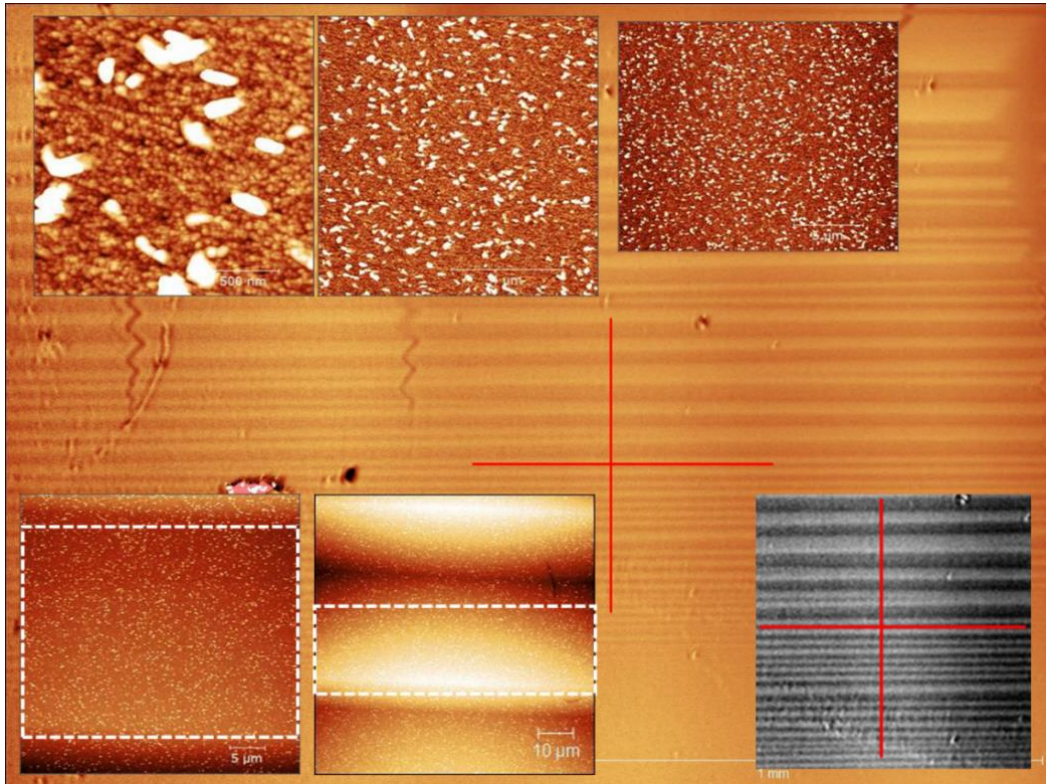
Figure 5.15. The location number is 1 of B1. The twin region on the left down 2 for B1 on LAO AFM and 3D Optical Profiler images. For 20x20 μm^2, actual size is 20x16.80 μm^2 because of the measurement error. For the other images, the illustrated method is identical with Figure 5.12
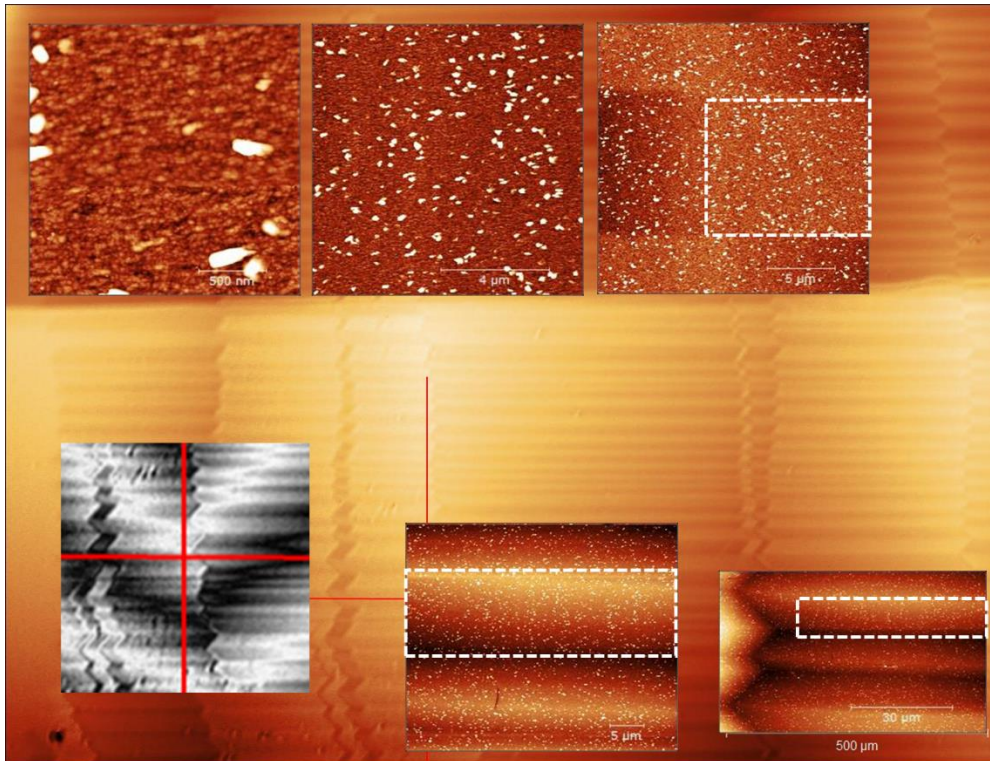
Figure 5.16. The location number is 3 of B1. The twin region on the right up2 for B1 on LAO AFM and 3D Optical Profiler images; the illustrated method is identical with Figure 5.12.
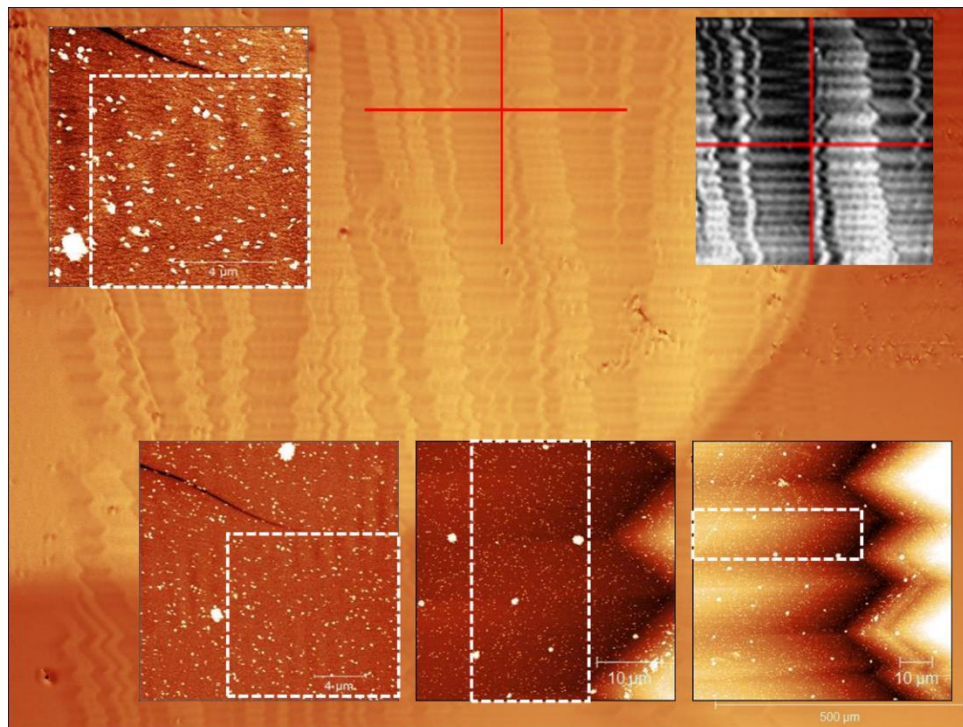
Figure 5.17. The location number is 4 of B1. The twin region on the right low for B1 on LAO AFM and 3D Optical Profiler images; the illustrated method is identical with Figure 5.12

Results from the mixed regions on B1

Next is the mixed regions which cannot be classified as twin or flat. Figures 5.18 to 5.21 are the mixed areas. Unfortunately, Figure 5.17 for 80x80 µm^2 could not be taken owing to the error in measurement. Figure 5.16 has pretty much spike or dust, so I calculated the roughness using some specific regions of the images (white dahs lines). The spike or dust are shown continuously from 2x2 µm^2 to 80x80 µm^2. Figure 5.18 for 80x80 µm^2 image seems to be twins, yet it is not clear. Thus, I decided to classify it as a mixed area. Figure 5.19, from 10x10 to 8 0x80 µm^2, sequentially exhibit the vertically dark and bright patterns. In these regions, the stripe patterns are also shown in the background (except the hillock area). Figure 5.16 for 10x10 µm^2 image has vertical lines, and Figure 5.19 for 10x10 and 20x20 µm^2 images have the same diagonal stripes between the right high and left low in the image.
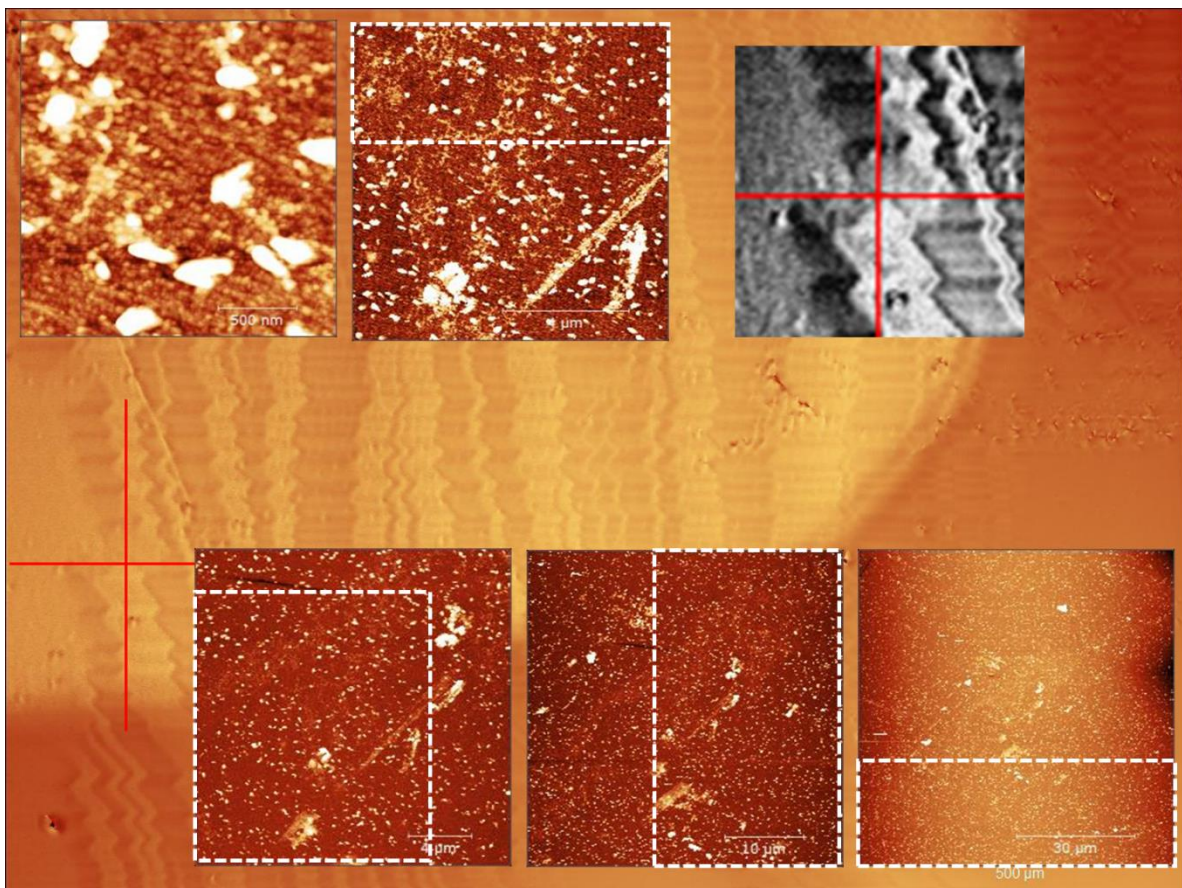
Figure. 5.18. The location number is 5 of B1. The mixed region on the right low for B1 on LAO AFM and 3D Optical Profiler images; the illustrated method is identical with Figure 5.12
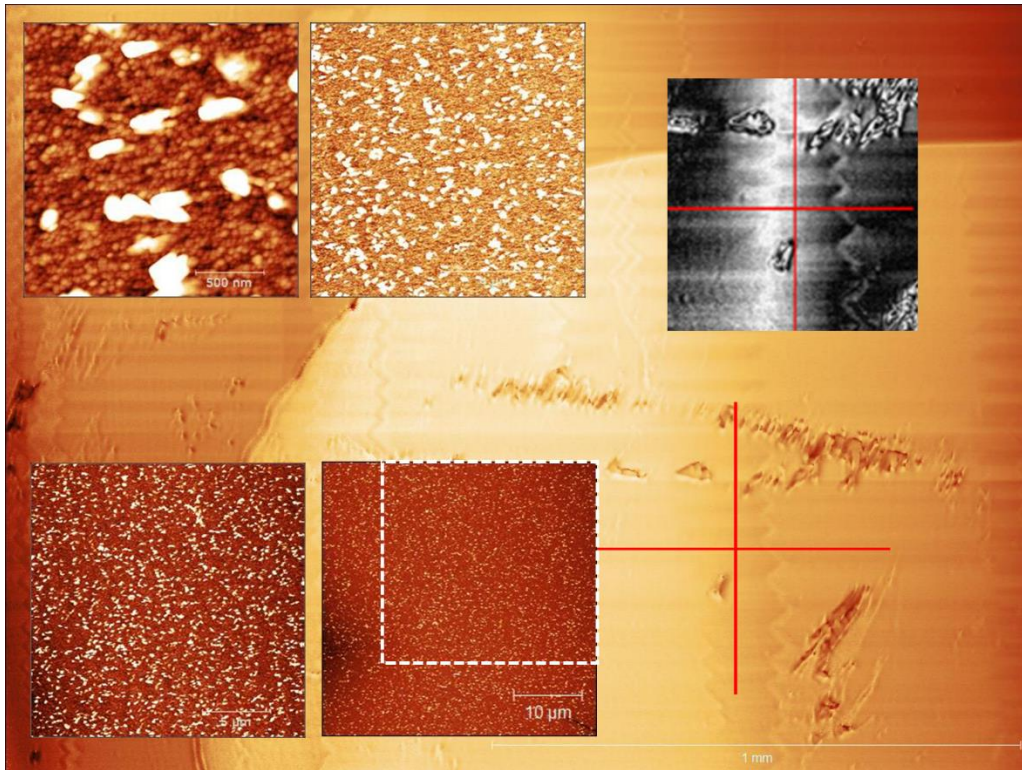
Figure. 5.19. The location number is 6 of B1. The left high 1 for B1 on LAO AFM and 3D Optical Profiler images; the illustrated method is identical with Figure 5.12.
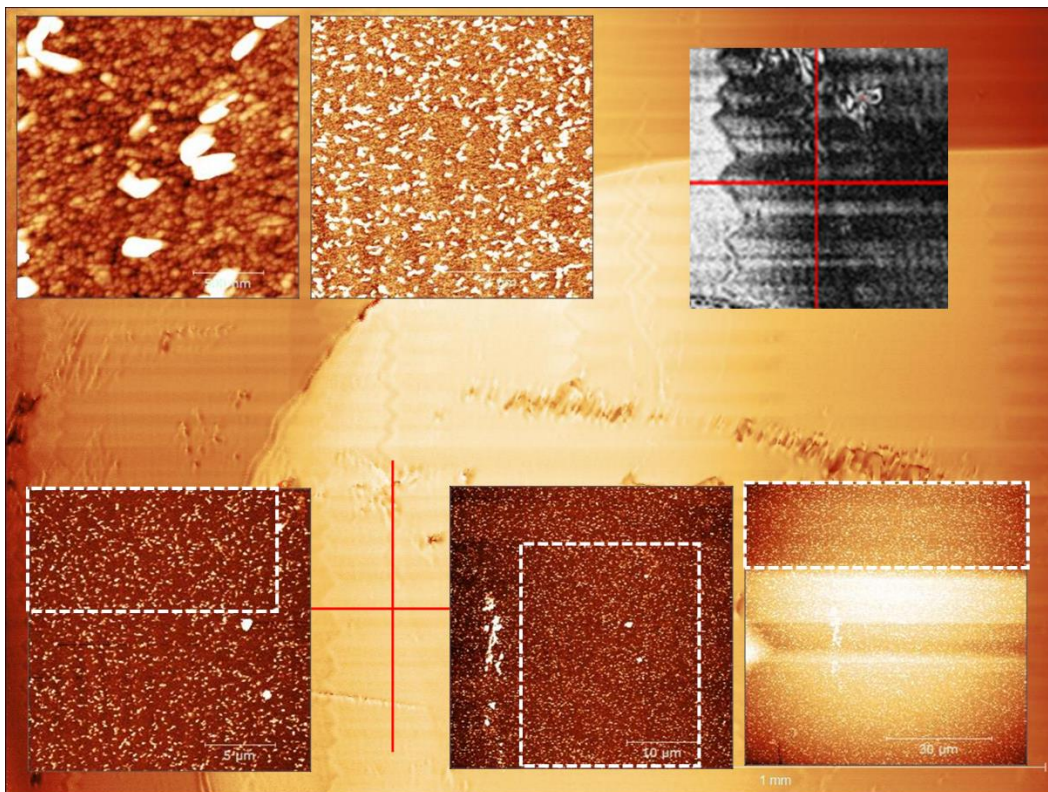
Figure 5.20. The location number is 7 of B1. The mixed region on the left high for B1 on LAO AFM and 3D Optical Profiler images; the illustrated method is identical with Figure 5.12.
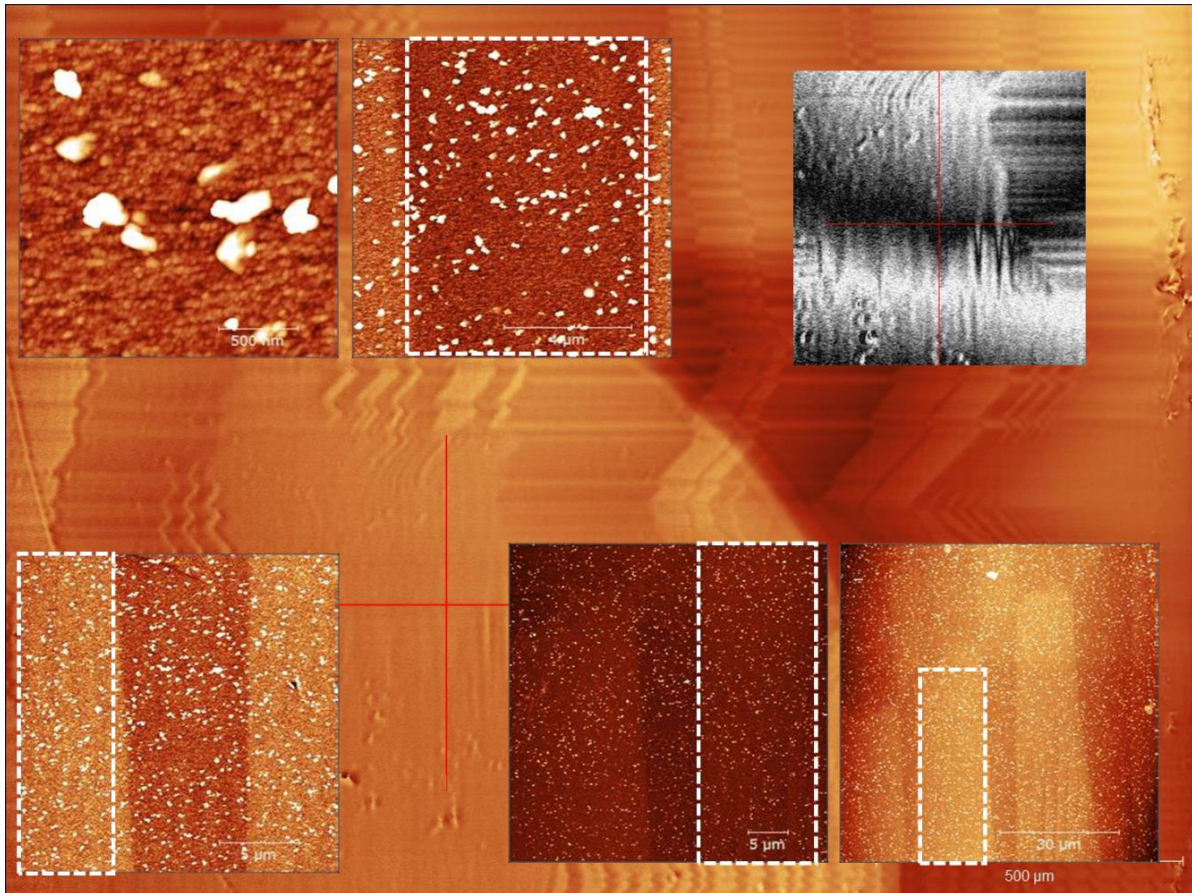
Figure. 5.21. The location number is 8 of B1. B1 on LAO on the right high corner. The method described is the same as Figure 5.12

Results from the flat regions on B1

In this section, I would like to explain the flat region for B1. Figures 5.22 to 25 are the flat areas. Although Figure 5.20 has many scratches, we decided to classify it as the flat region because of the background. When it was zoomed out, we were able to find the contaminations. Furthermore, this 3D optical profiler image is from the full stitching image because I could not find the region from the left low image of the 3D optical profiler. Even though it is from a stitching image, it is zoomed in; so, there are no stitching lines. The size of the 3D Optical Profiler image is the same as other 3D Optical profiler images. Like twin and mixed areas, some flat AFM images show striped patterns. Figures 5.21 and 5.22 for 10x10 μm^2 images have vertical stripes in the background, and Figure 5.23 for 10x10 and 20x20 μm^2 images have the same diagonal lines from right high to left low. Figure 5.21 for 10x10 μm^2 image is actually taken at 10x9.84 μm^2 due to measurement error. Likewise, in Figure 5.23, for 40x40, owing to the same reason above, the actual size is 40x39.5 μm^2.
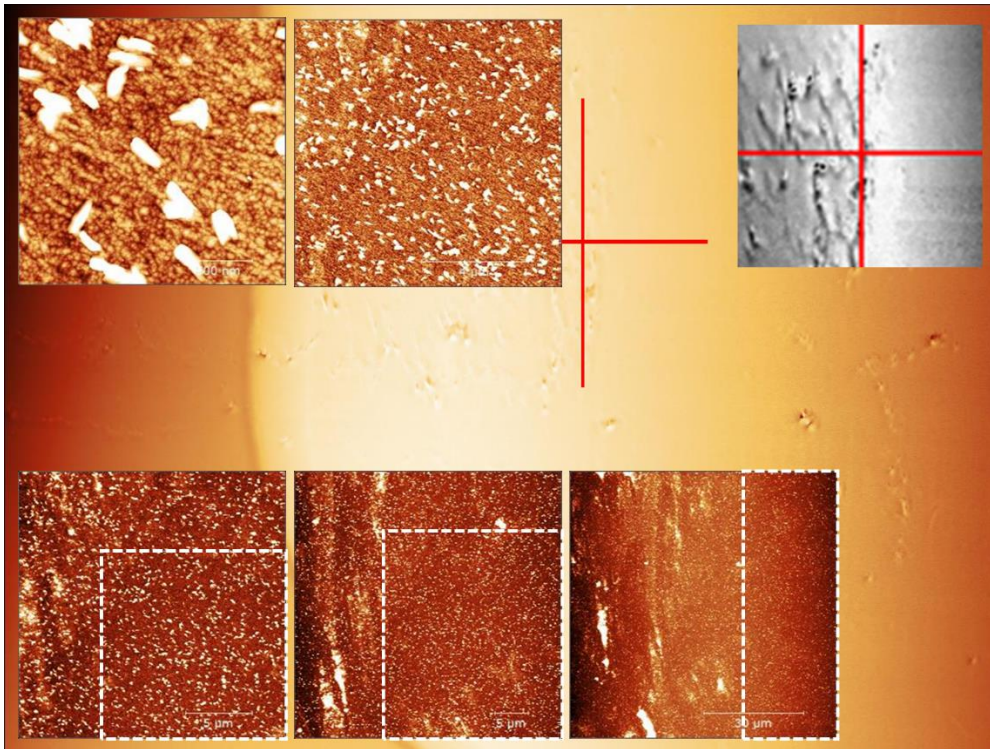
Figure 5.22. The location number is 9 of B1. B1 on LAO on the left low corner. The method described is the same as Figure 5.12
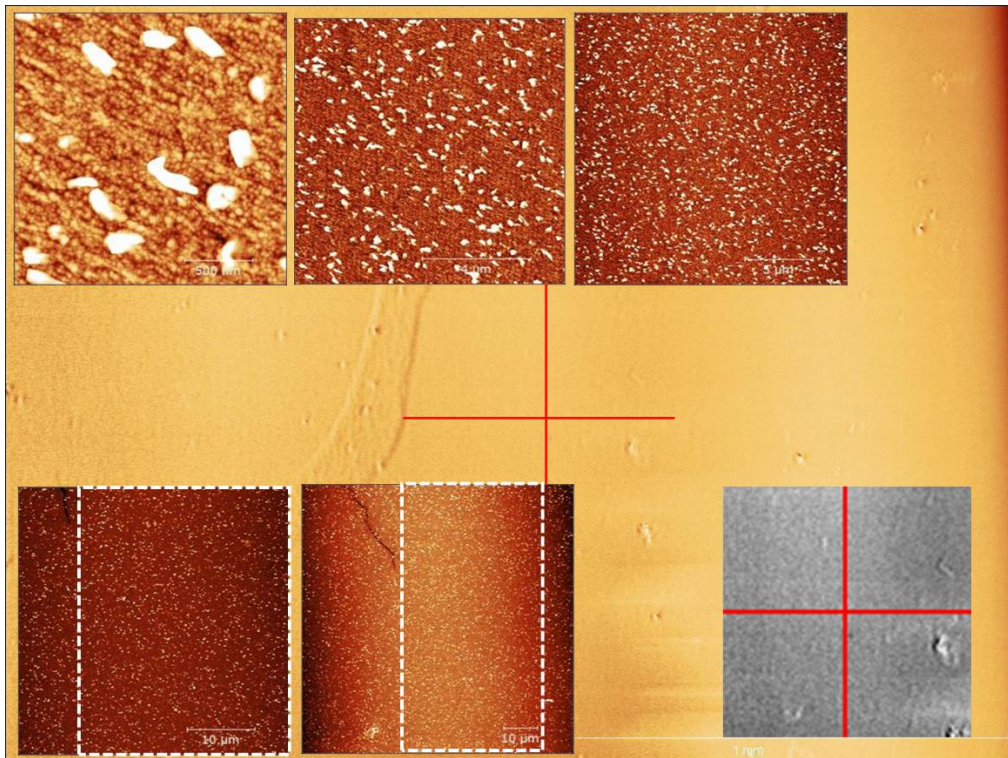
Figure. 5.23. The location number is 10 of B1. B1 on LAO on the left down 1. The method described is the same as Figure 5.12
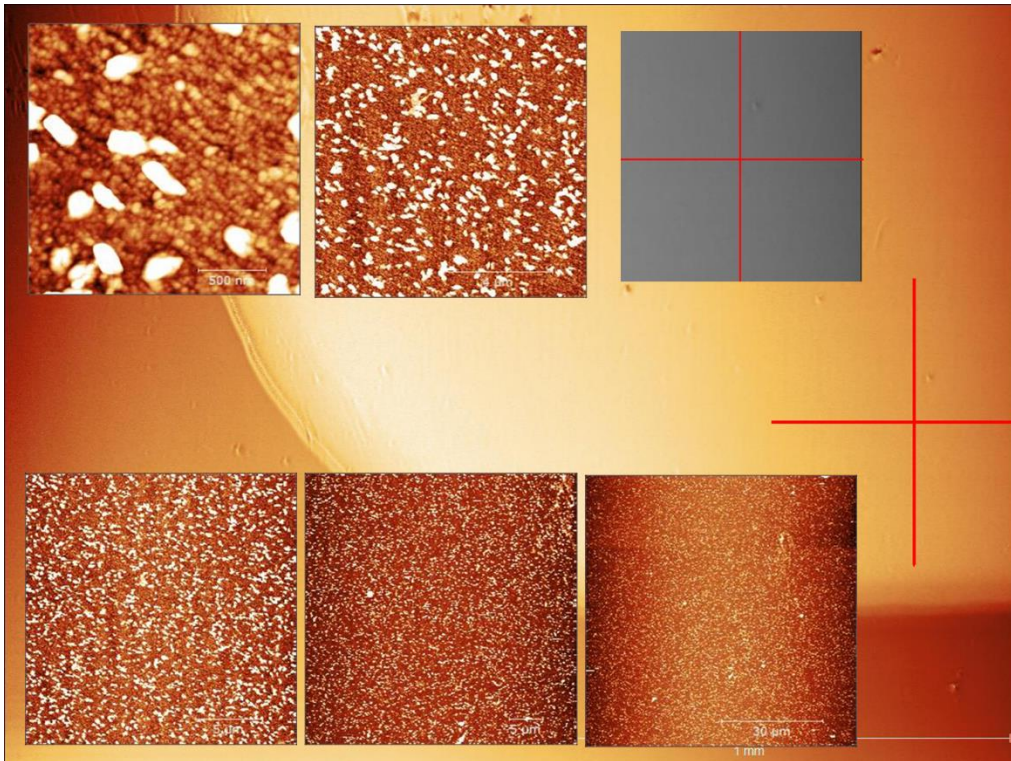
Figure 5.24. The location number is 11 of B1. B1 on LAO on the right low corner. The method described is the same as Figure 5.12
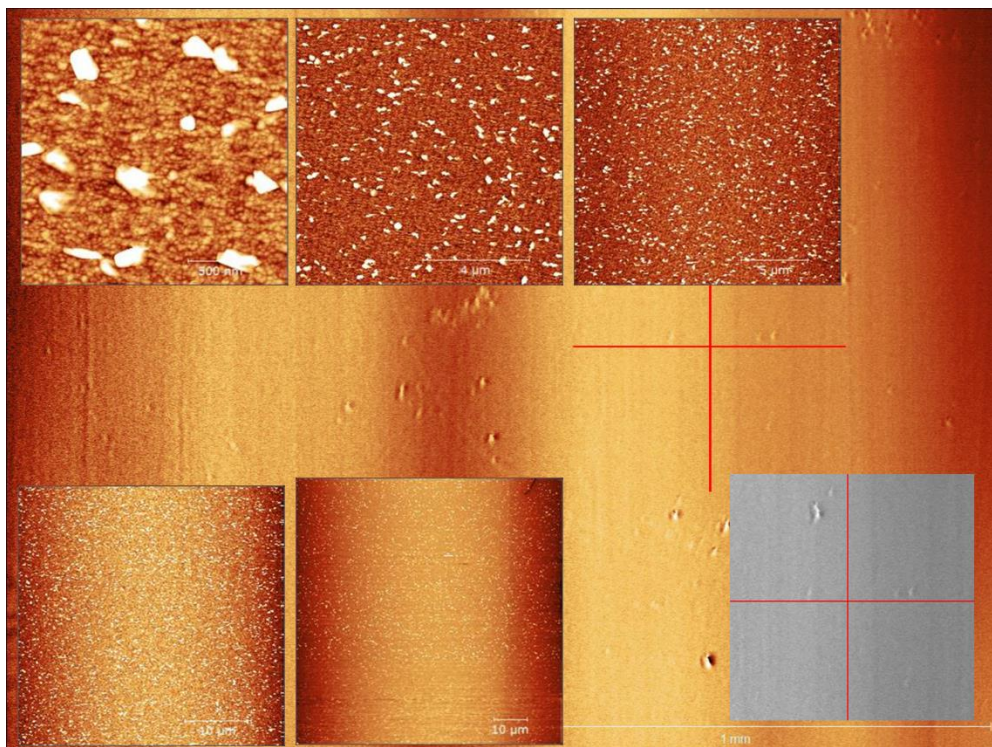
Figure 5.25. The location number is 12 of B1. B1 on LAO on the right up 1. The method described is the same as Figure 5.12

Discussion

One of the most outstanding features of B1 images is the hillocks since every AFM image shows the hillocks. As I will be discussing again with B5 AFM images, only B1 AFM images show the hillocks. Hillocks look like needles, clusters, or rods, and they are nucleations during the deposition. They might be TiO_2, Ti, O_2 or TiO_{2-x}, etc.; I could not determine what they are precise. Moreover, the size of hillocks is diverse; as we can see in Figure 5.15, they are sometimes significantly vast, while some others are pretty tiny. Figure 5.26 shows the 3D images of the AFM images for 10x10 and 80x80 μm^2.

a)

b)
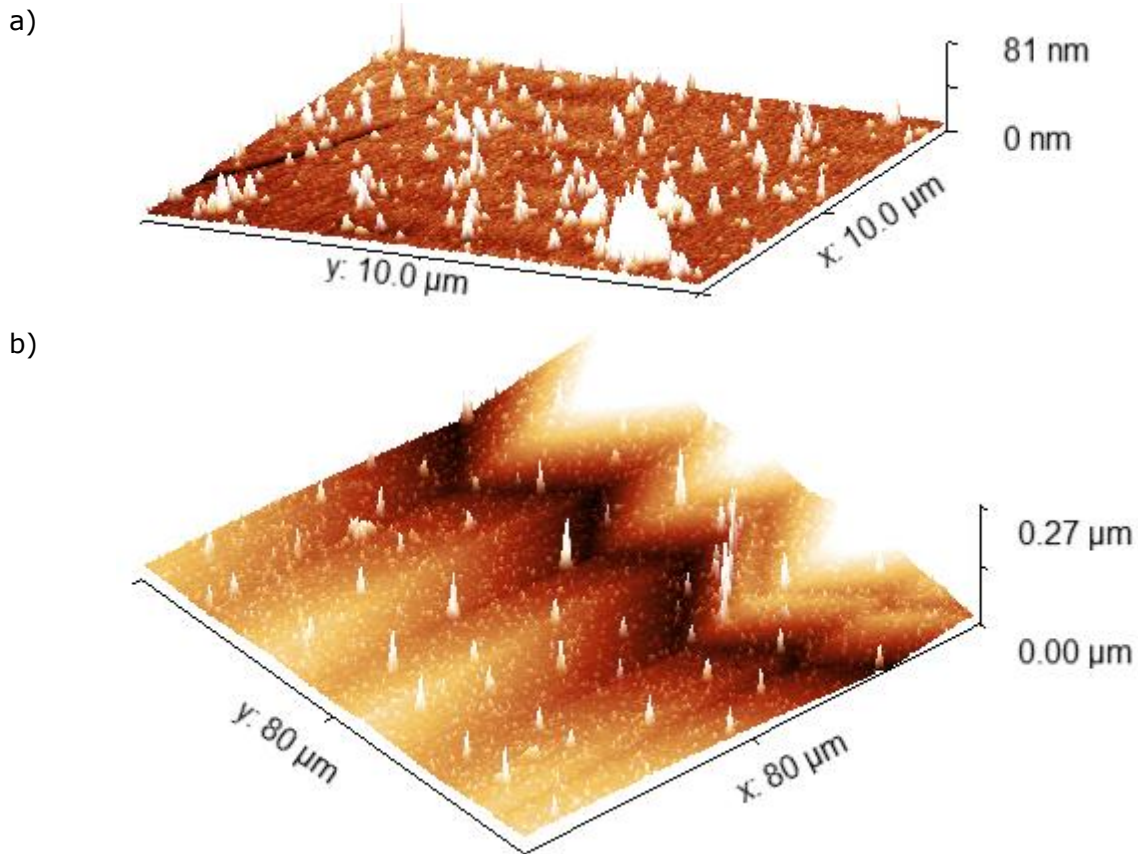
Figure.5.26. 3D images of AFM for location number 4 of B1. a) is the 10x10 μm^2 image, where there is one of a more extensive and higher hillock. b) is the 80x80 μm^2 image, wherein the valley, hill, and side of the twin there are more significant and taller hillocks than other small hillocks.

Among the twin, mixed and flat areas, the number of hillocks is not greatly affected by the regions since the numbers are pretty random. To explain in more detail, for 2x2 μm^2 AFM images, the lowest number of hillocks is 16 for location 8 in the mixed area, and the largest number is 60 for location 5 in the mixed area, too. Both the smallest and the biggest numbers are in the mixed area. The most significant number of hillocks is due to dust or spikes. Except for those regions, the number of hillocks is between 23 and 38, and I think it does not make a significant difference. Although only twelve regions are measured, I cannot say for certain that better-ordered areas such as flat and twinned regions can have the nucleations pretty uniformly. On the other hand, the mixed areas or less ordered regions, have uneven hillocks.

In general, 80x80 µm^2 images are similar to 3D Optical Profiler images. As I have figured out the location using AFM microscopy, the 80x80 µm^2 images are identical to 3D optical profiles. Thus, I could classify three categories of the regions, and I am able to say 3D Optical Profiler images and AFM images are linked.

As I mentioned in the results, some AFM images show the striped patterns in the background. I can not say whether it is a step height or a terrace; however, they seem similar to the terrace. For 2x2 µm^2, images can be exhibited even more specifically, despite the patterns being significantly random.

5.2.3 AFM images and 3D profiler images for B5

Like B1, I decided to measure region B5 on LAO; the areas are described in Figure 5.27; in addition, the method of display for 3D Optical Profiler and AFM images is identical with B1.
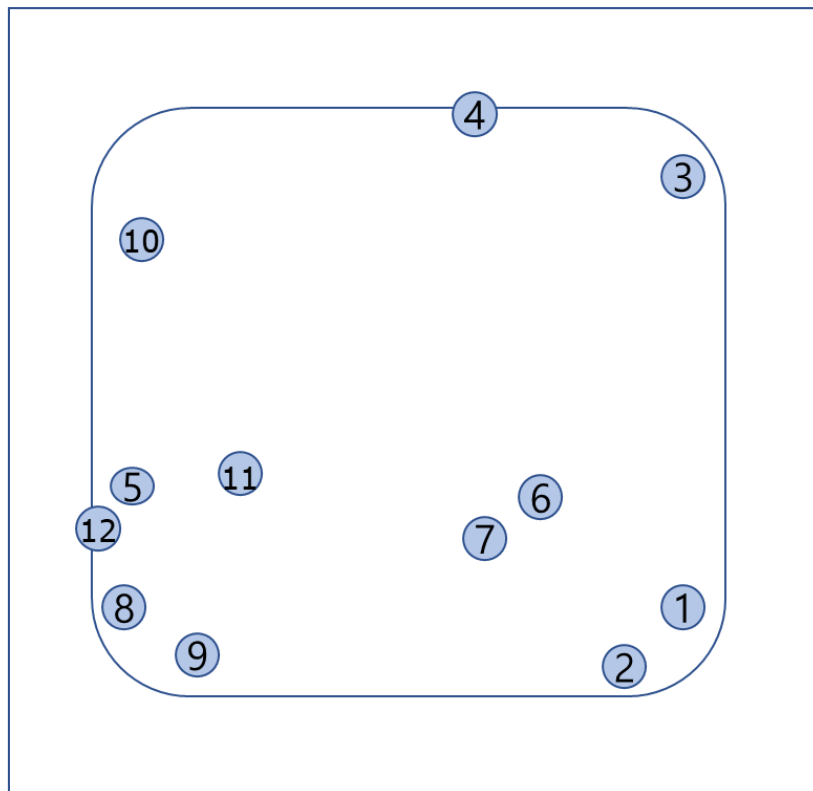
Figure. 5.27. B5 films on LAO substrate where I measured AFM approximately. The blue color circles are the locations. For B1, 1-4 are twins, 5-8 are mixed, and 9-12 are flat areas.

Results from the twinned regions on B5

In this section, I will describe the twin area of B5. Figures 5.28-5.31 are twin regions in B5 on LAO; these twins are ordered vertically. Figures 5.28 and 29 for 80x80 μm^2, the size is 80x80 μm^2; however, the displayed images are shrunken in size to show the measurement region (the red cross line). Unlike B1, the B5 series do not have hillocks, but instead of hillocks, they look like step height or terrace – the striped patterns. Not only in 2x2 μm^2 AFM images but also in 10x10 to 40x40 μm^2 images, step height can be seen. For the 80x80 μm^2 image, the terrace patterns cannot be seen; instead, they show twin surfaces. Like twin patterns, the step height is almost vertical for every 2x2 μm^2 image; conversely, from 10x10 to 40x40 μm^2, the terrace patterns are diagonal or vertical. They are located along the surface of the twin morphology. Like B1, the white dash line area is where the roughness is calculated. Some 80x80 μm^2 have had some contaminations, and some of them might look like hillocks – white dots.
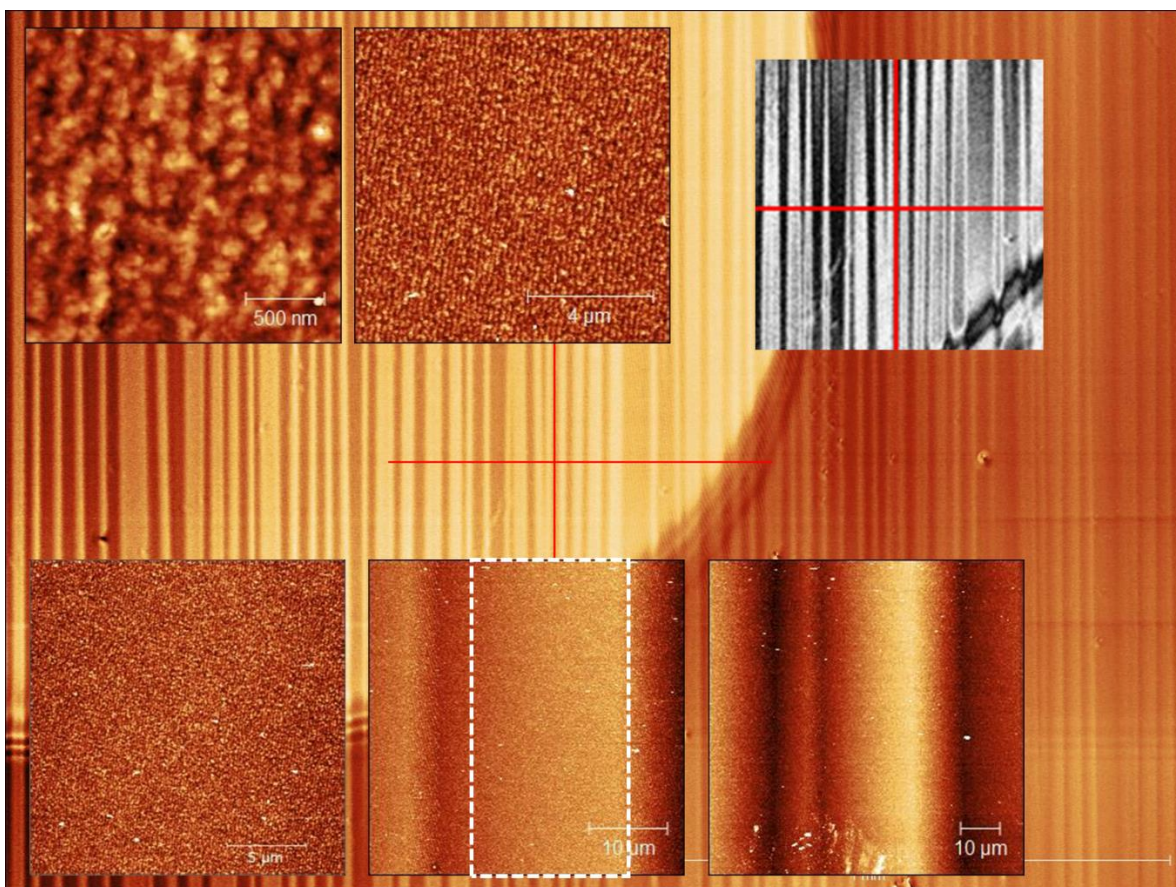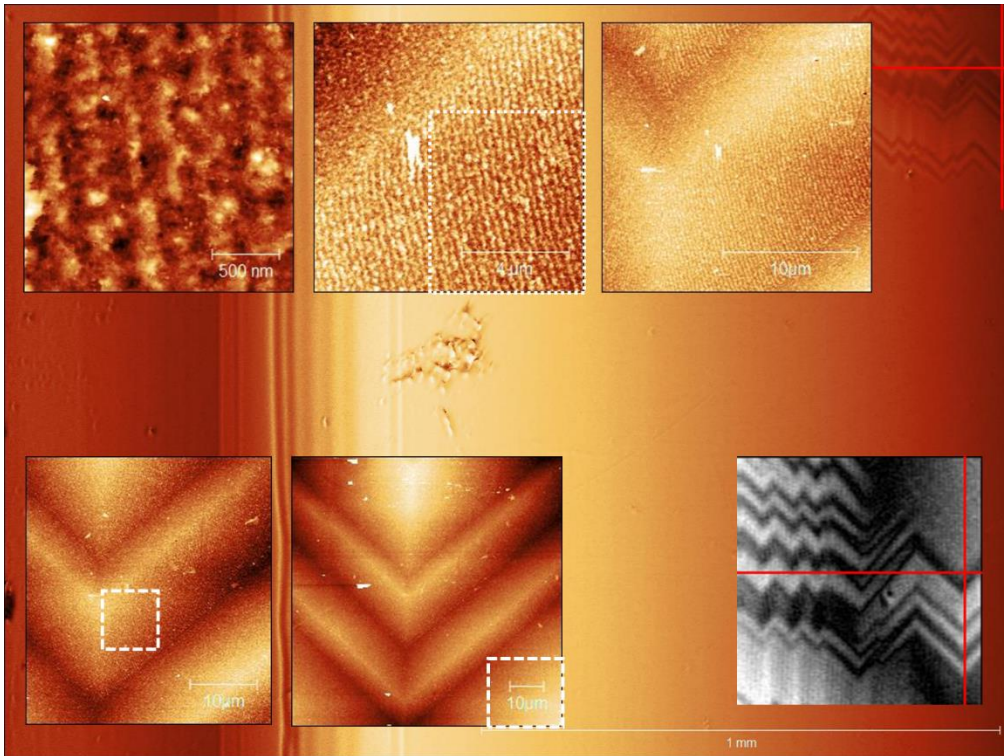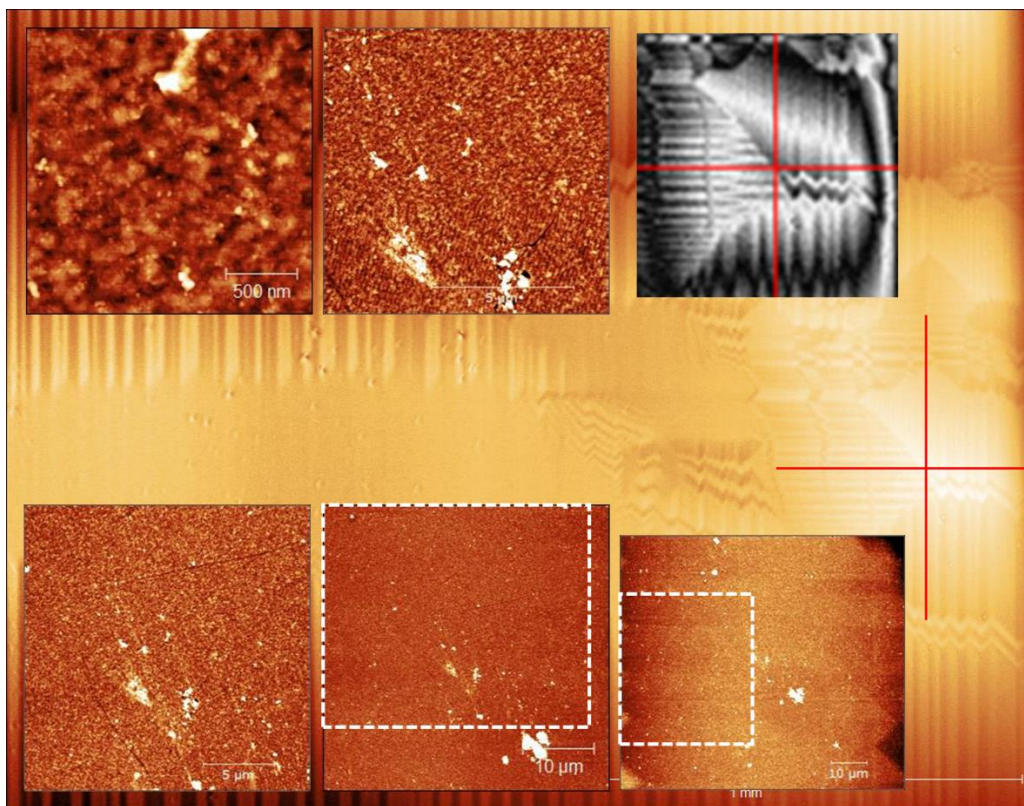

Figure. 5.28. The number 1 area of B5. B5 on LAO right low corner. The method described is the same as Figure 5.12
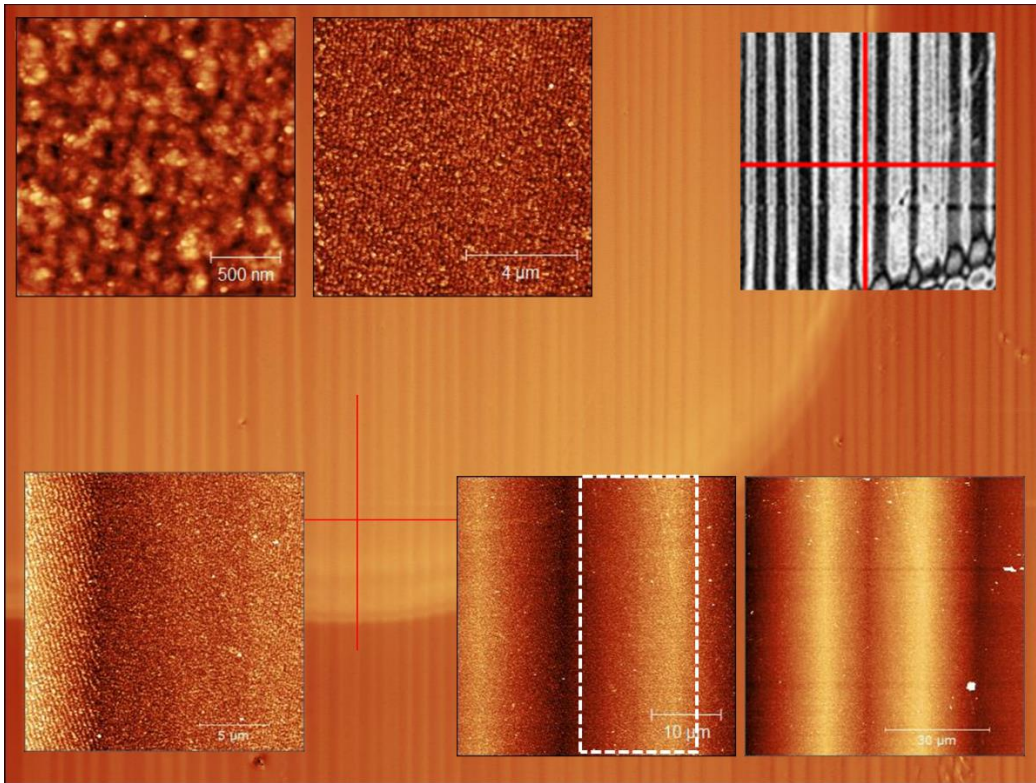
Figure. 5.29. The number 2 area of B5. B5 on LAO right low corner. The method described is the same as Figure 5.12.
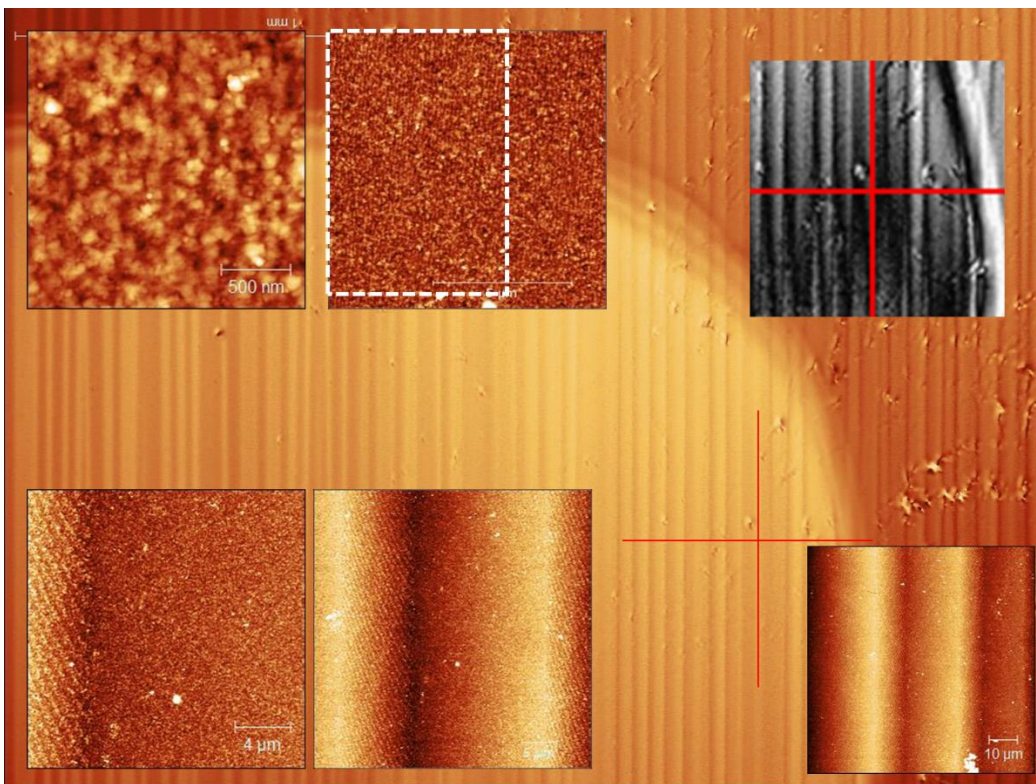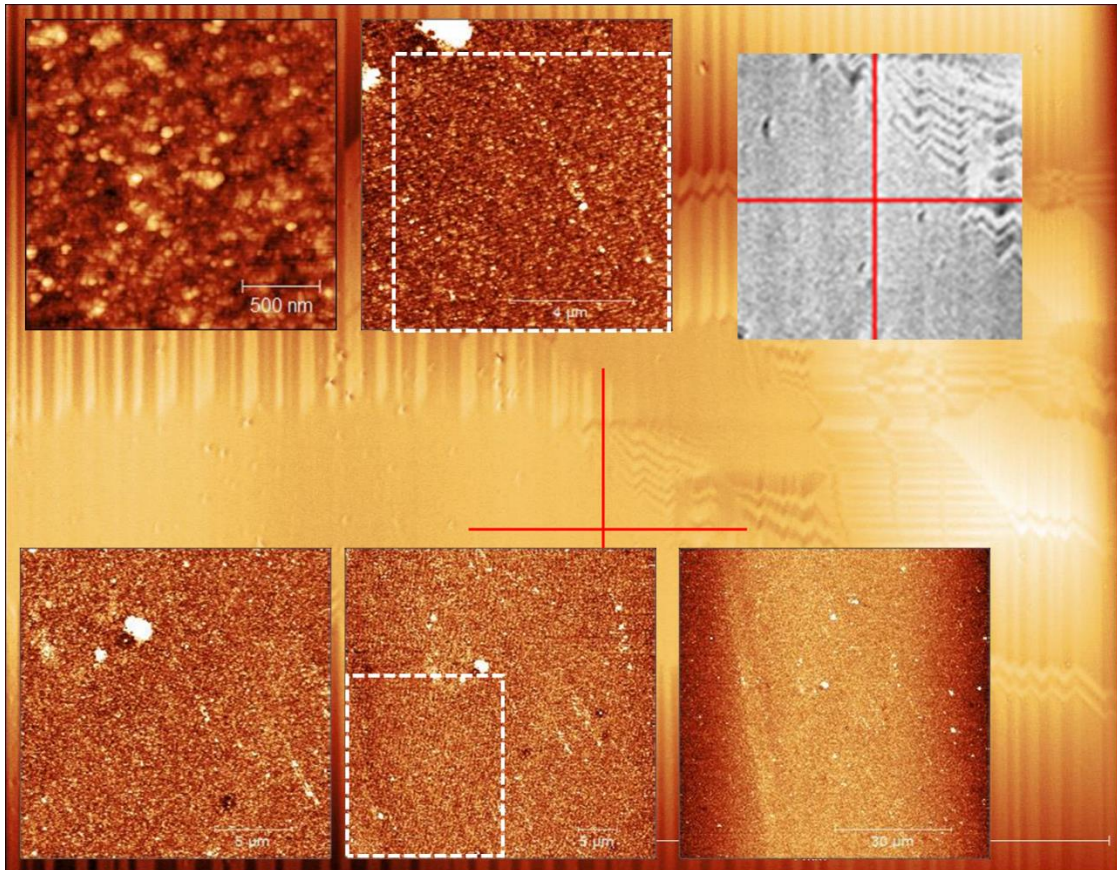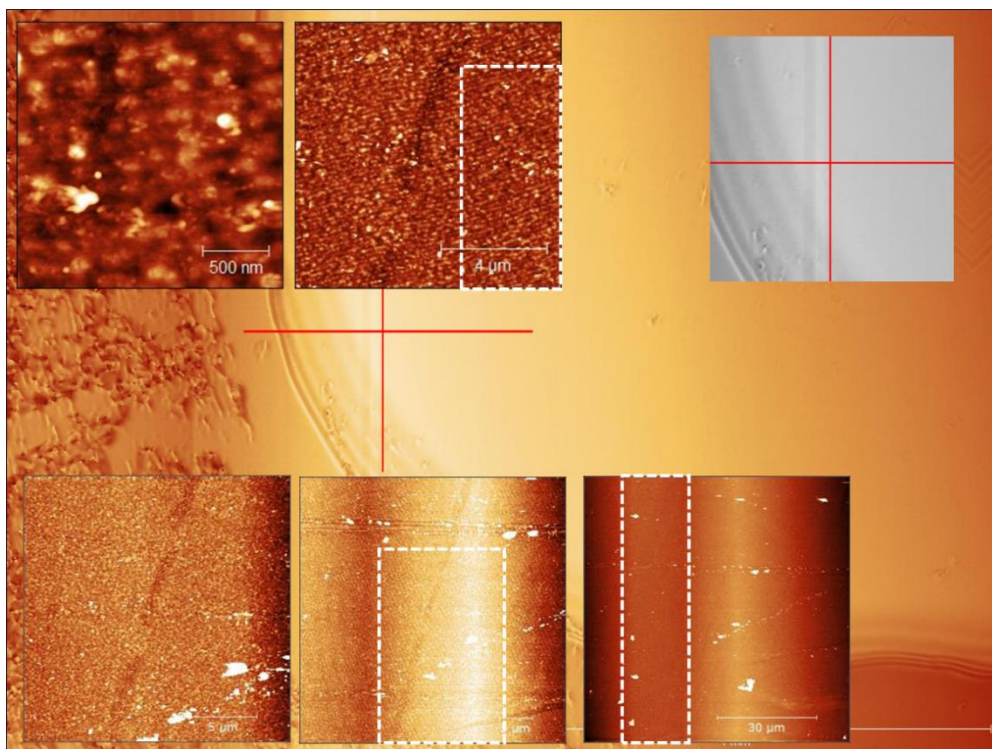

Figure. 5.30. The number 3 area of B5. B5 on LAO right high corner. The method described is the same as Figure 5.12.
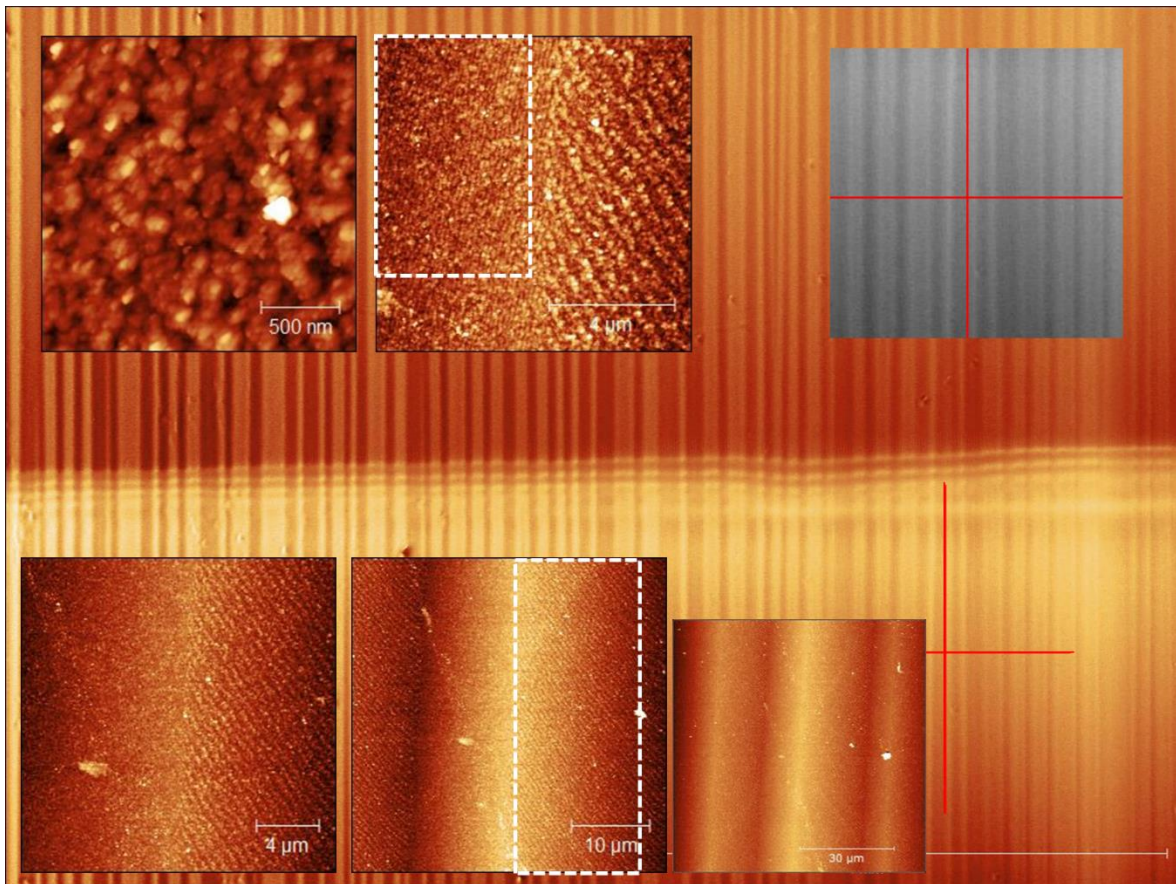
Figure. 5.31. The number 4 area of B5. B5 on LAO right up 1. The method described is the same as Figure 5.12

Results from the mixed regions on B5

Next, the mixed regions in B5 on LAO are illustrate. Like B1, these mixed areas are also classified as neither twin nor flat. Figure 5.32 has wiggle twins and flat mixed; Figure 5.34 is flat and mixed twinned areas which can be seen in the 3D Optical Profiler image and AFM image for 80x80 µm². On the other hand, Figure 5.32 looks flat, and there is a small wiggle twinned pattern. Figure 5.32 for 20x20 µm2 is too dark, so I displayed it on the same color scale as 10x10 µm². The noticeable feature is also that they have stripes like step height or terrace, from 2x2 to 20x20 µm² images like twin areas. The difference is in the angle of the striped pattern for 2x2 µm² - in figure 5.32, the patterns are close to vertical; in contrast, Figures 5.31 and 5.32 are similar to horizontal terrace patterns. Features of Figure 5.34 are like a twin area; however, figure 5.33 has similar flat features. Figure 5.33 has the features of both Figures 5.32 and 5.34. In Figure 5.33, the actual size of 80x80 µm² is 80x70.6 µm² due to measurement error. In Figure 5.32, the striped patterns for 2x2 to 20x20 µm² are located along the surface of the wiggle twin.

Figure. 5.32. The number 5 area of B5. B5 on LAO left edge. The method described is the same as Figure 5.12

Figure. 5.33. The number 6 area of B5. B5 on LAO right down 1. The method described is the same as Figure 5.12
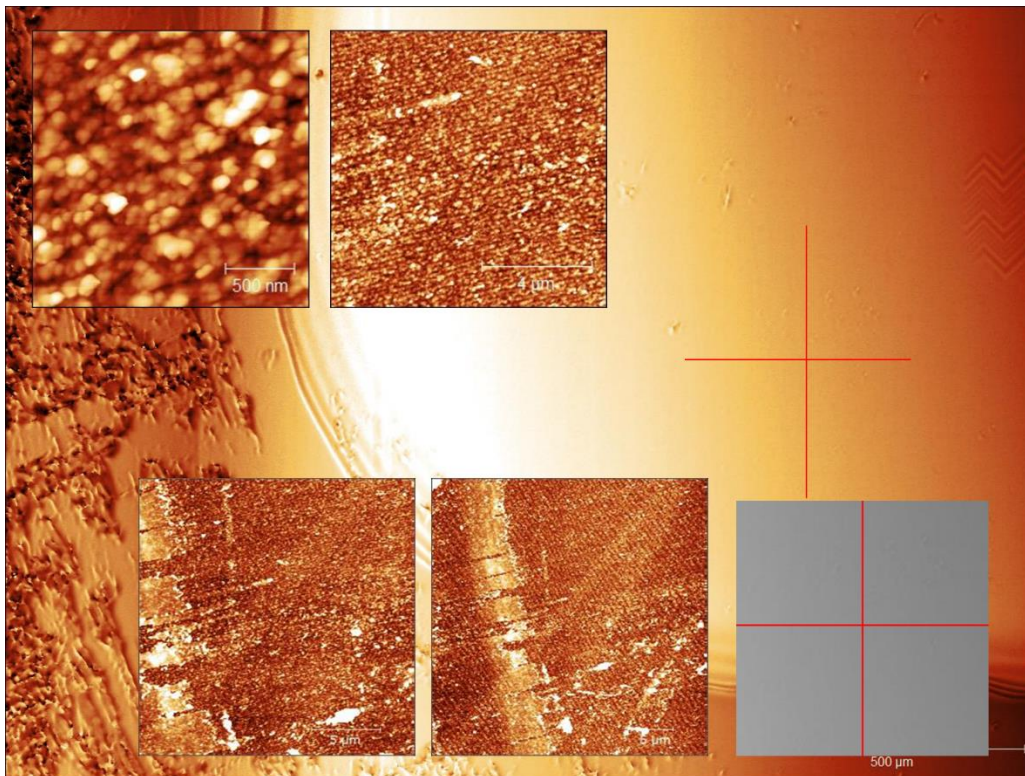
Figure. 5.34. The number 7 area of B5. B5 on LAO right down 1-2 The method described is the same as Figure 5.12

Figure. 5.35. The number 8 area of B5. B5 on LAO, the left low corner. The method described is the same as Figure 5.12

Results from the flat regions on B5

Lastly, the flat region will be explained. Figures 5.36 to 39 are flat areas of B5. Compared to previous Figures, the most notable thing is that the terrace's angle is relatively horizontal. Although each step height is different, the slope of the pattern is close to horizontal compared to the twin regions. Moreover, the striped pattern is well shown compared to twin or mixed areas. Unfortunately, Figure 5.36 could not be taken at 80x80 μm^2 because of measurement error. I believe the tip of AFM is contaminated, in that from 2x2 to 40x40 μm^2, we can continuously see the contaminations. Despite the contamination, in Figure 5.36, all AFM images are seen in the striped pattern, yet the 40x40 μm^2 image has a different terrace pattern – opposite to the diagonal stripes. Like Figure 5.36, Figure 5.38 for 40x40 μm^2 striped pattern is different from 2x2, 10x10 and 20x20 μm^2 image- the angle contrast. In Figure 5.39, the 20x20 μm^2 image is too dark, so I displayed an identical color scale with 2x2 and 10x10 μm^2 images; moreover, the actual size of 20x20 μm^2 is 20x18.83 μm^2 owing to the spike. The spike could be found on the 80x80 μm^2 AFM image in the middle. Like 20x20 μm^2 image, the real size of 40x40 μm^2 is also 40x28.6 μm^2 because of the same reason as the 20x20 μm^2 image. Figure 5.37 for the 3D Optical Profiler image is from the full stitching image since I could not find the measurement region from the normal left high corner image of the 3D Optical Profiler.

Figure. 5.36. The number 9 area of B5. B5 on LAO, the left low corner. The method described is the same as Figure 5.12
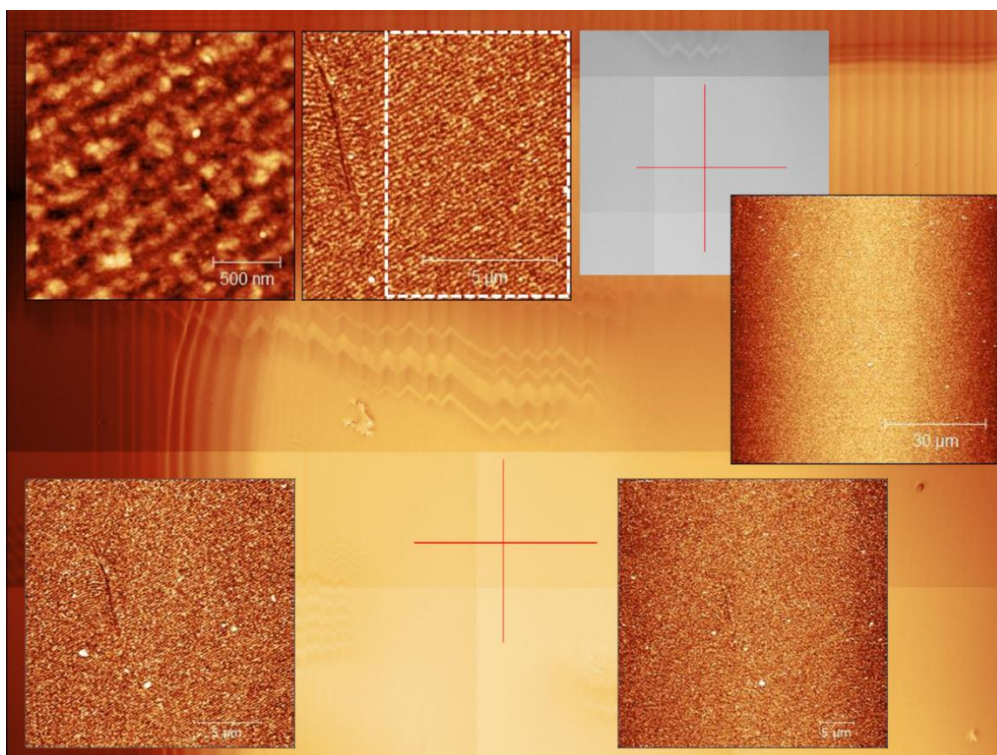
Figure. 5.37. The number 10 area of B5. B5 on LAO left high corner. The method described is the same as Figure 5.12
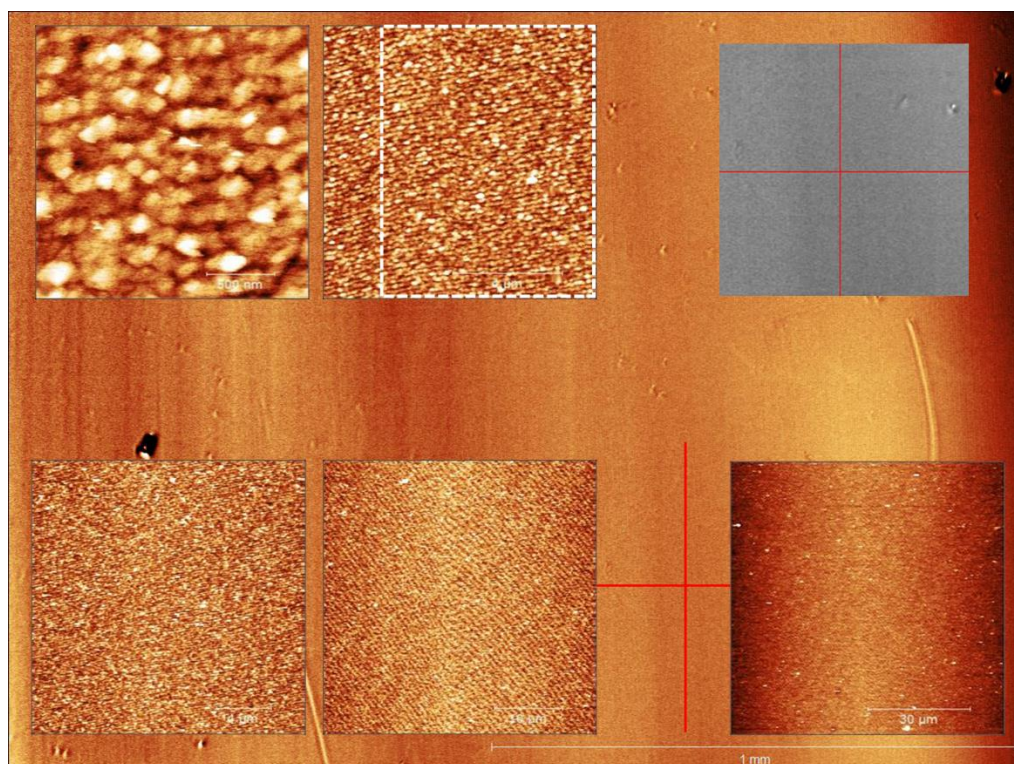

Figure. 5.38. The number 11 area of B5. B5 on LAO the left down. The method described is the same as Figure 5.12.
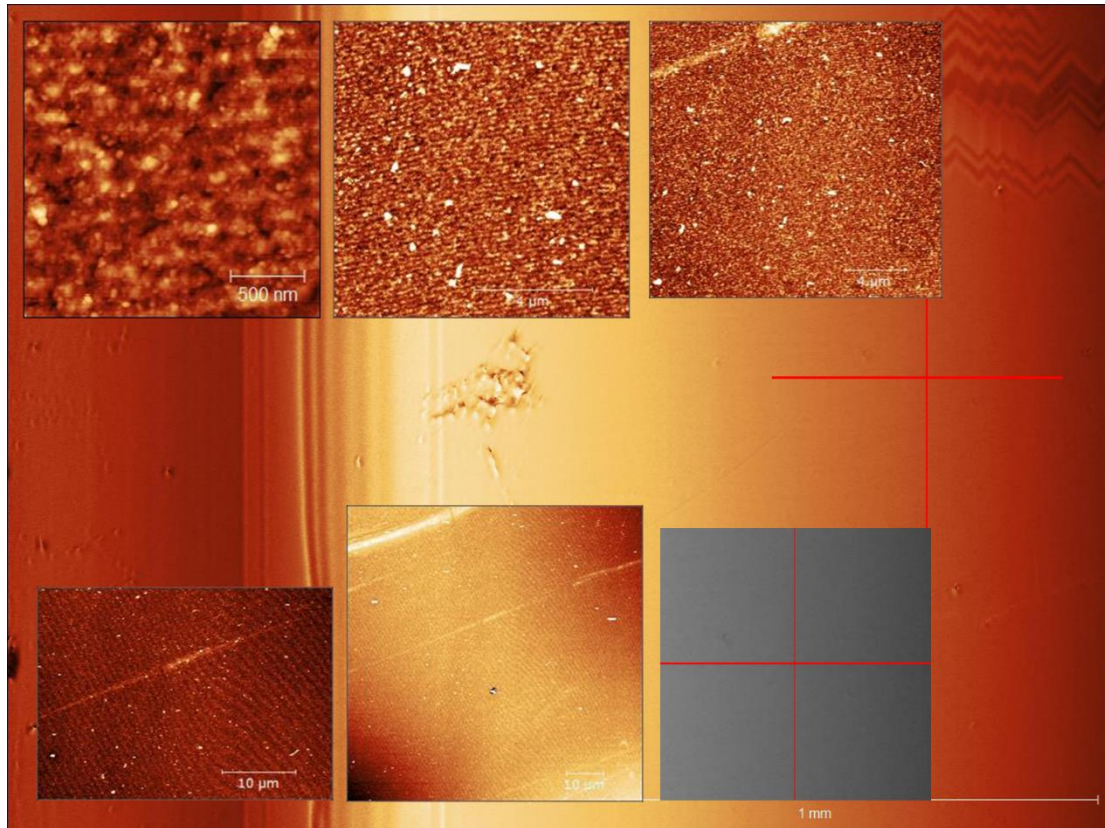
Figure. 5.39. The number 12 area of B5. B5 on LAO the left edge. The method described is the same as Figure 5.12

Discussion

The most noticeable feature is that the terrace is shown in all of the 2x2 µm^2 and 10x10 µm^2 images; additionally, 20x20 and 40x40 µm^2 images are also seen in the striped patterns. I believe that it means B5 is better-ordered than B1. The nucleations have been positioned more safely during the deposition. Thus, instead of creating hillocks or clusters, the nucleations regularly settle down on the surface despite some contaminations or clusters. Secondly, the property is that the terrace angle might be affected by the measurement region. In detail, in the twin region, the terrace pattern is usually vertical; on the other hand, in the flat area, the pattern is close to horizontal. This is because the terrace patterns are located along the surface of the region. Thus, when it is zoomed out, those patterns are formed in two different directions like Figure 5.31 and 5.37 for 10x10 µm^2 images. Furthermore, the terrace direction changed when it was zoomed out except in Figures 5.35 and 37. In the other 40x40 µm^2 images the patterns are formed in opposite directions or horizontal to diagonal from the top left to the bottom right. I believe that when they are zoomed out, the twin domain size changed, and then the shown domain might be two different domains or a broader domain. Figure 5.40 described the two domains, and they are from Figure 5.39 10x10, 20x20, and 40x40 µm^2. I figured out through the contaminations (arrowhead), for 10x10 µm^2, the terrace angle is close to horizontal. However, when it was zoomed out, the pattern shows two different directions.
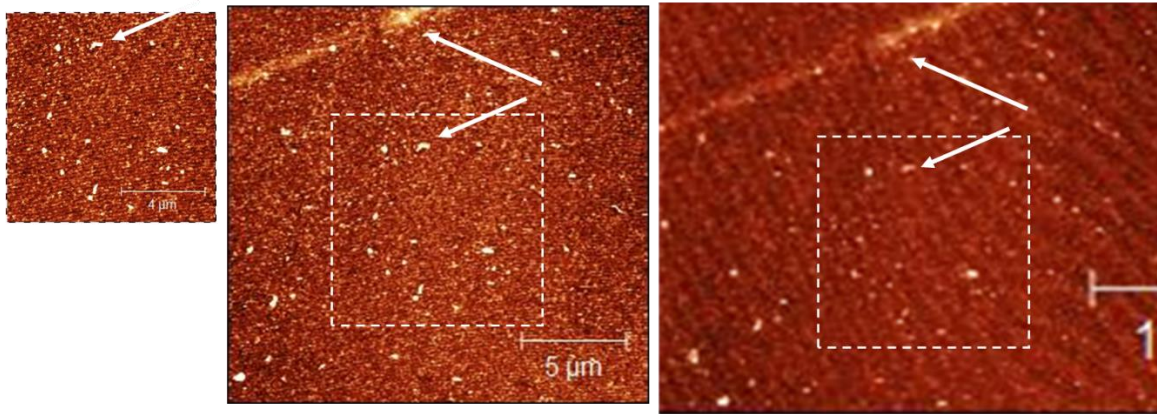
Figure. 5.40. The change in terrace pattern after zooming out for Figure 5.39 images.

Comparison of B1 and B5

Compared to B1 and B5, one of the most prominent properties is, I think, the hillocks. Both samples have identical deposition parameters, except the background gas ratio; B1 was deposited with 100% of argon, so B1 could not have enough oxygen. Although we are not sure of the inside of the plume, the nucleations gathered like clusters or rods. Therefore, the AFM image shows hillocks that look like rods or needles (Figure 5.26 illustrates this). From our previous work[44], B1 is metallic; therefore, it may be acknowledged that it is titanium suboxides. Even though we are not sure what they composite precisely, it could be Ti_nO_{2n-1}(n=integer greater than one) or Ti_2O_3, etc. Those materials are Magnéli phase. Titanium suboxides have an outstanding electric conductivity, which is similar to metal[45, 46]. Marina's work[44] is double-checked. Due to the lack of oxygen, the B1 looks like metal.

On the other hand, the B5 could have enough oxygen; also, the nucleations are more spread and better-ordered than the B1. Therefore, in the B5 images, more terrace patterns are easily found than in B1. Of course, we could figure out the striped pattern in B1 samples, yet it is faint.

Thus, I could calculate the terrace width for B1 and B5, especially the more clear terrace pattern ones. Figure 5.41 a) is 10x10 μm^2 of the AFM B5 image, the location is 1, and b) shows the periodic lines on the terrace pattern. I used the function 'measure lattice' from the Gwyddion program. Figure 5.42 is illustrated how to calculated from the periodic terrace pattern. Figure 5.42 is the periodic lines that I drew from Figure 5.41 b). From the periodic lines, we can figure out the a_1 and a_2 vectors. Between two vectors, the angle is φ, and the terrace width is the distance d. The length of the a_1 vector is 297.389 nm, the a_2 vector length is 361.117 nm, and the angle φ is 31.4°. From the length of the vector and the angle φ, the terrace width(d) could be calculated, which means that it is the second vector length times sin φ.

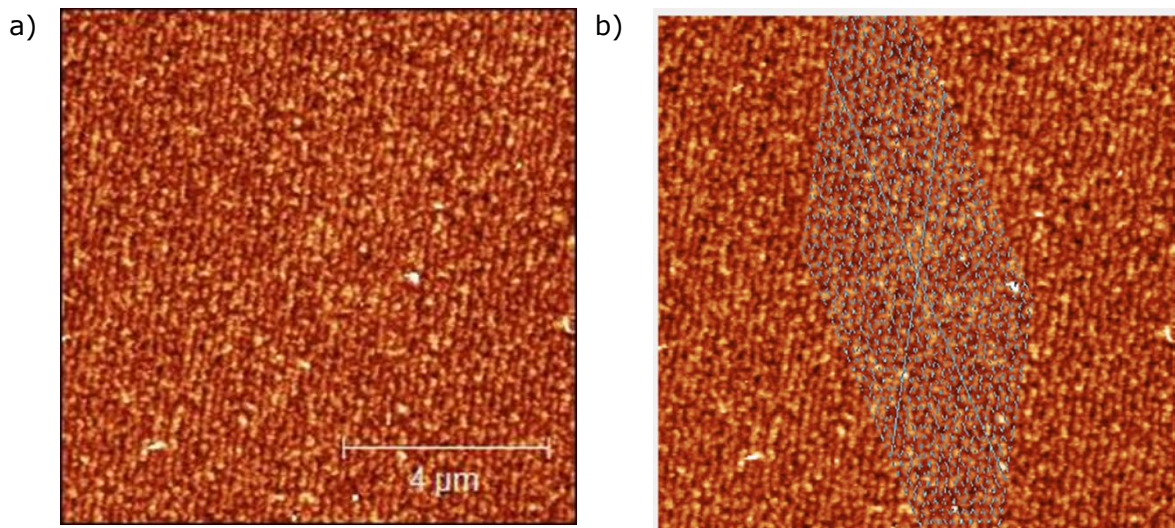Figure 5.41. 10x10 μm^2 of the AFM B5 image on LAO. a) is the location number 1, and b) is the lines on the periodic terrace using the function of 'measure lattice'.
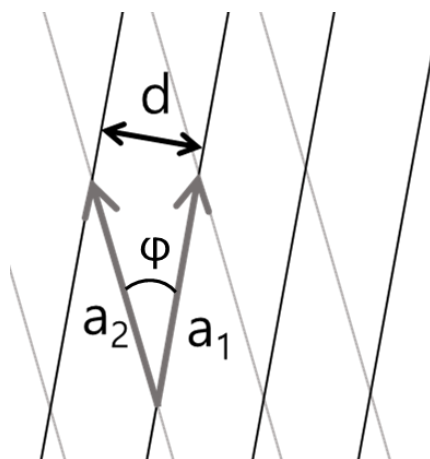

Figure 5.42. The schematic of the lattice lines drawing. We can calculate the terrace width(d) using two vectors and between the angle φ.
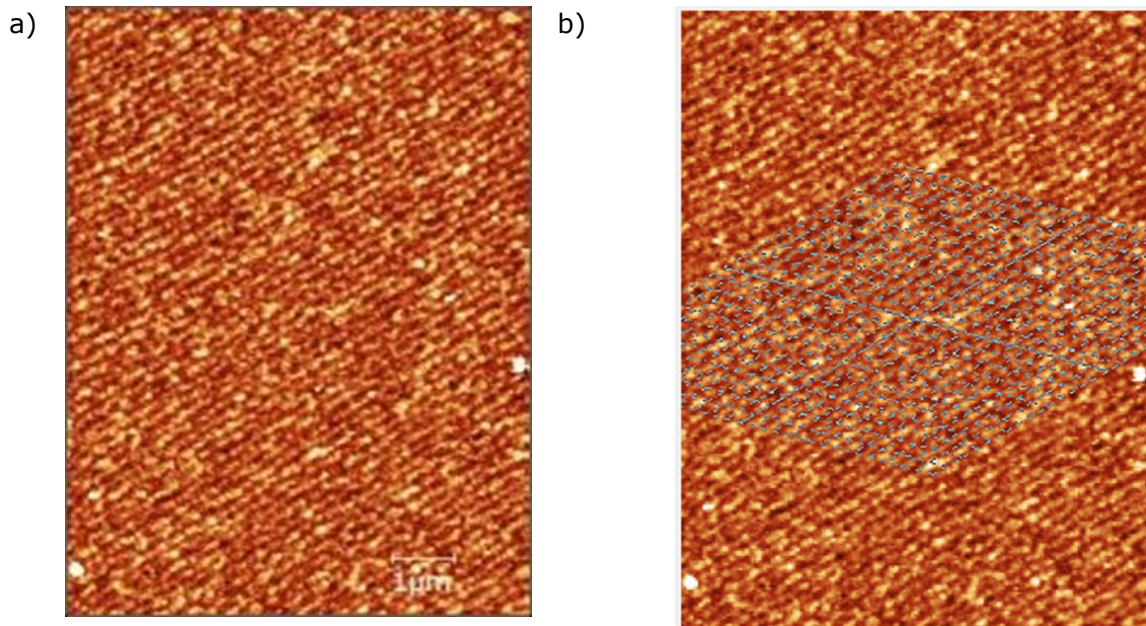
Figure 5.43. 10x10 μm^2 of the AFM B5 image on LAO. a) is the location number 10, and b) is the lines on the periodic terrace using the function of '*measure lattice*'.

When we get terrace width, we can also calculate the apparent miscut angle, according to Bueble[21]. Figure 5.41 is calculated the terrace width at 190±5nm. Figure 5.43 is also 10x10 μm^2 of the AFM B5 image; the location is 10. This location is also estimated the terrace width at 190±5nm. Figure 5.44 describes the cross-section of the LAO before deposition. Using terrace width and lattice constant, we could calculate the apparent miscut angle. If the twin domain wall is perpendicular with terrace width, the surface kink angle could be calculated.
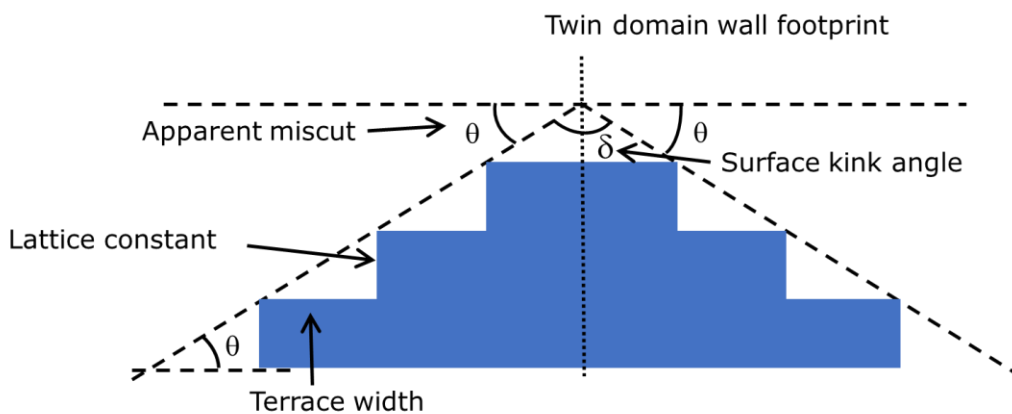
Figure 5.44. Cross-section of the LAO surface before deposition.

Assuming TiO$_2$ is deposited by the c-axis, the TiO$_2$ anatase lattice constant is around twice with the LAO lattice constant. Again, if the twin domain is still perpendicular with deposited TiO$_2$ on LAO, the apparent miscut angle is still identical before and after deposition. Figure 5.45 illustrates the cross-section of TiO$_2$ film on the LAO after deposition.

59
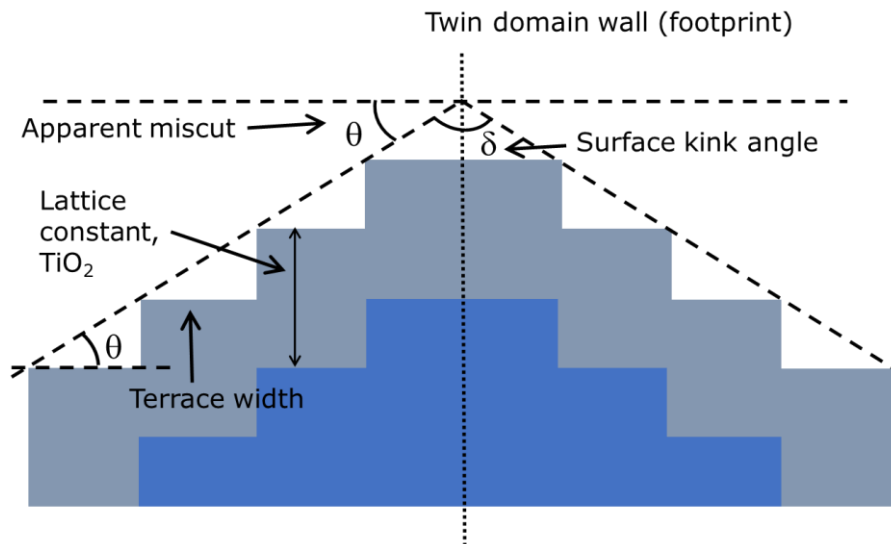
Figure 5.45. Cross-section of TiO$_2$ thin film on the LAO surface during the growth of the TiO$_2$ film on the C-axis.

However, during deposition, the LAO substrate is heated again, and it usually gets new twins. Moreover, it might be cut misorientation; then, the twin domain wall is not perpendicular anymore. After that, the film obtains new apparent miscut angles, new terrace width, and new surface kink angle. Therefore, we cannot see a periodic terrace width. Figure 5.46 illustrates the misorientation twin.
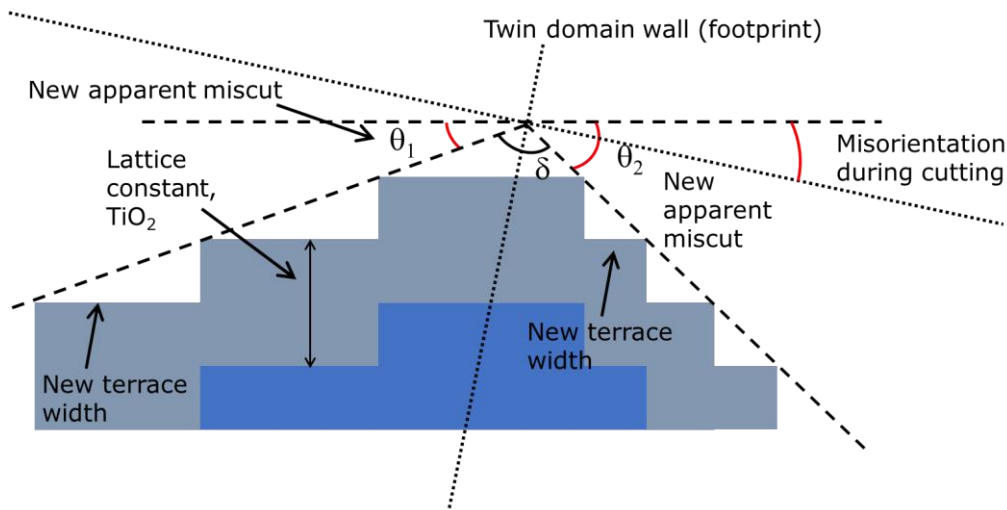
Figure 5.46. Cross-section of the TiO$_2$ on the LAO with misorientation during cutting.

Assuming the twin domain is perpendicular, I can calculate the apparent miscut angle at 0.11757° and the surface kink angle at 179.728°. According to Bueble [21], they got calculated. All these data are pretty similar to Bueble's [21] paper.

Like those methods, I could also calculate B1, although most images are blurry. Figure 5.47 is 10x10 µm^2 of the AFM B1 image. The a$_2$ vector length is 278.094nm, and the angle is 108.05°. Thus the terrace width is around 264.41nm. From this, the miscut angle could get 0.08578°, and the surface kink angle is 179.828°.
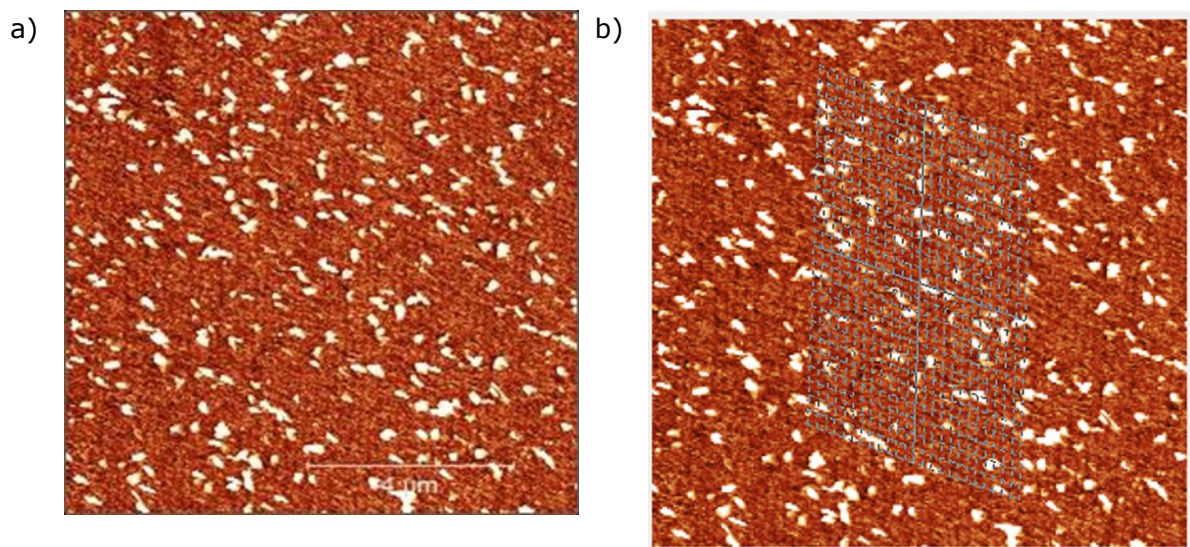
Figure 5.47. 10x10 µm² of the AFM B1 image on LAO. a) is the location number 10, and b) is the lines on the periodic terrace using the function of '*measure lattice*'; the white and the yellow arrows are first and second vectors.

On the other hand, well-ordered regions such as twin or flat areas are stable depositions for both B1 and B5 series. In detail, for B1, the number of hillocks is from 23 to 38; they are moderate in the twin or flat areas. Further, although it is a bit weak, we are able to find the terrace patterns in 2x2 and 10x10 µm² images. Yet, in the mixed regions, the number of hillocks is the highest and the lowest; also, the striped pattern is fainter. For B5, the twin and flat areas have a clear terrace pattern, vertical, horizontal, and diagonal, but the striped pattern in the mixed regions is a bit blurry. I could reconfirm this from the roughness value; I will figure out this in the next chapter.

5.3   Method to determine the hillock properties

As shown earlier, the B1 sample surface consisted of hillocks on top of a smooth surface. I wanted to calculate the surface roughness for the entire surface smooth background with hillocks), but also for the smooth surface alone. To calculate roughness from the AFM images, both including and excluding the hillocks, I thus needed to determine what part of the surface belonged to the hillocks, using the Gwyddion image processing software.

The procedure I developed was as follows (function names in italic), starting from the image processing explained in chapter 4:

1. First, I used "*Stretch color range to part of data.*" I decided on the highest peak n umber, assuming this is the height of the smooth background. Figure 5.48 shows this function.
2. From the previous step, the highest peak number was doubled, and the higher nu mber is the decided mark.
3. I used "*Mark grains by threshold*." marking the hillocks threshold at the double he ight, which I found from step two. Figure 5.49 a) is hillocks drawn in red using th e function.
4. Except for the marked area, I was able to get the roughness. Figure 5.49 b) is th

e area without hillocks. The roughness data is received from the function "*Statical quantities*." I could find the three masking modes; first, the 'Exclude masked region' mode is determined by the RMS and average roughness of the excluding masked area. Second 'Include only masked region' determined the volume of hillocks; last, 'Use entire image (ignore mask)' to select the RMS and average roughness of the entire area.
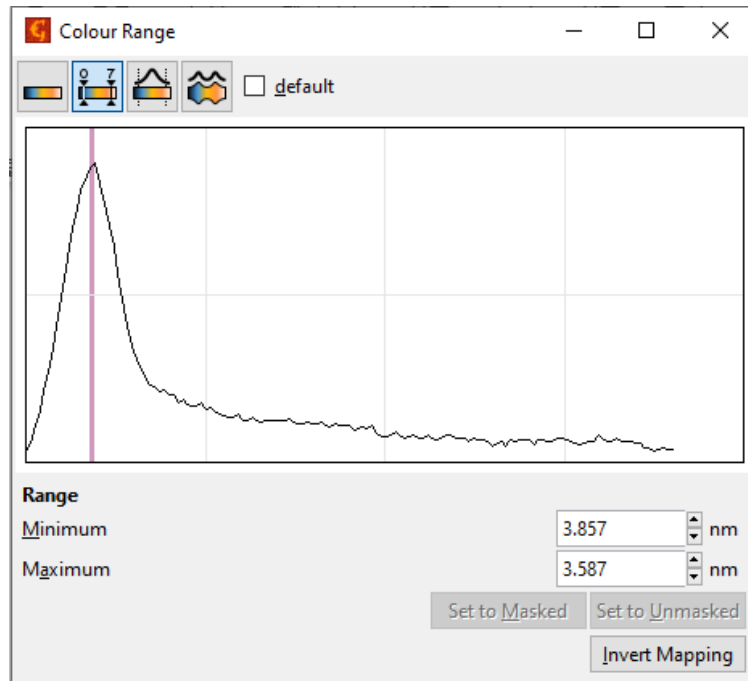

Figure 5.48. The scale of color range. To find the highest peak for marking the hillocks

Meanwhile, for the 2x2 µm² AFM image, I have described a line profile in Figure 5.50. In Figure a), the line across the hillocks is the line profile on the B1 AFM image. Based on the line across the hillocks, I plotted a graph(Figure b)). The height of hillocks is between 10nm and 30nm. The last image is the 3D image of the AFM for 2x2 µm².

On the other hand, although B5 does not have hillocks, I used the marking function similar to B1 to mark the terrace except for excessively high ones.

To compare the B1 and B5 AFM images, I also chose a B5 for 2x2 µm² image to draw the line profile. Figure 5.48 is illustrated in the same method as Figure 5.51. The B1 image has hillocks, while the B5 has terraces. The step height is roughly from 3nm to 20nm.
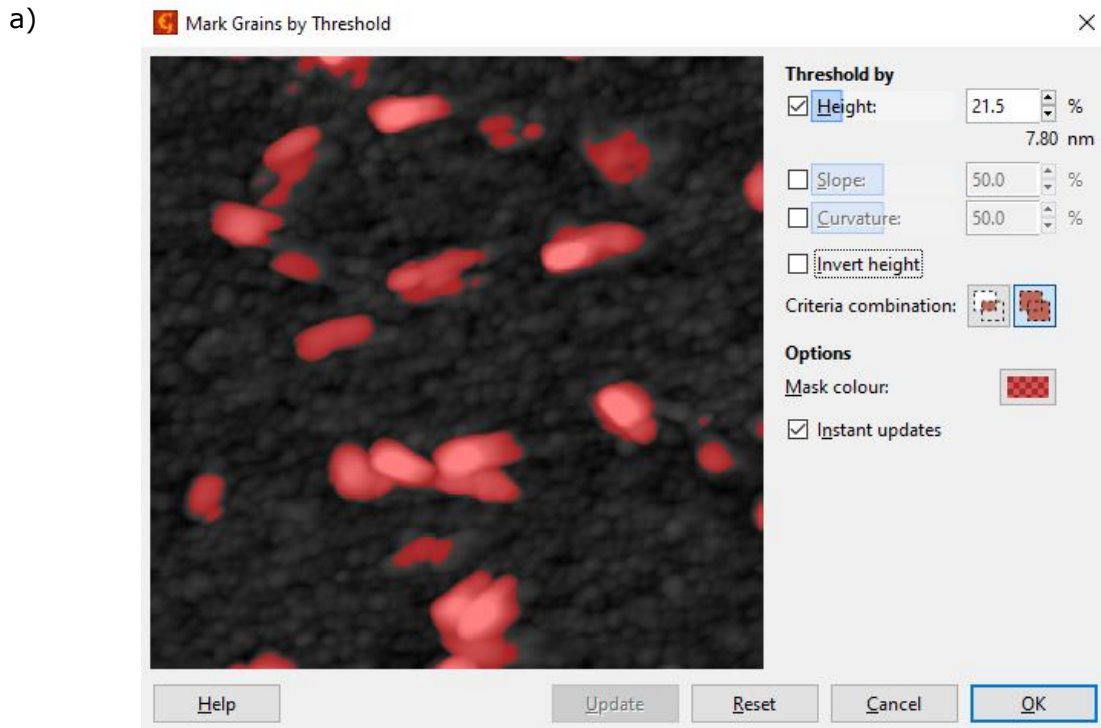
a)

b)
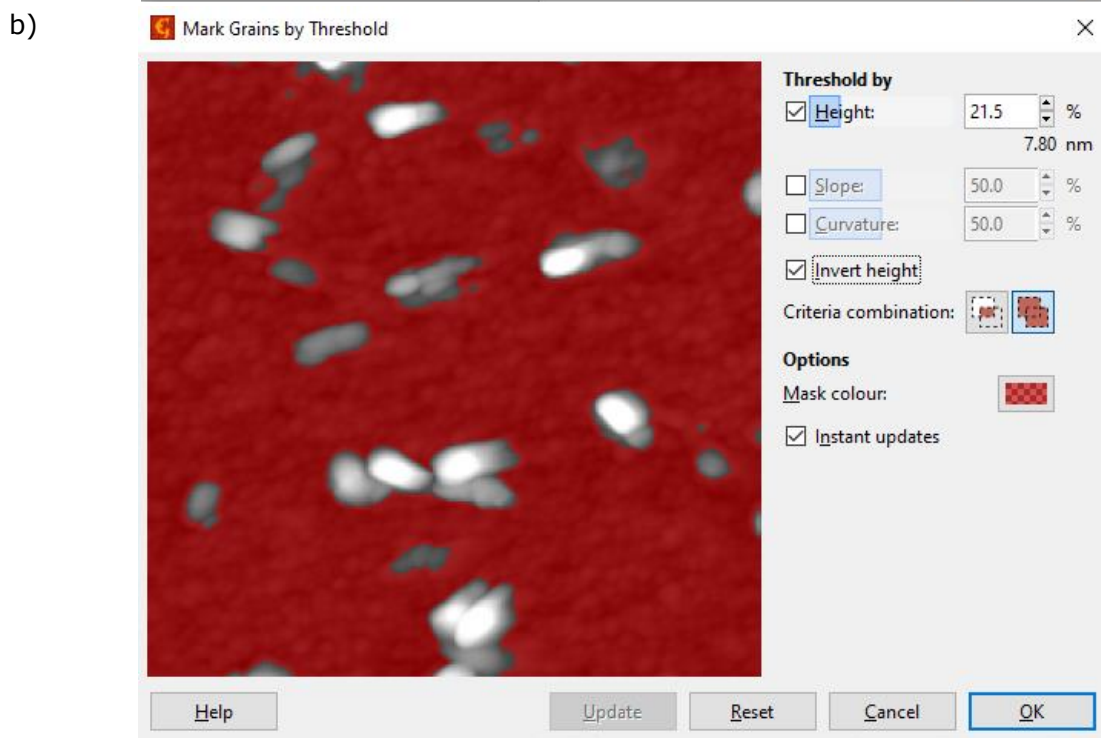
Figure 5.49. a) is the marking of the hillocks. b) is the area of the calculation roughness
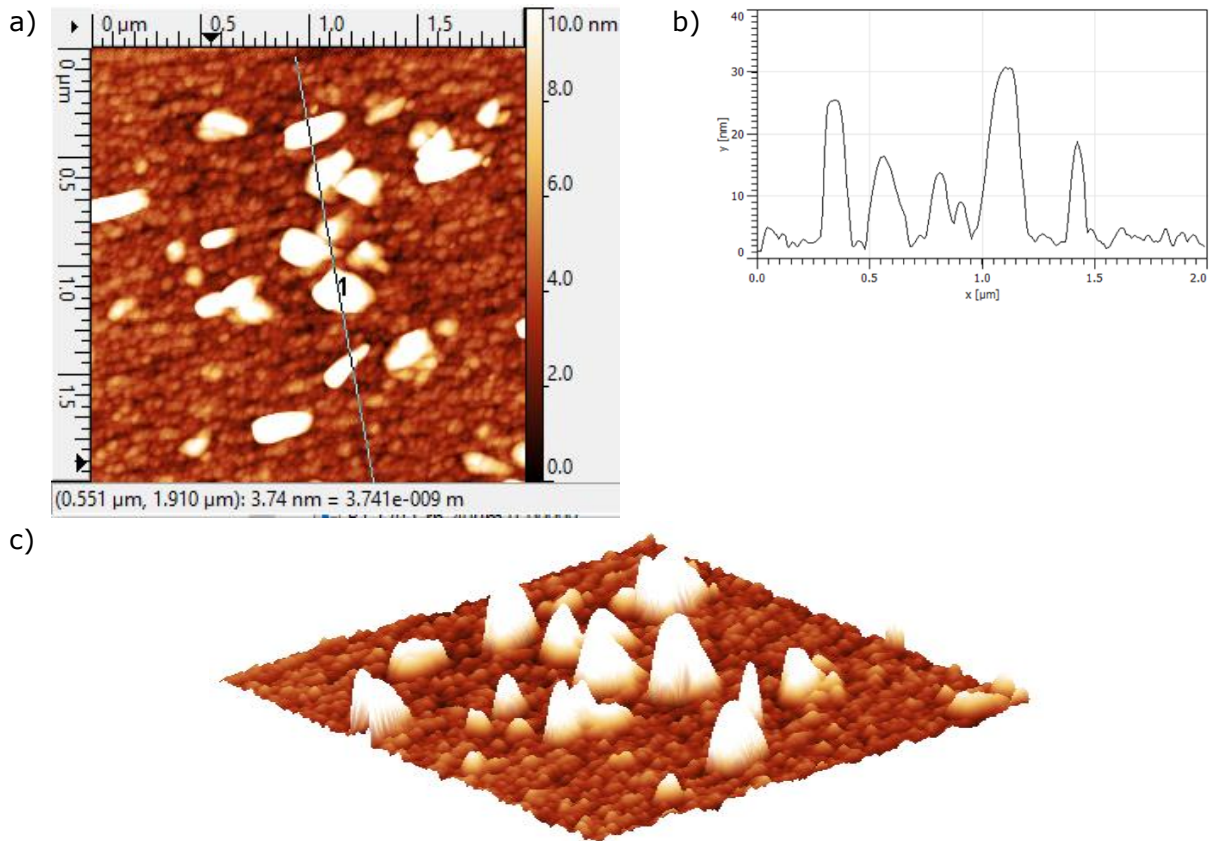
Figure 5.50. a) B1 on LAO Right high corner for2x2µm^2 line profile image across the hillocks. b) the line profile graph c) The 3D image of AFM
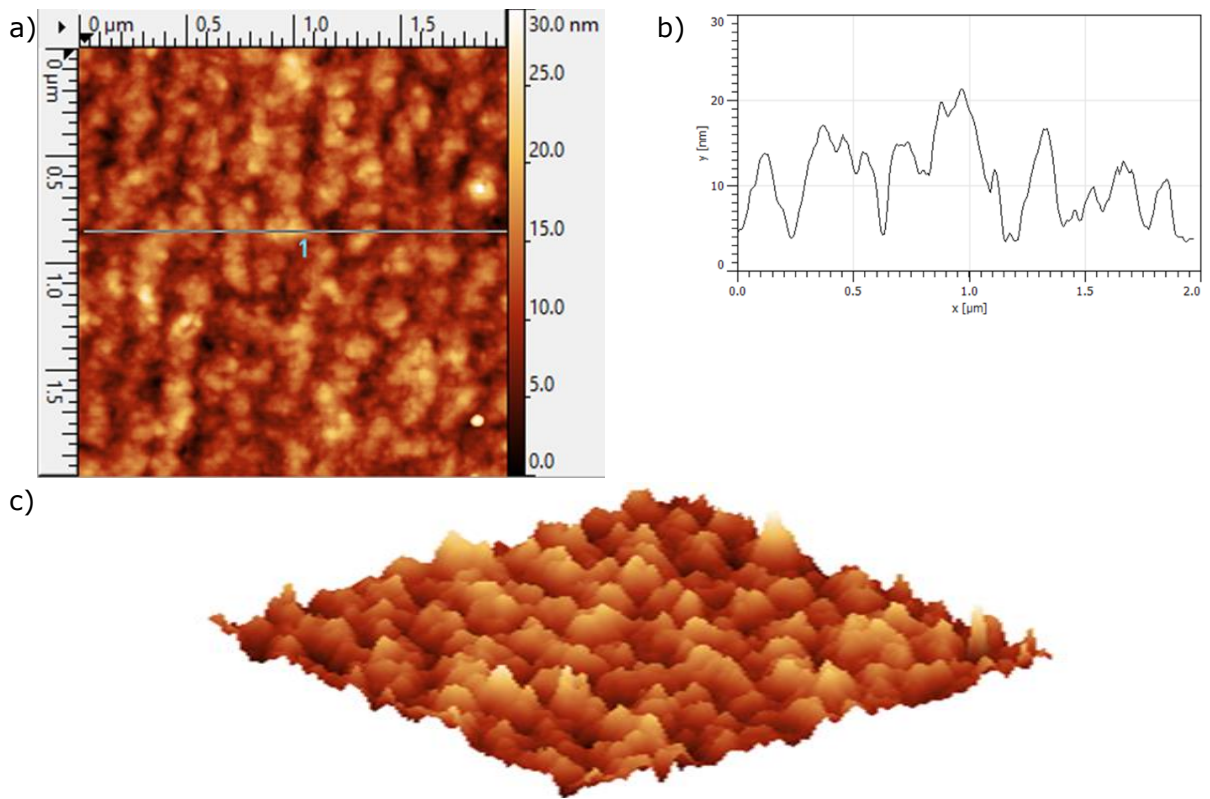

Figure 5.51. a) B5on LAO Right high corner for2x2 µm^2 line profile image across the hillocks. b) the line profile graph c) The 3D image of AFM

5.4   Roughness obtained from AFM images for B1 and B5 on LAO

This section will explain the roughness with the relationship between the volume of hillocks and hillock density. Also, the roughness is illustrated depending on the areas such as twin, mixed, and flat.

To easily understand, I plotted a graph where the x-axis is the volume of hillocks and the y-axis is the roughness. The red triangles with trend lines are for the roughness of the whole area, and the green dots with trend lines are for the roughness except for the volume of hillocks. Rq is the RMS roughness, and Ra is the average roughness (Ch.5.3). I extracted the roughness data from the AFM images. Further, the relation between the roughness and hillock density is also described. The extracting method is explained in detail in chapter 4.

5.4.1 The roughness of sample B1

First, I plotted the roughness with the volume of hillocks. As we can see, the green circles with a trend line are the entire region (i.e., including hillocks). The roughness for excluded hillocks is the red triangles with a red trendline. I plotted the roughness of the hillock volume with only excluded hillock area since I wanted to use the background area. Furthermore, to understand the relation between the roughness and the hillock density, I also plotted the roughness with hillock density depending on three regions. Also, to quickly compare the roughness of different areas, I have attached the region images depending on the three areas from the lowest to the highest roughness.

Results 2x2 µm² images

For 2x2 µm2 images, the roughness is raised by using the whole area and by increasing the volume of hillocks in Figure 5.52. The roughness is between 2 and 5nm for RMS, and the average values are from 1 to 3nm. Excluding hillock areas, the roughness stayed on the horizontal trend line, except for one region. Figure 5.53 is the roughness with hillock density, and it also has the excluded hillock region's roughness which is similar in all the spots. However, the entire area does not seem to have any trends.

Thus, I decided to zoom in on the y-axis in Figure 5.54 using only the excluded hillock region. In Figure 5.54, 3D Optical Profiler and AFM images are attached with the location number. Even though the roughness interval is only at 0.7nm, the roughness also increases with the growing hillock volume in general.

Figure 5.55 shows the roughness with hillock density depending on three regions: twin, flat, and mixed with location number. I plotted only the RMS roughness with hillock density. The open mark is the roughness of the excluded hillock area, and the closed sign is the roughness of the entire region. In the excluded hillock region, RMS roughness is similar in the entire region which is around 1nm. From the closed mark, we can figure out the roughness between 3 and less than 5nm, and the density of the mixed area is pretty varied.

To see the region, I have arranged the 3D Optical Profiler and AFM images from low roughness to high roughness depending on the regions: twin, mixed and flat. The low location number means more twins, and the high location number is flatter. Location number 4 could not be taken because of a measurement error.
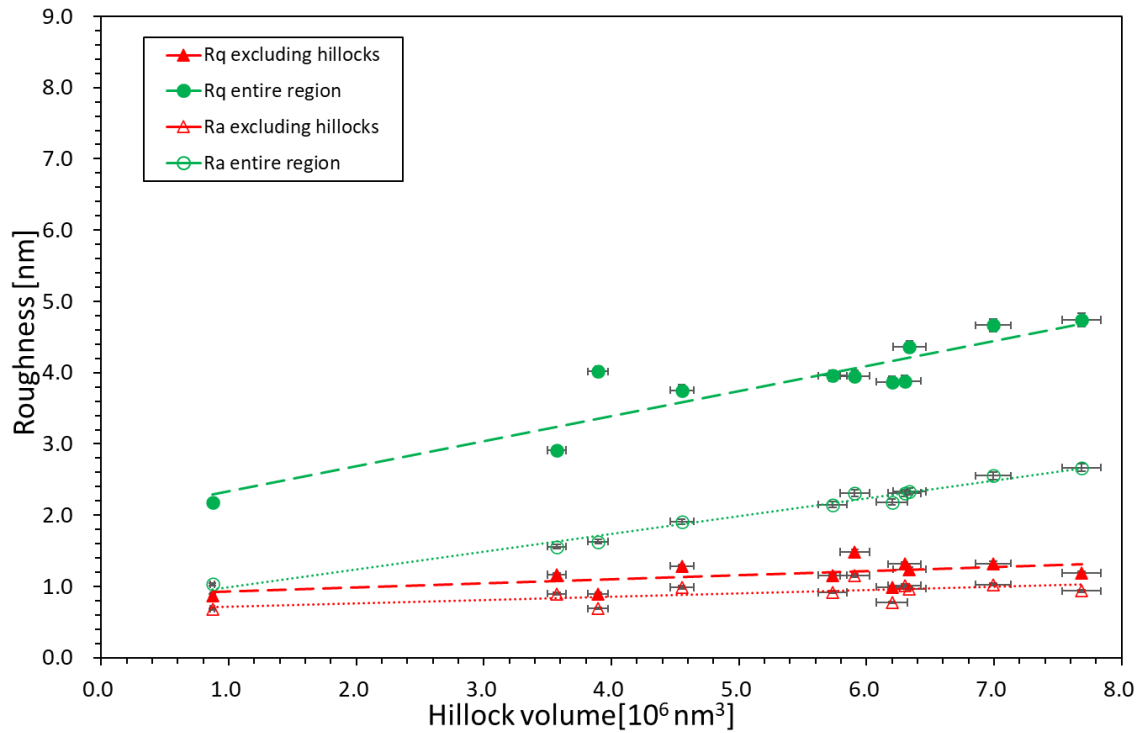
Figure 5.52. RMS and average roughness – the volume of hillocks graph. The red triangles are excluded hillocks volume with roughness, and the green dots are included hillocks volume with roughness(for the entire area) for 2x2 μm^2 images of the B1.
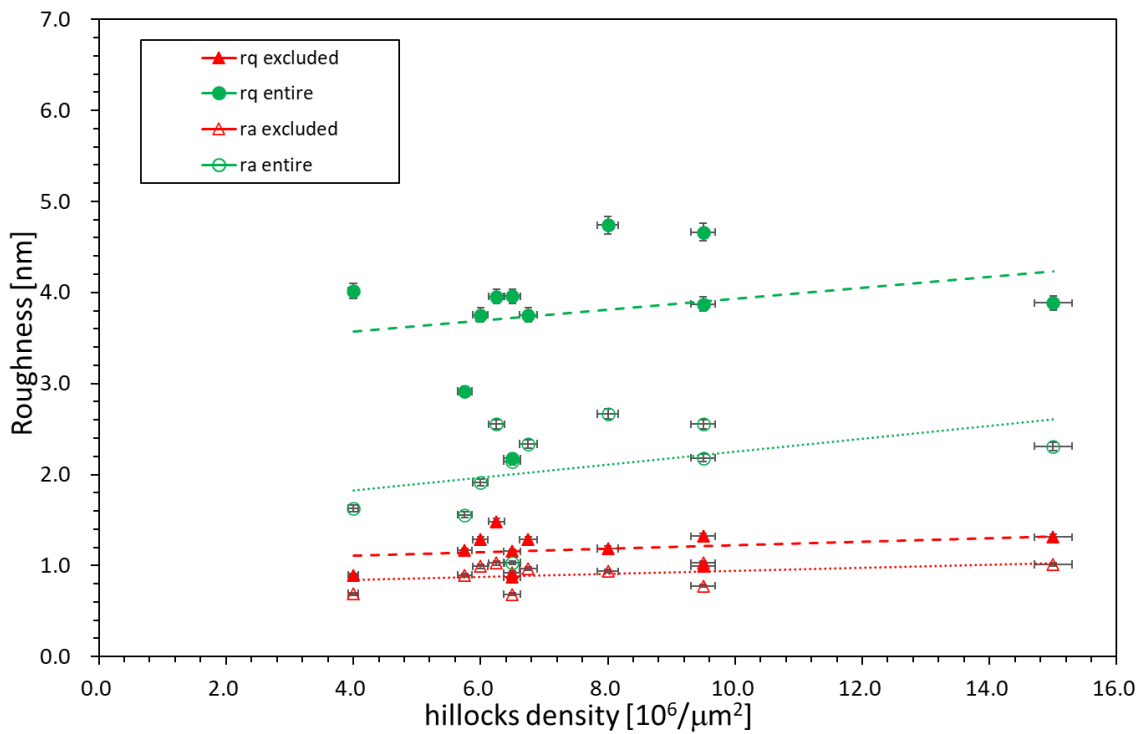

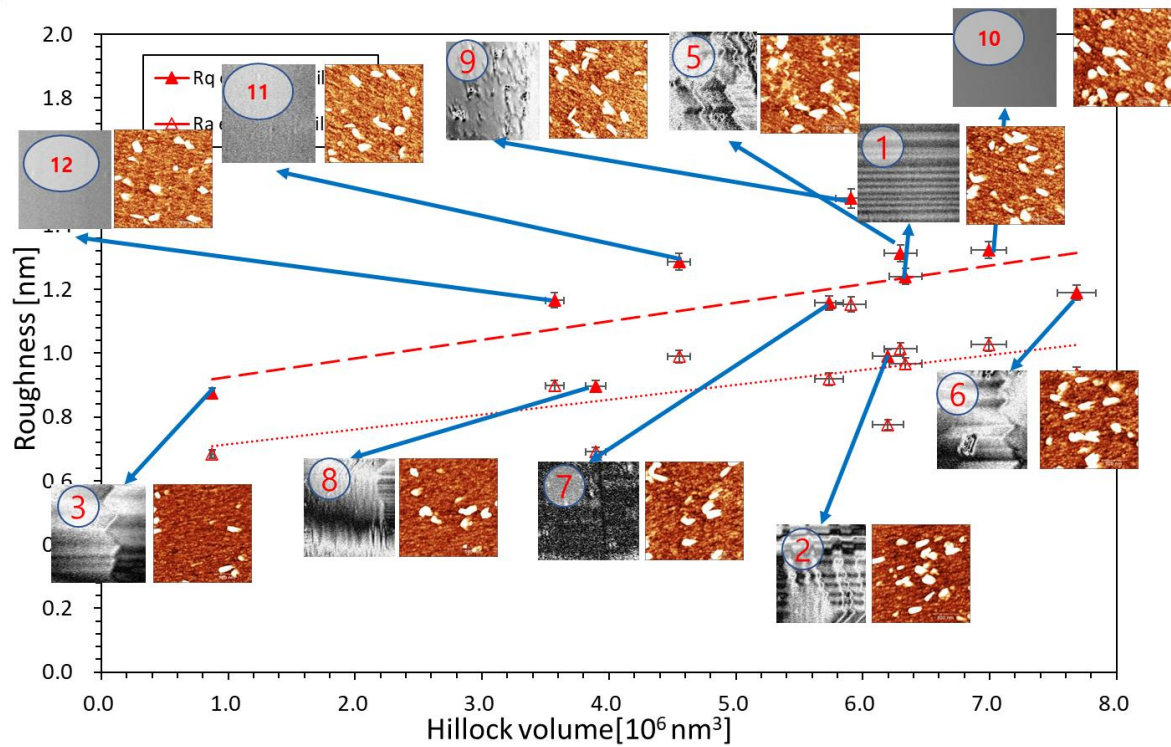Figure 5.53. The roughness with hillock density for 2x2 μm^2 images of B1.

Figure 5.54. RMS and average roughness – the volume of hillocks graph with AFM and 3D Optical Profiler images for excluded hillock area for 2x2 μm2 images of the B1. Not to confuse, the images pointed at are only by RMS roughness. The volume of the hillock is identical in RMS and average roughness. Location number 4 could not be taken because of a measurement error.
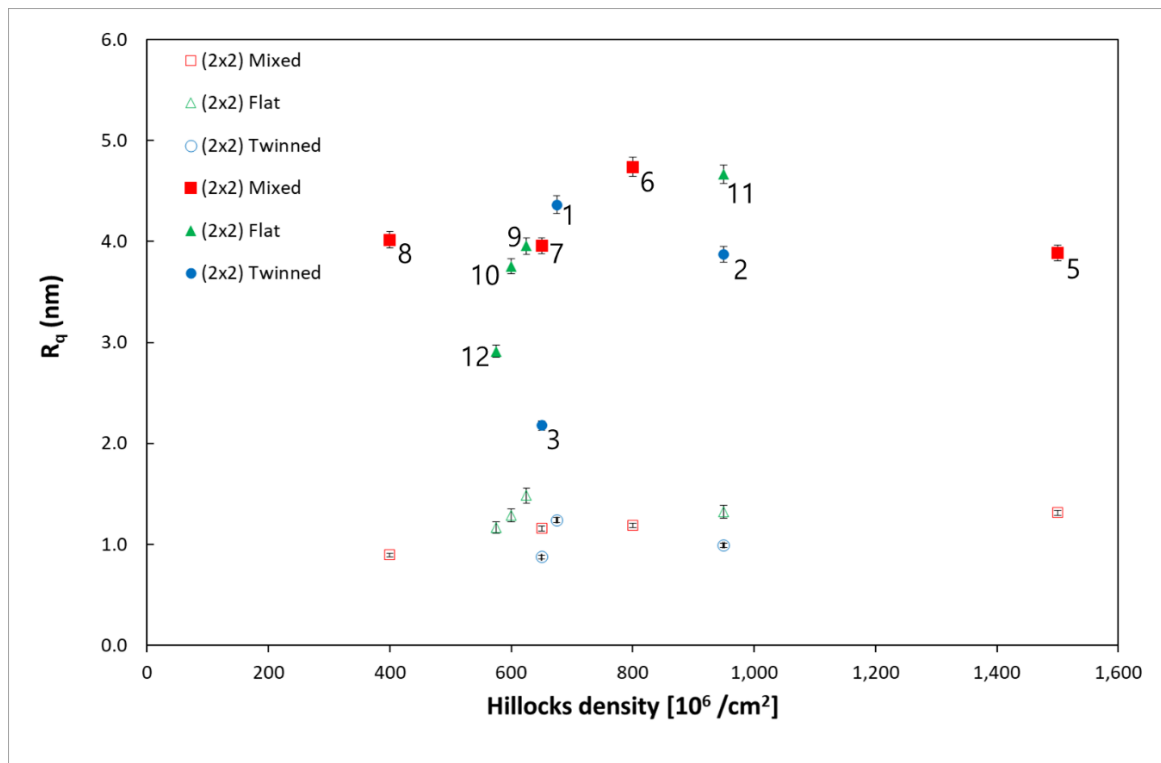
Figure 5.55. The RMS roughness graph with the hillock density for 2x2 μm2 of the AFM image B1 of the three regions with location number.
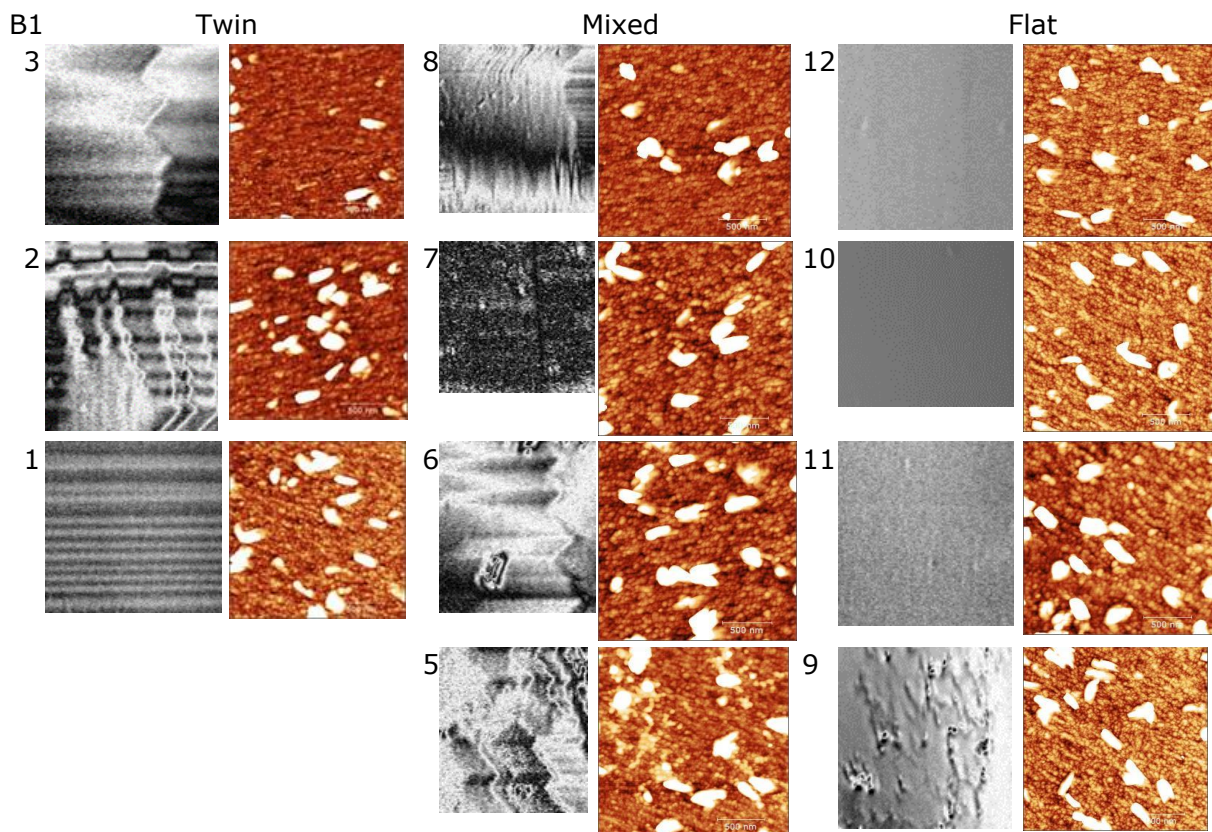
Figure 5.56. The three regions, from low roughness in the upper row to high roughness at the bottom, with location numbers of 2x2 µm2 for B1.

Discussion

In Figure 5.54, I could figure out that the roughness is not significantly affected among twin, flat, and mixed areas; yet, the roughness is the smallest or the most considerable value in mixed areas. Moreover, the flat and twin areas closely follow the trend line, while the mixed region is pretty random.

According to Figure 5.55, the hillock affected the RMS roughness, so the RMS roughness is much bigger than the excluded hillock region. However, depending on the areas, they cannot influence the roughness; the value is similar in all the spots except location 3. I believe location 3 does not have enough hillocks, so the roughness is pretty minor. On the other hand, the noticeable feature is that the mixed area of hillock density is quite spread out.

However, measurement areas are only twelve, so it is tough to say whether they are affected or not. There is also no trend in the areas since the RMS average roughness is twin area at 1.24nm, the mixed region at 1.13nm, and the flat area at 1.26nm, respectively. The value does not have a significant difference, like the number of hillocks per area trend. I think if I had measured more spots, we would have got the tendency. I think it is tough to come to conclusions on the measurement of the twelve areas.

Results 10x10 μm² images

Let us move to 10x10 μm2 roughness. Similar to 2x2 μm2 images, when the volume of hillocks increases, the roughness also grows; the value is from 3nm to 5.5nm for RMS and 1-2.5nm for average roughness in Figure 5.57. The excluded hillock area is also similar to 2x2 μm2 roughness; in general, the roughness is less than 1nm in the horizontal trend line.

In Figure 5.58, we are able to see the roughness value with hillock density. Although I drew the trend line, the entire region seems to have no trend; yet, the excluded hillock area has a similar tendency with 2x2 μm2 roughness- the horizontal trend line. However, compared to 2x2 μm2 roughness, it is pretty random.

In the excluded hillock area, the roughness rises by increasing hillock volume in Figure 5.59. However, as you can see from the 3D Optical Profiler and AFM images, the region cannot affect the roughness. For location number 2, the roughness is calculated only inside the black dash line since the entire area is not flat.

Increasing hillocks density, the RMS roughness also grows for twin and flat areas in Figure 5.60; yet, the mixed area trend is opposite in the entire regions. However, in the excluded area RMS roughness is all similar, around 1nm.

Figure 5.61 shows the 3D Optical Profiler and AFM image of the three regions from low roughness to high roughness using excluded hillock area. Yet, I could not find any trends.
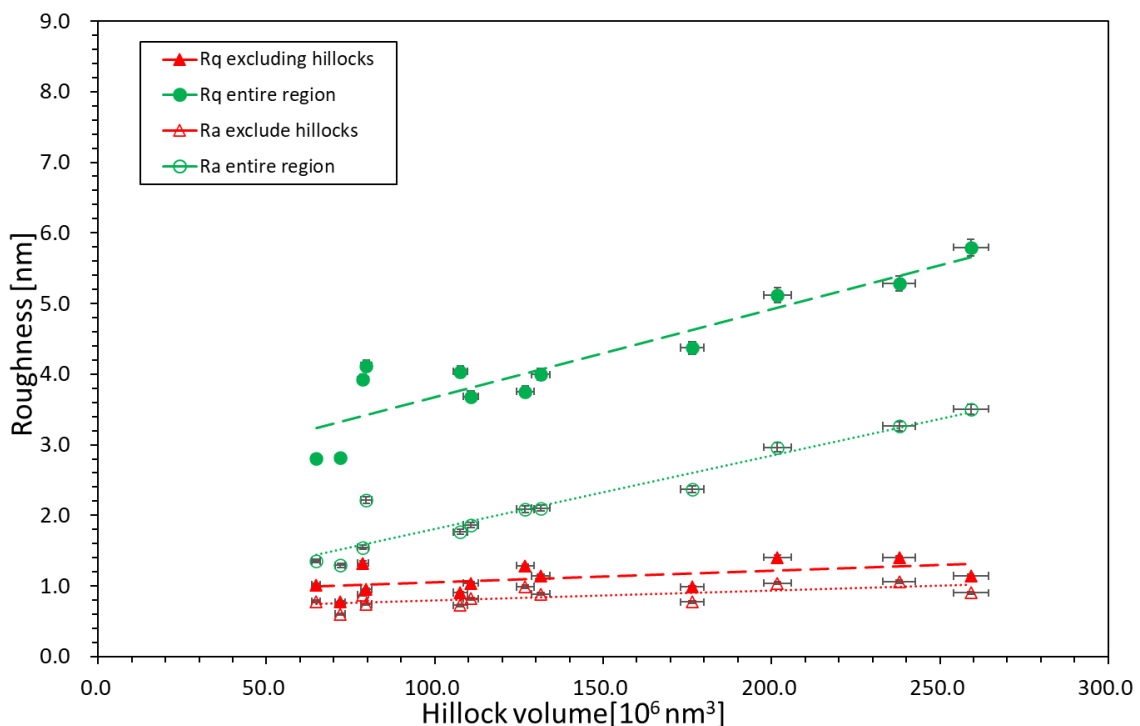

Figure 5.57. RMS and average roughness – the volume of hillocks graph. The red triangles are excluded hillocks volume with roughness, and the green dots are included hillocks volume with roughness(for the entire area) for 10x10 μm² images of the B1.
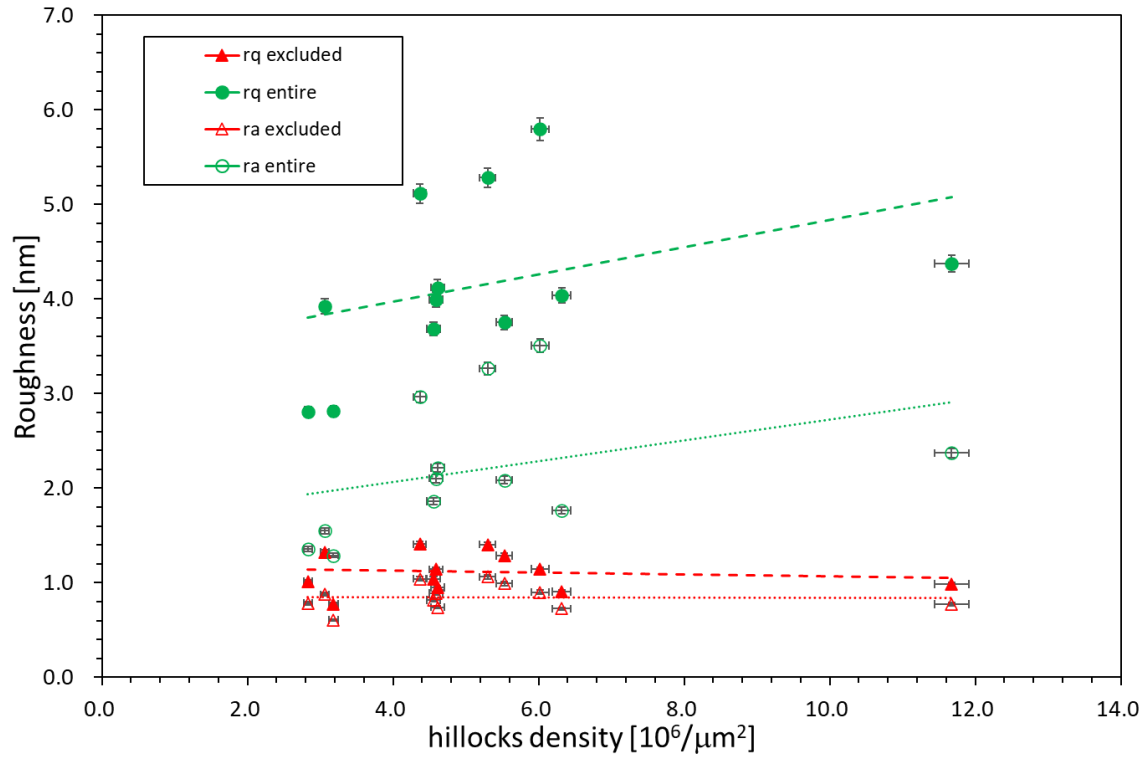
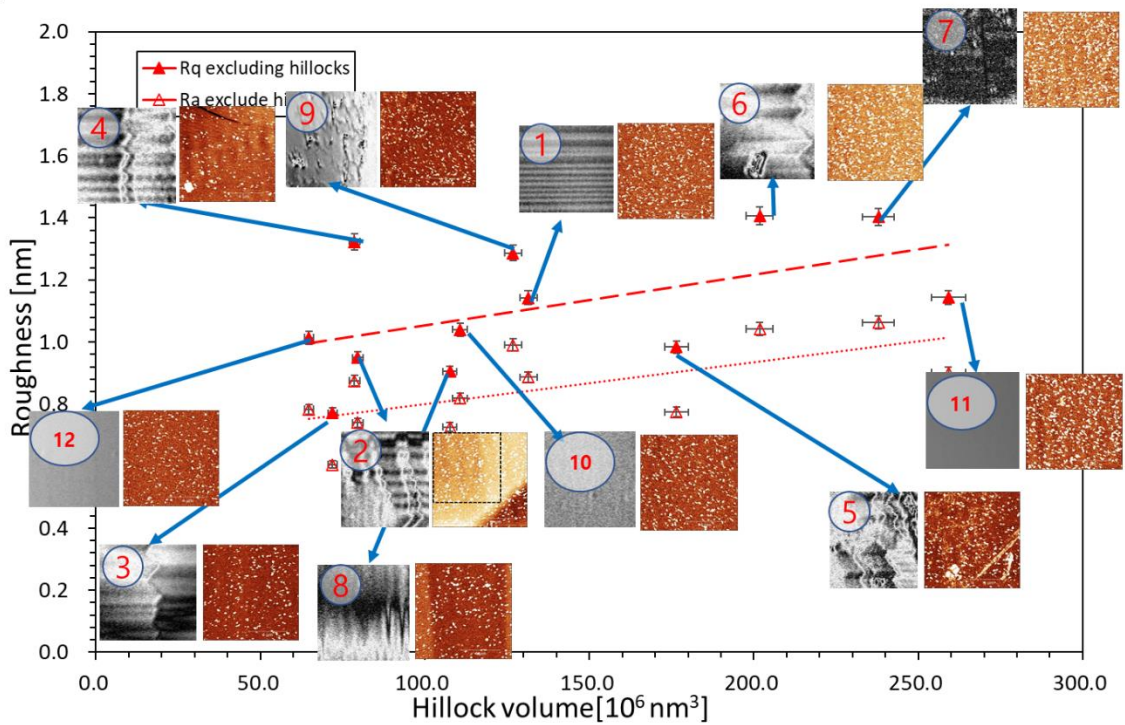Figure 5.58. The roughness with hillock density for 10x10 µm^2 images of B1.

Figure 5.59. RMS and average roughness – the volume of hillocks graph with AFM and 3D Optical Profiler images for excluded hillock area for 10x10 µm2 images of the B1. Not to confuse, the images pointed at are only by RMS roughness. The volume of the hillock is identical in both RMS and average roughness.
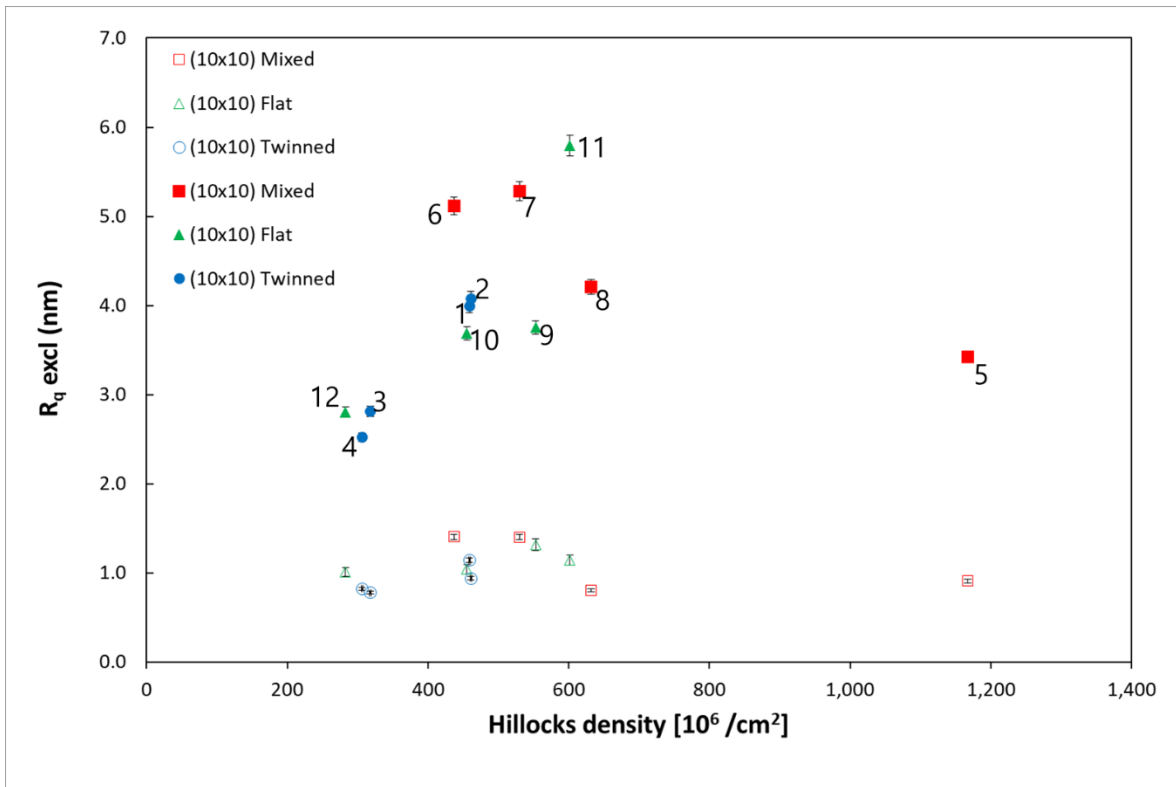
Figure. 5.60. The RMS roughness graph with the hillocks density for 10x10 μm² of the B1 by the three regions with location number.
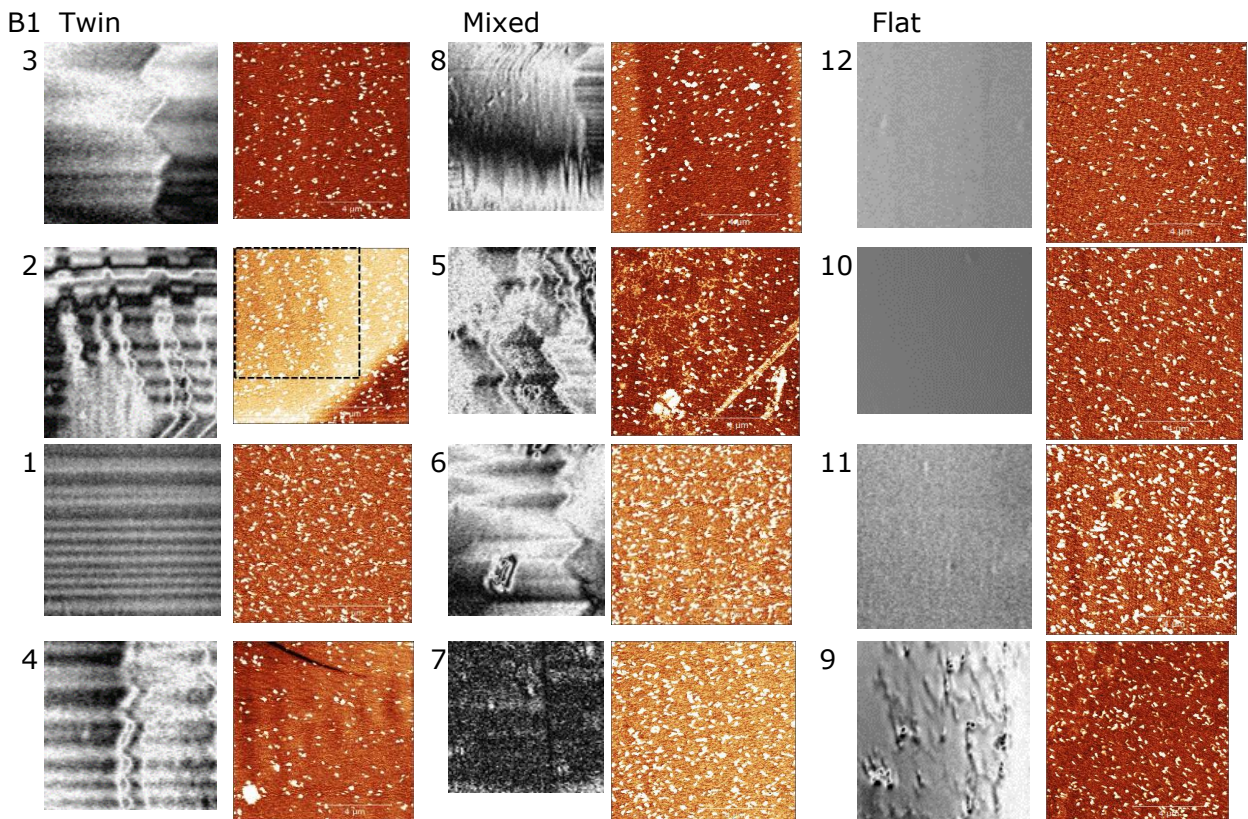
Figure 5.61. The three regions, from low roughness in the top row to high roughness in the bottom row, excluded the hillock areas with location numbers of 10x10 μm² for B1.

Discussion

Like the 2x2 µm2 image, the roughness is not affected by the twin, mixed, or flat regions. With the increasing volume of hillocks, the roughness is generally intensified. Although I zoomed in the y-axis (roughness) in Figure 5.59, there is no trend. It seems that as the roughness grows, there is an increase in the hillock volume; in fact, there is no big difference in the gap, roughly 0.5nm. Since I measured only twelve different regions, it is hard to say there is a clear trend.

Results 20x20 µm² to 80x80 µm² images

Since it is hard to find the roughness tendency in the three regions, the hillock density or the hillock volume, I would like to explain the roughness from 20x20 to 80x80 µm2 image together in this section. Figures 5.62 to 5.64 are for the roughness with hillock volume, the roughness only in excluded hillock area by hillock volume, and the roughness in the images with a location number, in 20x20 µm2 images respectively. I used the roughness only inside the white dash lines because they are not flat due to the twin or contaminations. In the identical method, 40x40 µm2 image roughness is illustrated in Figures 5.65-67, and 80x80 µm2 image is in Figures 5.68-70. In the hillock volume graph, the roughness increases the hillock volume, and the roughness also generally grows. However, the roughness of 80x80 µm2 images does not follow the tendency, and they are relatively random. Like 10x10 µm2 images, I used the roughness inside of the white dash line, which has a similar reason to 10x10 µm2 images.
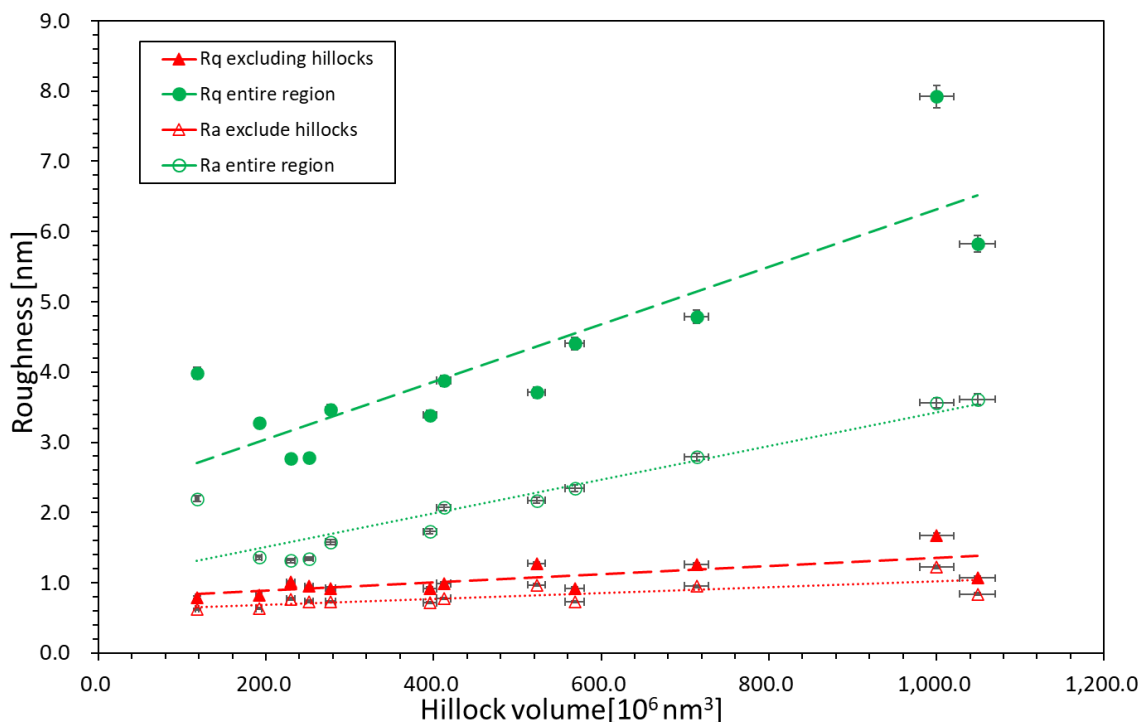

Figure 5.62. RMS and average roughness – the volume of hillocks graph. The red triangles are excluded hillocks volume with roughness, and the green dots are included hillocks volume with roughness(for the entire area) for 20x20 µm² images of the B1.
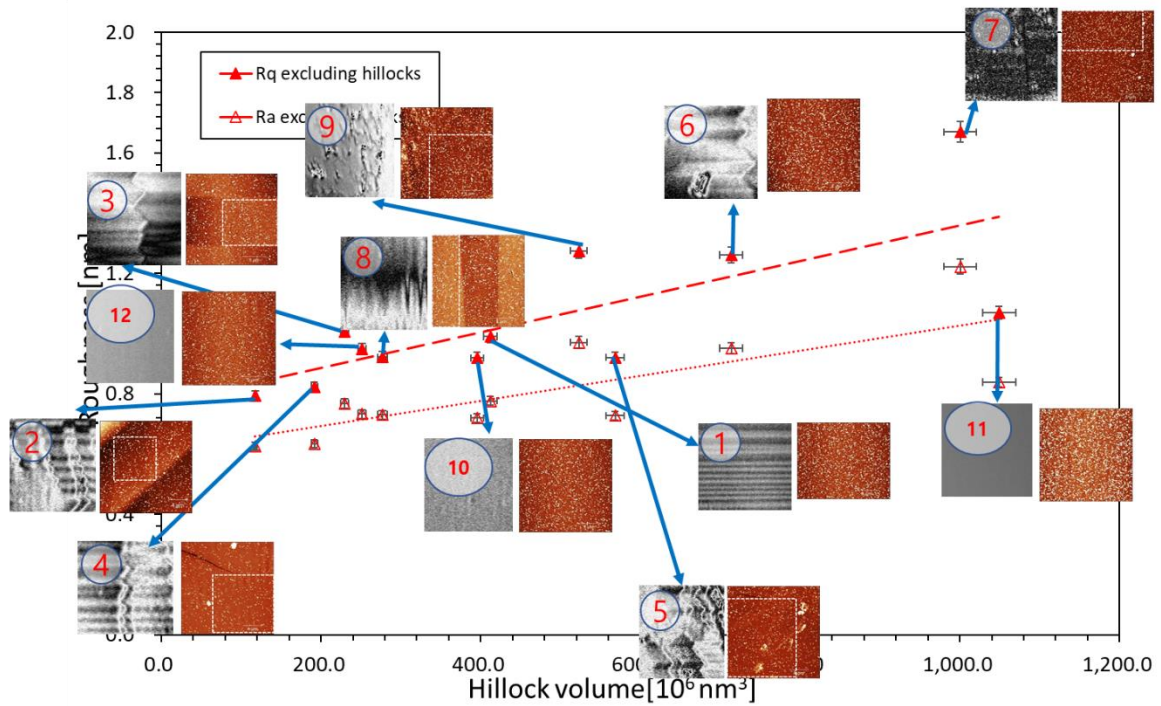
Figure 5.63. RMS and average roughness – the volume of hillocks graph with AFM and 3D Optical Profiler images for excluded hillock area for 20x20 µm² images of the B1.
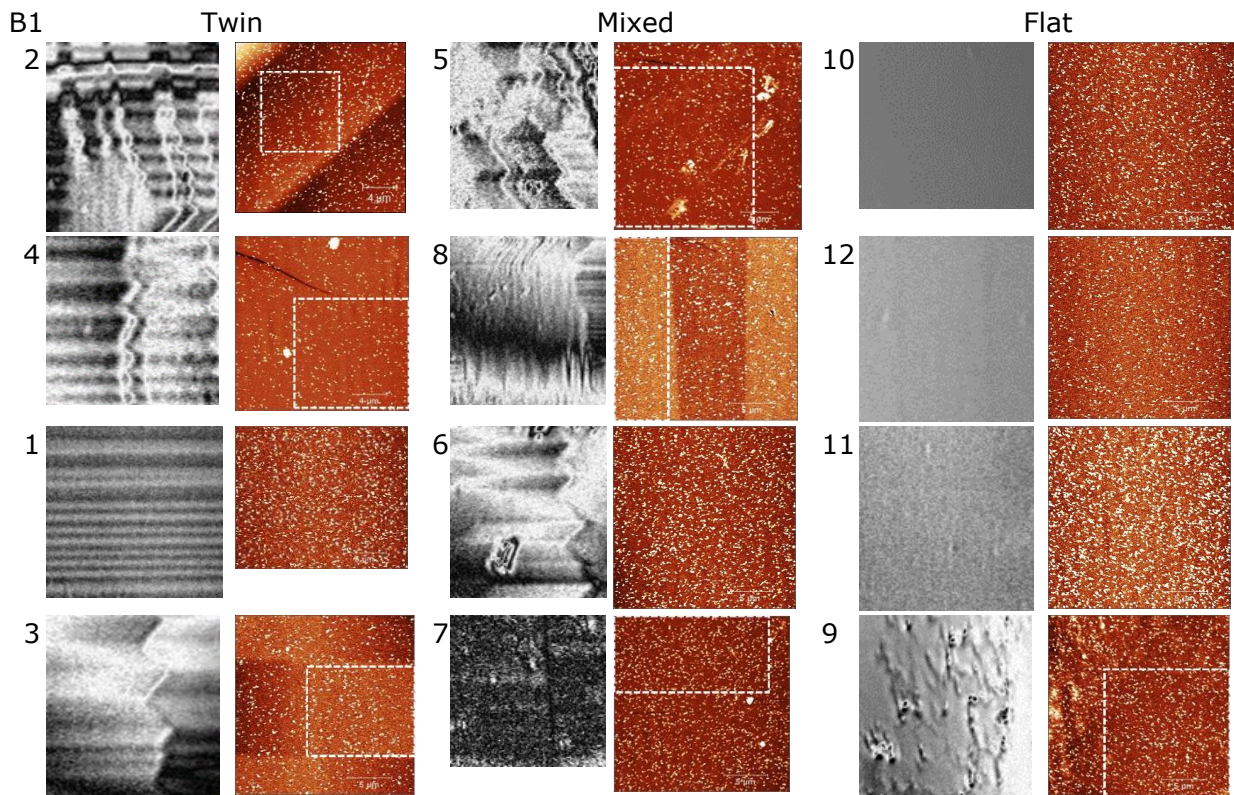

Figure 5.64. The three regions, from low roughness in the top row to high roughness in the bottom row, excluded the hillock areas with location numbers of 20x20 µm² for B1.
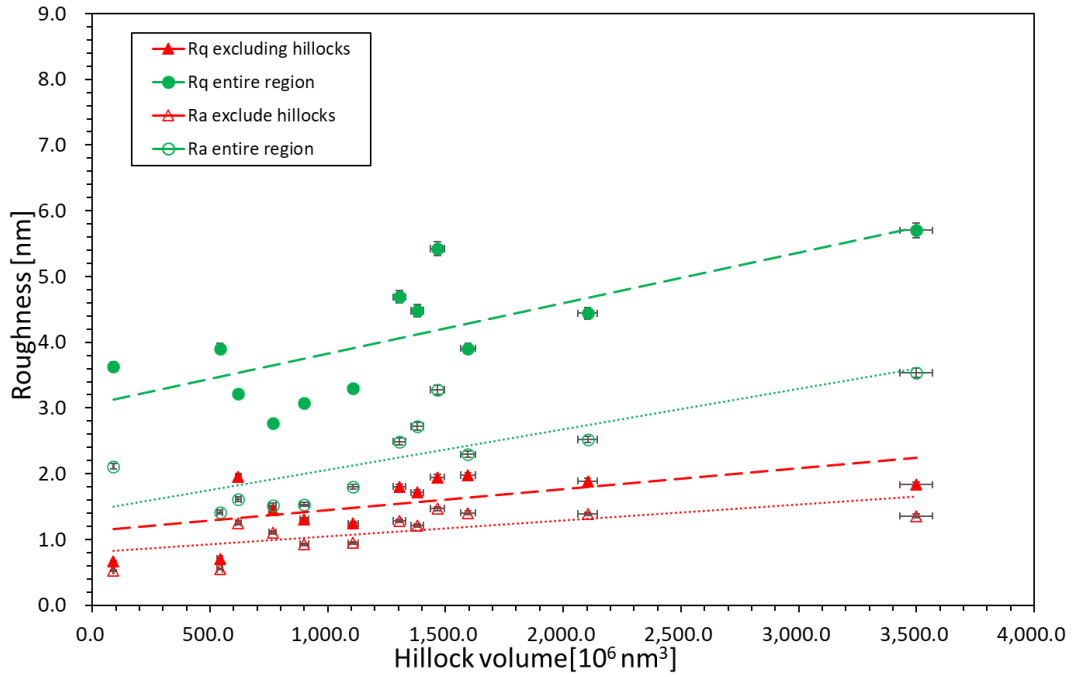
Figure 5.65. RMS and average roughness – the volume of hillocks graph. The red triangles are excluded hillocks volume with roughness, and the green dots are included hillocks volume with roughness(for the entire area) for 40x40 μm² images of the B1.
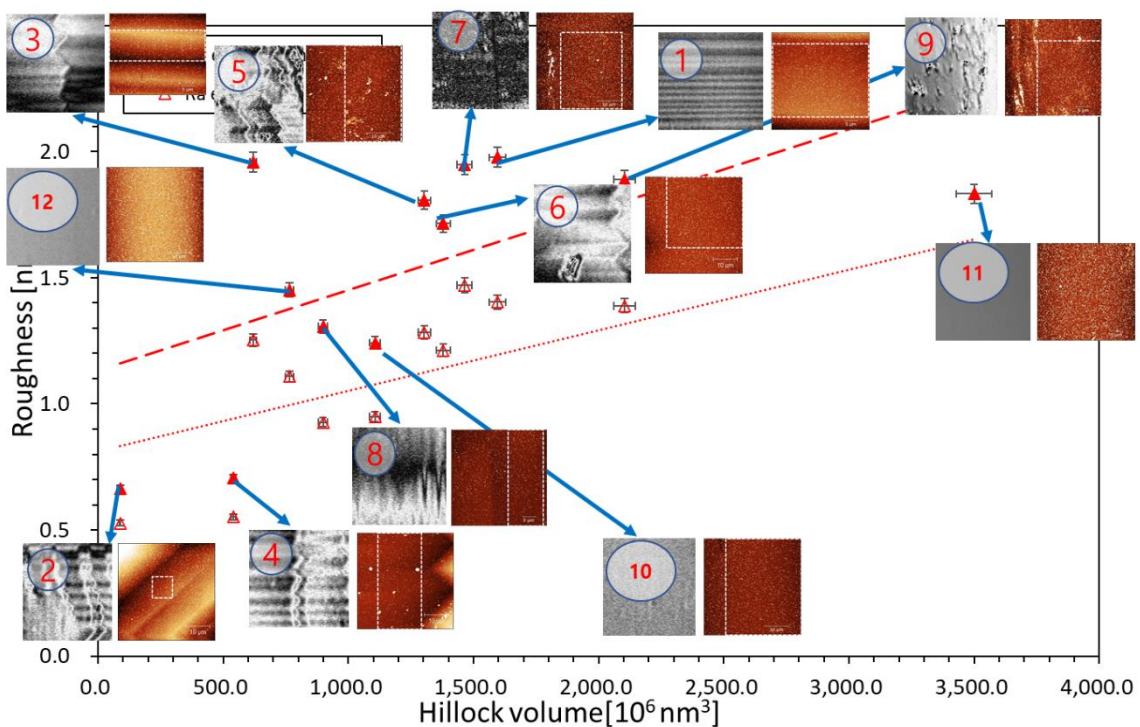

Figure 5.66. RMS and average roughness – the volume of hillocks graph with AFM and 3D Optical Profiler images for excluded hillock area for 40x40 μm² images of the B1.
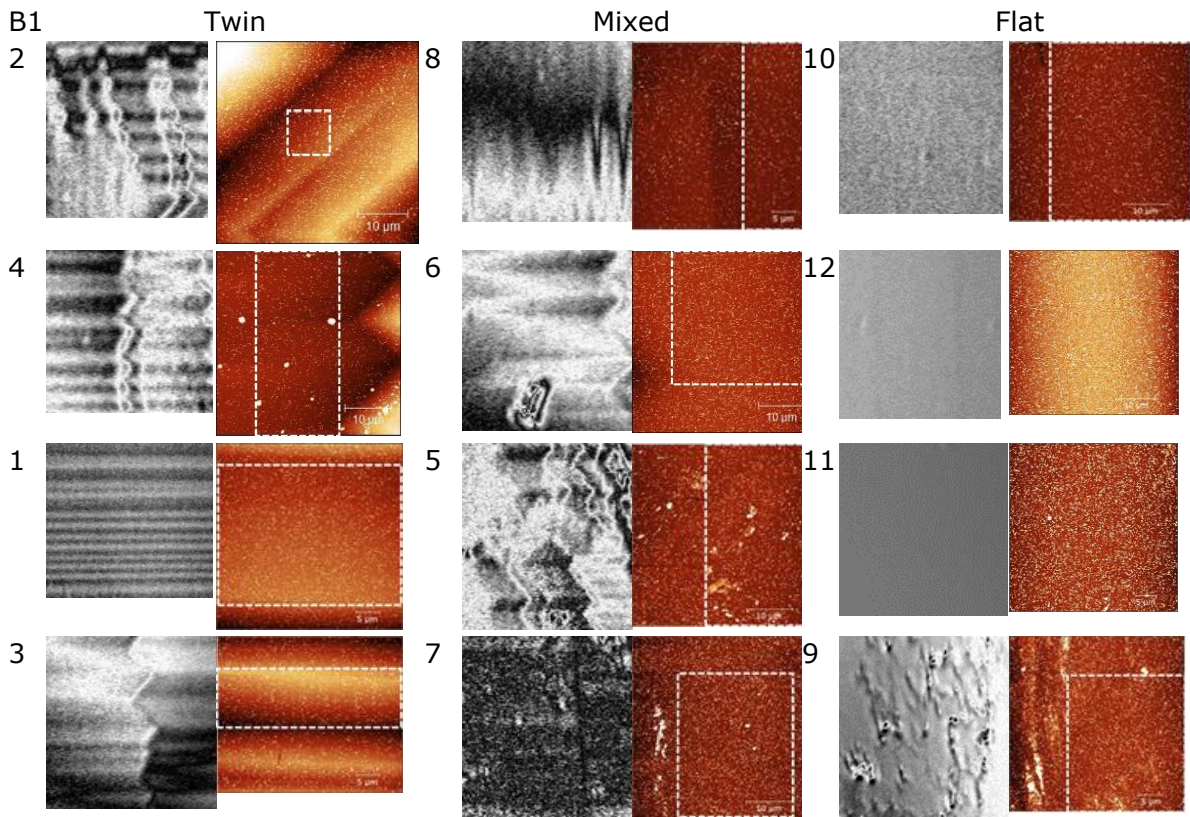
Figure 5.67. The three regions, from low roughness in the top row to high roughness in the bottom row, excluded the hillock areas with location numbers of 40x40 μm² for B1.
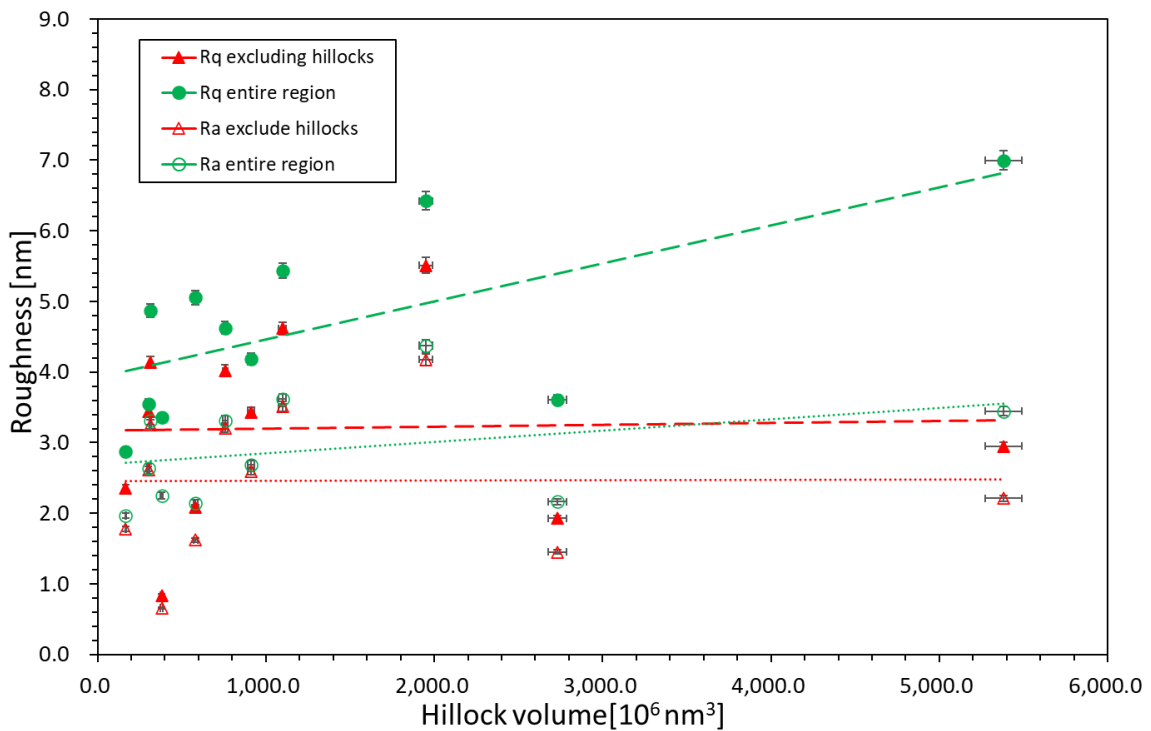

Figure 5.68. RMS and average roughness – the volume of hillocks graph. The red triangles are excluded hillocks volume with roughness, and the green dots are included hillocks volume with roughness(for the entire area) for 80x80 μm² images of the B1.
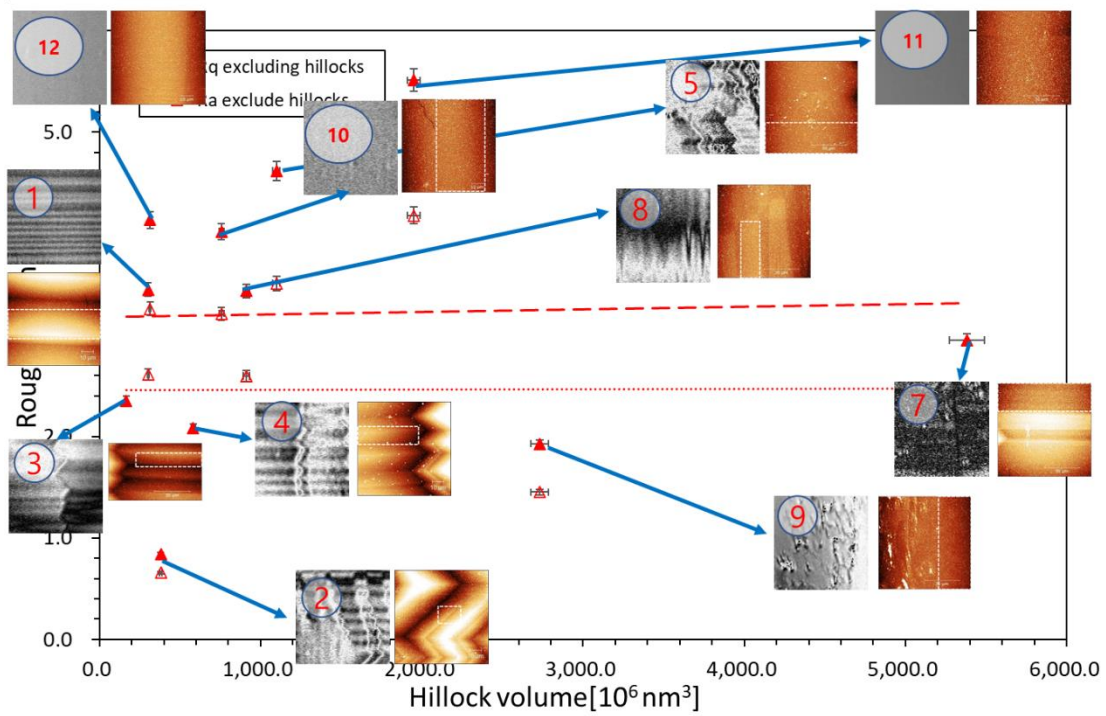
Figure 5.69. RMS and average roughness – the volume of hillocks graph with AFM and 3D Optical Profiler images for excluded hillock area for 80x80 μm^2 images of the B1

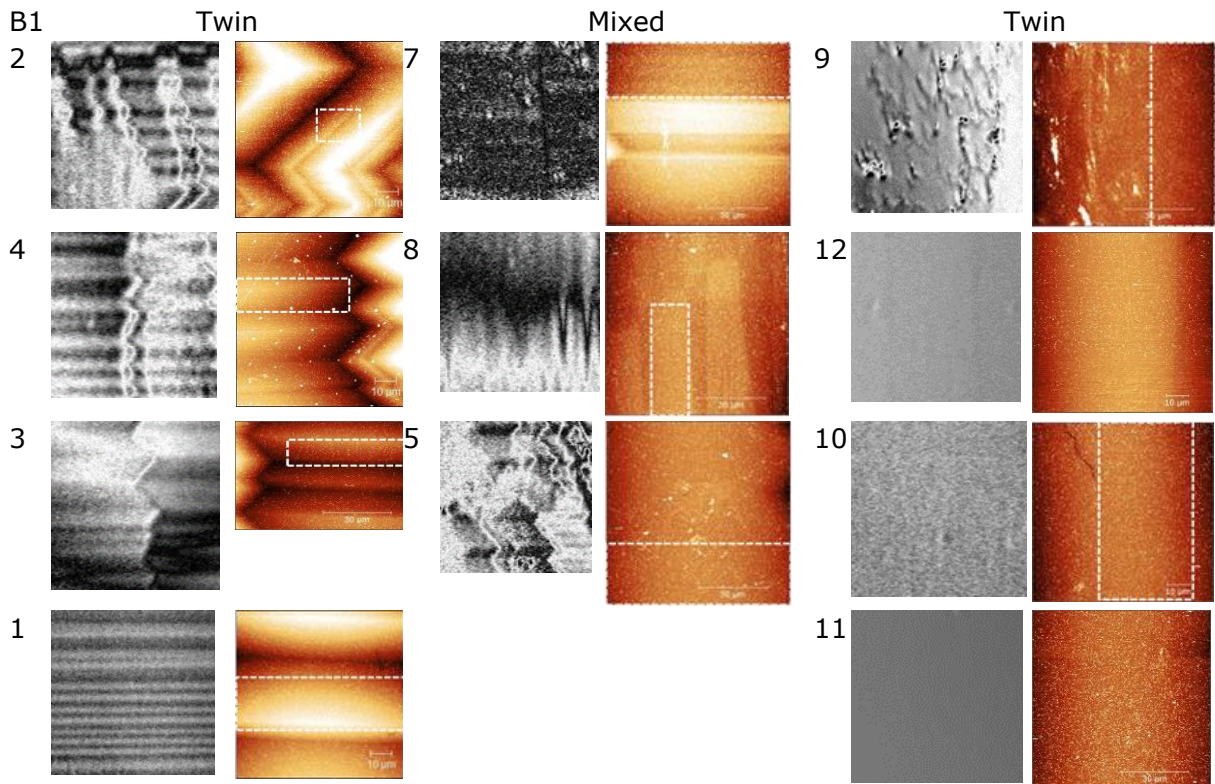Figure. 5.70. The three regions, from low roughness to high roughness, excluded the hillock areas with location numbers of 80x80 μm^2 for B1. Unfortunately, location 9 could not be taken due to the measurement error.

Discussion

I think the fact that there is no trend is repeated again and again; the roughness of 20x20-80x80 μm2 images seems to have no trend in all the factors such as three different regions, hillock volume, excluded hillock areas or an entire region, etc. Although I used only the white dash regions, it might affect the twin or contaminations. Furthermore, I measured only twelve areas (i.e., only four spots in each type), so it is hard to conclude.

5.4.2 The roughness of the B5 sample

The method used in B1 is identical to the one used in B5, which also extracted the roughness with the volume of hillocks and hillock density. B5 does not have the hillocks, yet I plotted the roughness graph with hillock volume and hillock density. Like B1, I also measured twelve regions of four different areas.

Results from the 2x2 μm^2 images

In this section, I will explain the roughness of the 2x2 μm2 images. The first two charts (Figures 5.71 and 5.72) are the roughness with hillock volume and hillock density. Since B5 does not have hillocks, unlike B1, the roughness for excluded hillock areas is similar in all the areas which is around 3nm. Meanwhile, the roughness for the entire images slightly increases when the volume of hillocks goes up. Yet, the roughness rises from just over 3nm to just under 5nm- the gap is pretty minor. I also plotted the roughness – the volume of hillock for the entire regions by attaching 3D Optical Profiler and AFM images. Like B1, the areas do not affect the roughness, and I only figured out that with the increase in hillock volume, the roughness also goes up. To understand roughness more specifically in the three regions, the roughness is plotted by the hillock density with location number in Figure 5.74.
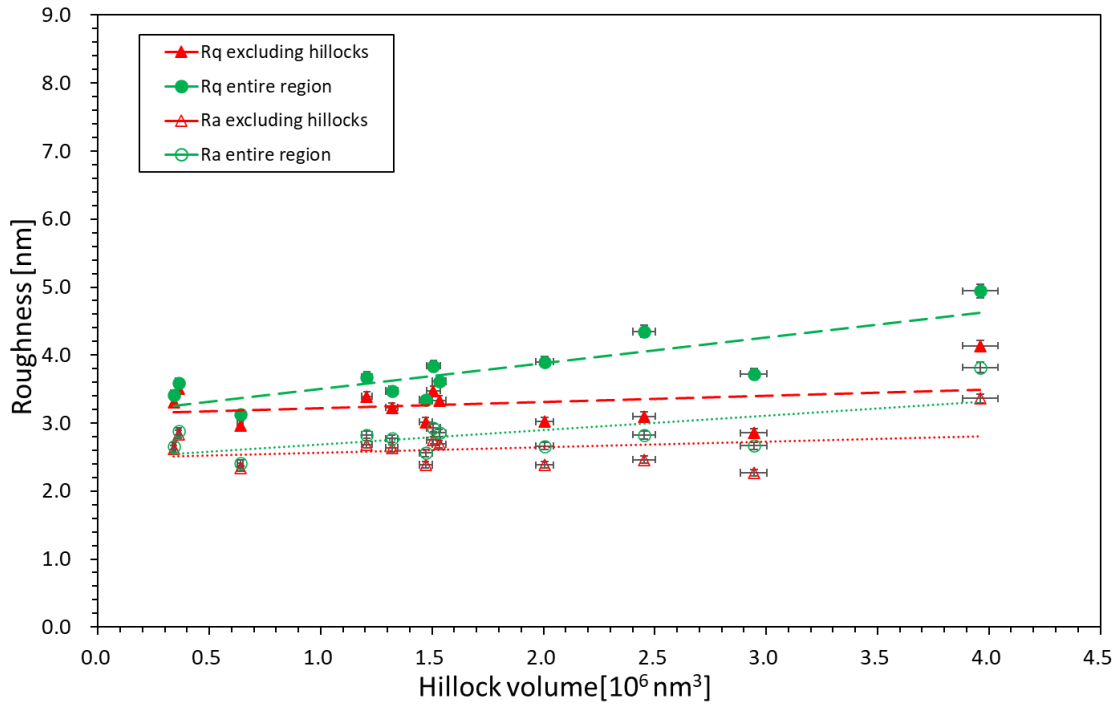
Figure 5.71. RMS and average roughness – the volume of hillocks graph. The red triangles are excluded hillocks volume with roughness, and the green dots are included hillocks volume with roughness(for the entire area) for 2x2 µm² images of the B5.
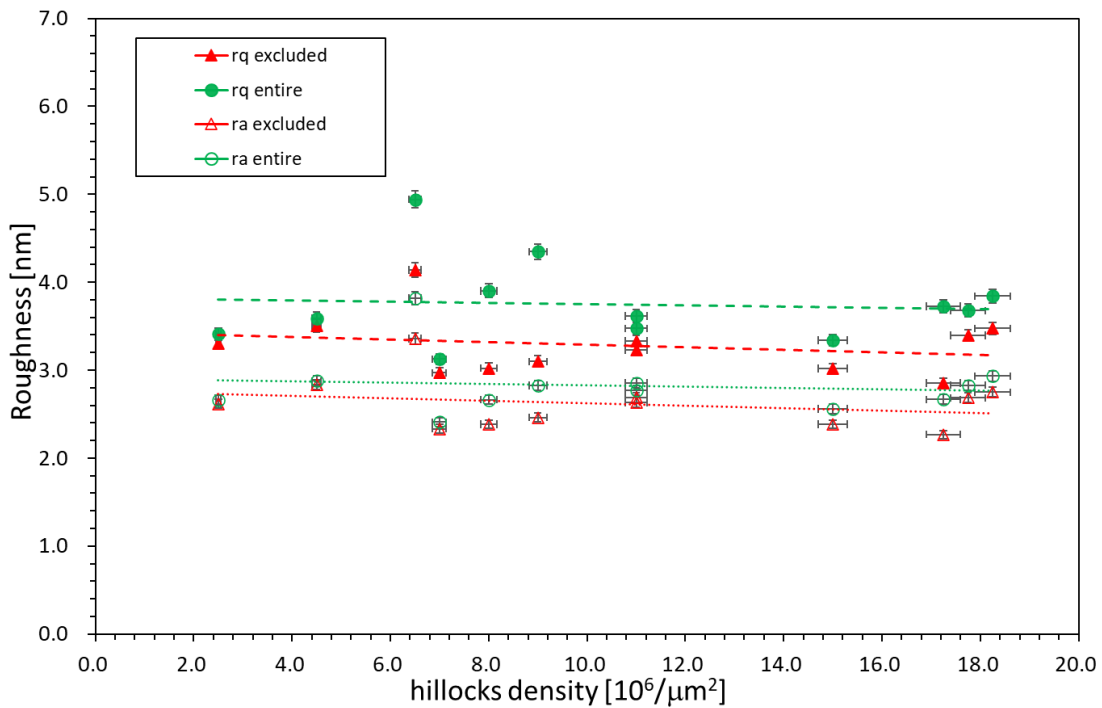

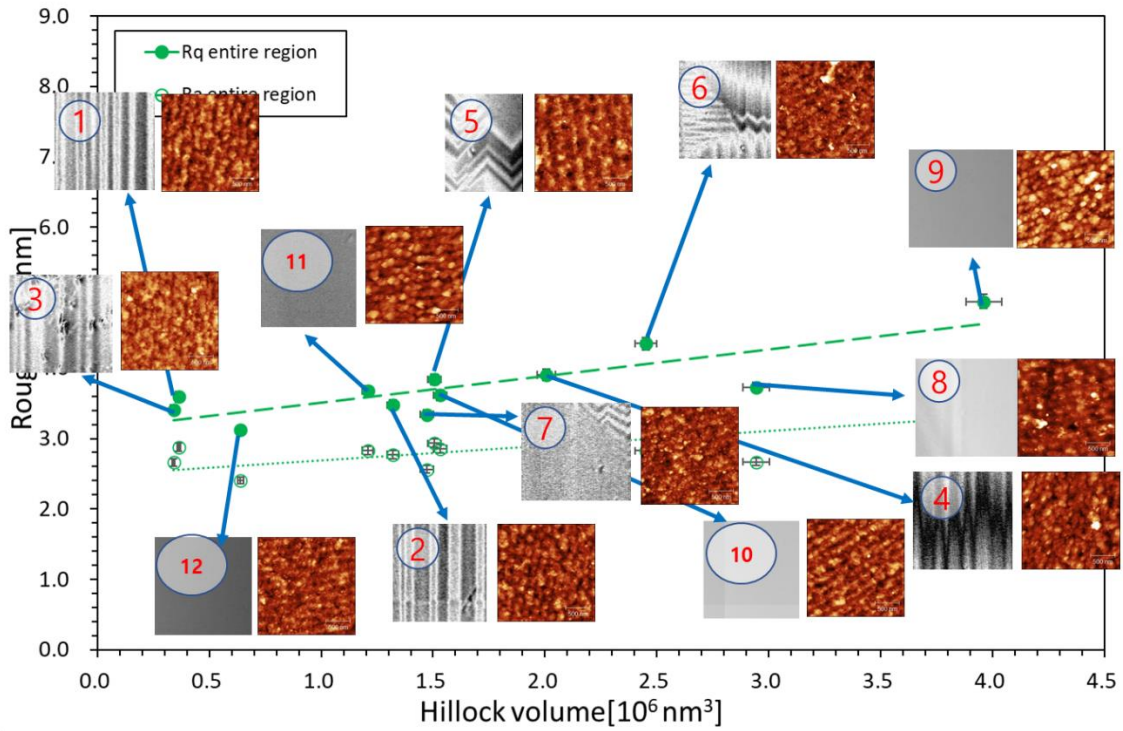Figure 5.72. The roughness with hillock density for 2x2 µm² images of B5

Figure.5.73. RMS and average roughness – the volume of hillocks graph with AFM and 3D Optical Profiler images for the entire area for 2x2 μm^2 images of the B5
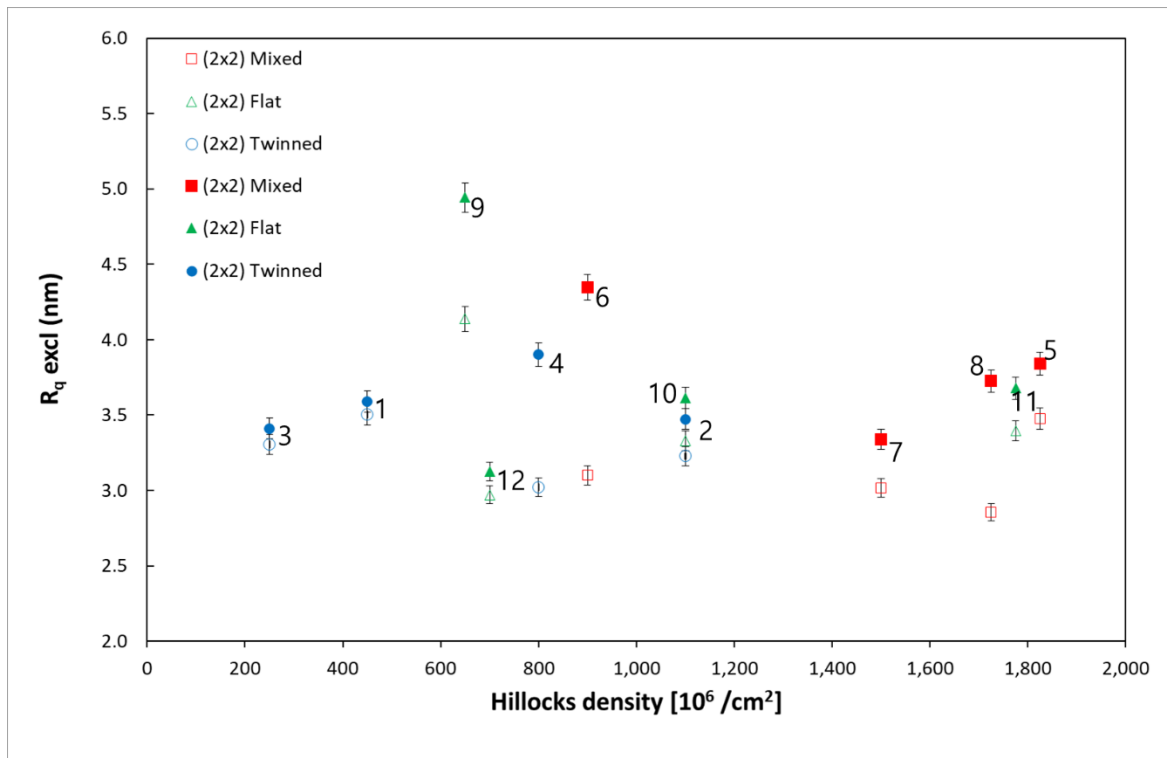

Figure.5.74. The RMS roughness graph with the hillocks density for 2x2 μm^2 of the B5 by the three regions with location number.
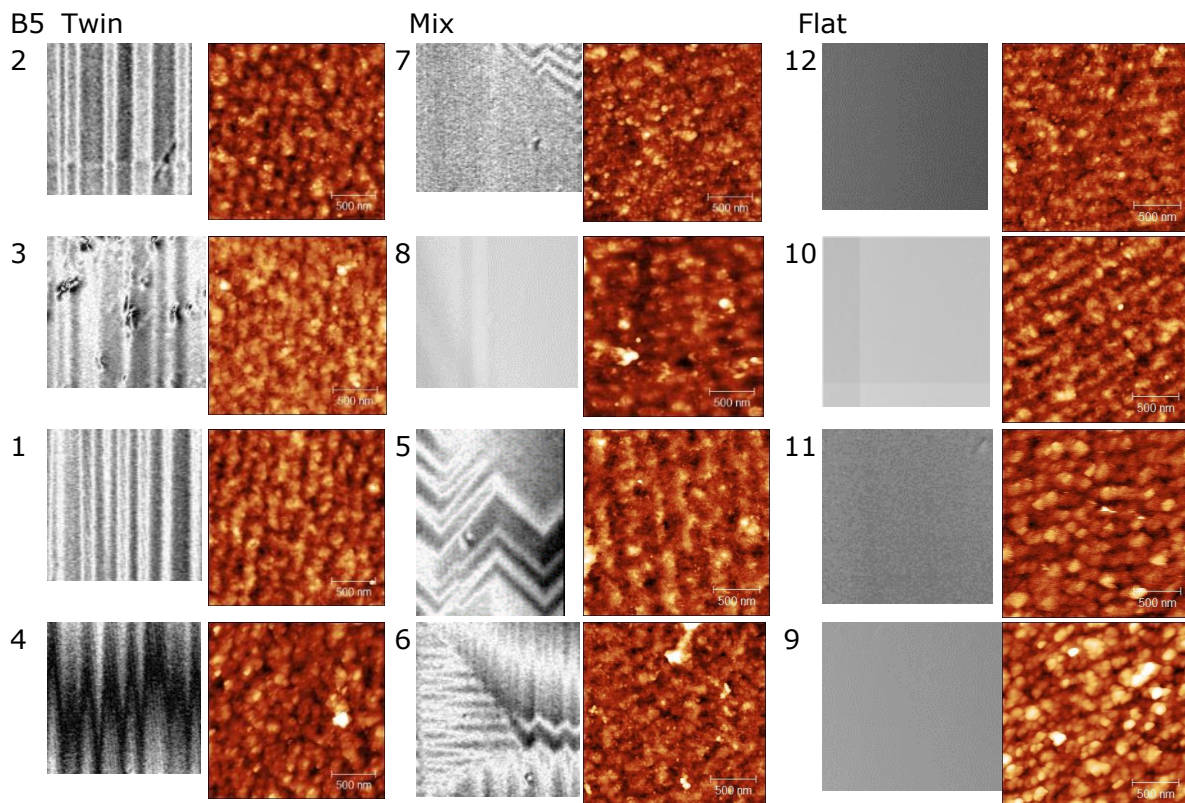
Figure 5.75. The three regions, from low roughness in the top row to high roughness in the bottom row, excluded the hillock areas with location numbers of 2x2 µm^2 for B5.

Discussion

For 2x2 µm^2 for B5, there is no trend except one: increase hillock volume affects the roughness of the entire region. Yet, even this tendency is not outstanding. Since B5 does not have hillocks, the roughness for the whole region and excluded hillock area does not have a big difference. Like B1, I measured only twelve regions; so, it is also tough to conclude.

Results from the 10x10 µm^2 images

Figures 5.76 and 77 are the roughness chart with hillock volume and hillock density for 10x10 µm^2 AFM images. They seem to have a similar tendency with 2x2 µm^2 images, increasing hillock volume, and the entire region's roughness also rises. The other factors , such as the roughness of the excluded hillock areas with the hillock volume, the RMS roughness with hillock density, resembles between 2 and just over 3nm. Like B1, the roughness is calculated inside the white dash lines, since they have different twin domains and are not flat. Since B5 does not have hillocks, I plotted the roughness with the volume of hillocks using the entire regions in Figure 5.78. The roughness increase when the volume of hillocks expands. However, as I have attached the 3D Optical Profiler and AFM images with a location number, the region types cannot affect the roughness. The roughness with hillock density by the three different regions is described in Figure 5.79. The hillock density of the mixed areas is pretty varied, yet it is hard to figure out any tendency.

Figure 5.76. RMS and average roughness – the volume of hillocks graph. The red triangles are excluded hillocks volume with roughness, and the green dots are included hillocks volume with roughness(for the entire area) for 10x10 μm^2 images of the B5.

Figure 5.77. The roughness with hillock density for 10x10 μm^2 images of B5.

Figure 5.78. RMS and average roughness – the volume of hillocks graph with AFM and 3D Optical Profiler images for the entire area for 10x10 μm^2 images of the B5
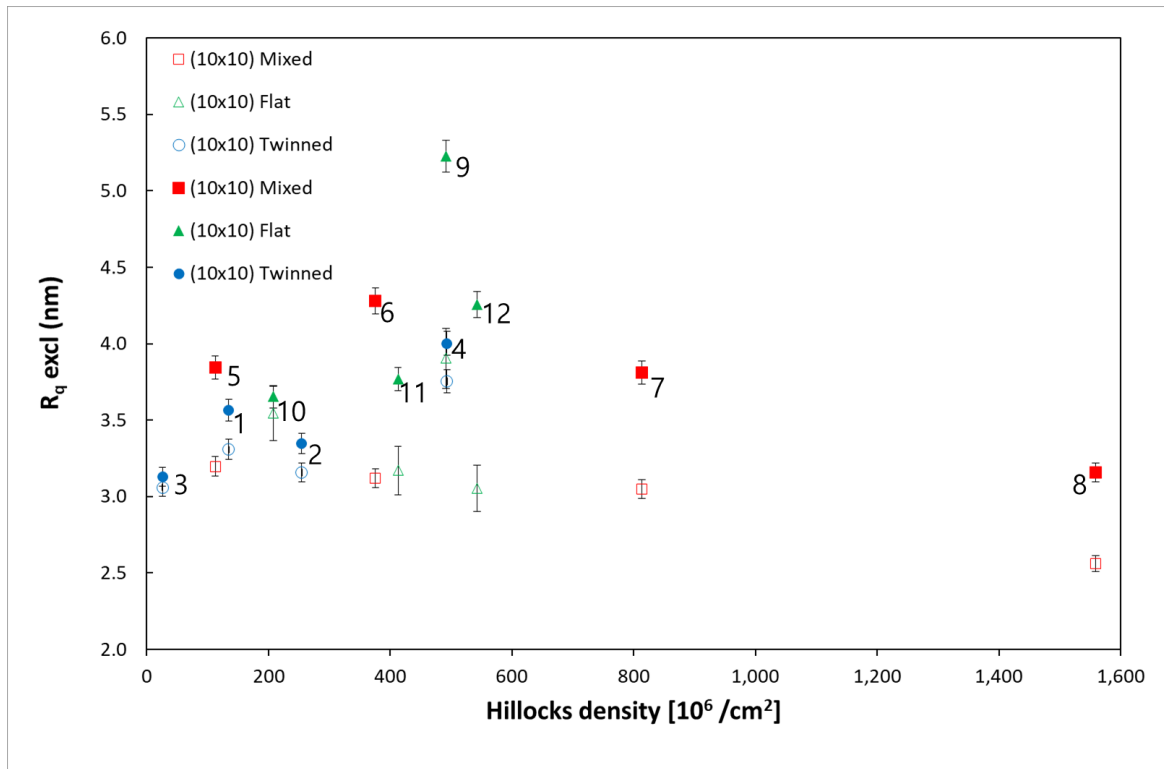
Figure 5.79. The RMS roughness graph with the hillocks density for 10x10 μm^2 of the B5 by the three regions with location number.
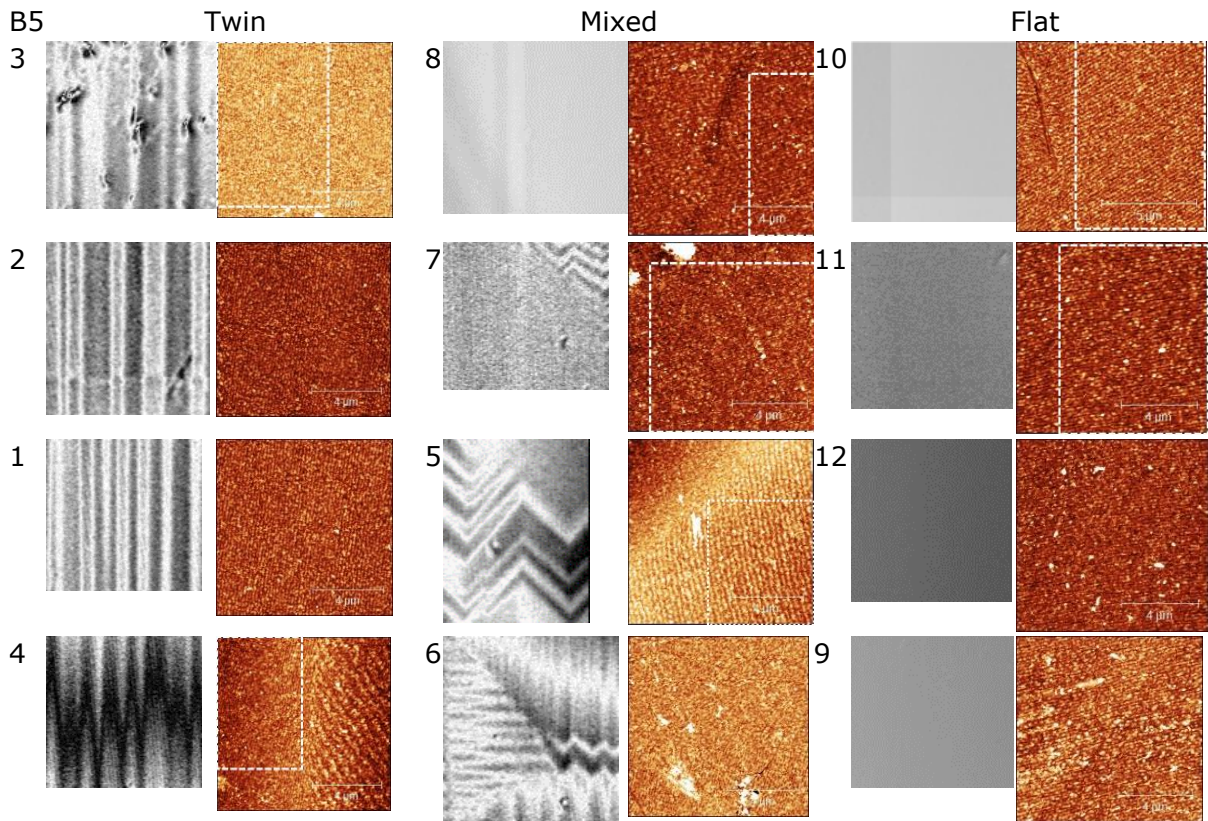
Figure 5.80. The three regions, from low roughness in the top row to high roughness in the bottom row, excluded the hillock areas with location numbers of 10x10 µm^2 for B5.

Discussion

To understand the roughne by the three different areas, I could not find any tendency, like 2x2 µm^2 for B5. This is because, I guess, I used some parts of the regions. I used it partially because the AFM images have different twin domains, and they are not flat. I plotted the roughness by hillock volume and hillock density; however, it also seems to have no trend. If I could have measured more spots by the areas, I might have concluded clearly.

Results from the 20x20 µm^2 to 80x80 µm^2 images

Since it is hard to make a conclusion or figure out any remarkable trend using 2x2 and 10x10 µm^2 images, I will explain the roughnees for 20x20 to 80x80 µm^2 areas. Figures 5.82 to 83 are the roughness for 20x20 µm^2 images. Increasing the hillock volume, the roughness for the entire region also rises like previous results. However, they are more haphazard than 2x2 or 10x10 µm^2 images. In the case of 40x40 µm^2 images, the roughness resembles roughly 2 to over 3 nm in the all the areas. Even though the volume of hillock increase, the roughness stayed the horizontal trend lines. Again, for 80x80 µm^2 images, the roughness increase when the volume of the hillock boosts. Figure 5.87 shows a disparate tendency; the roughness has a comparable value between exclude hillock area and the entire area.
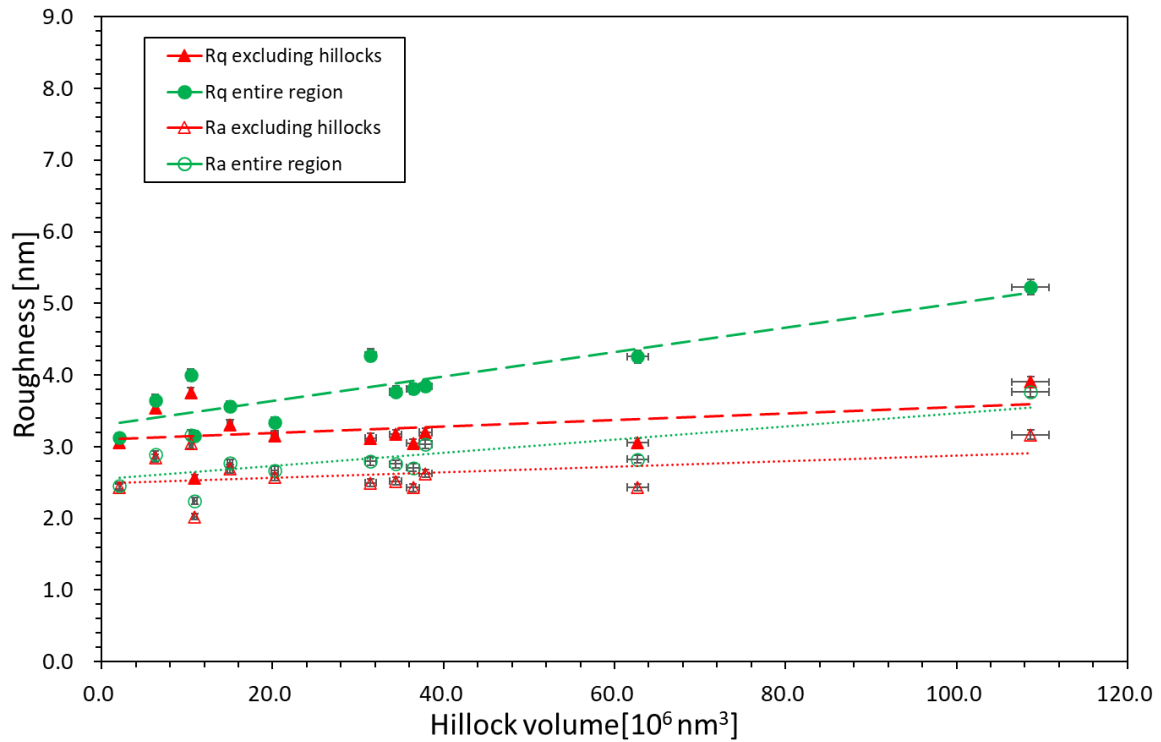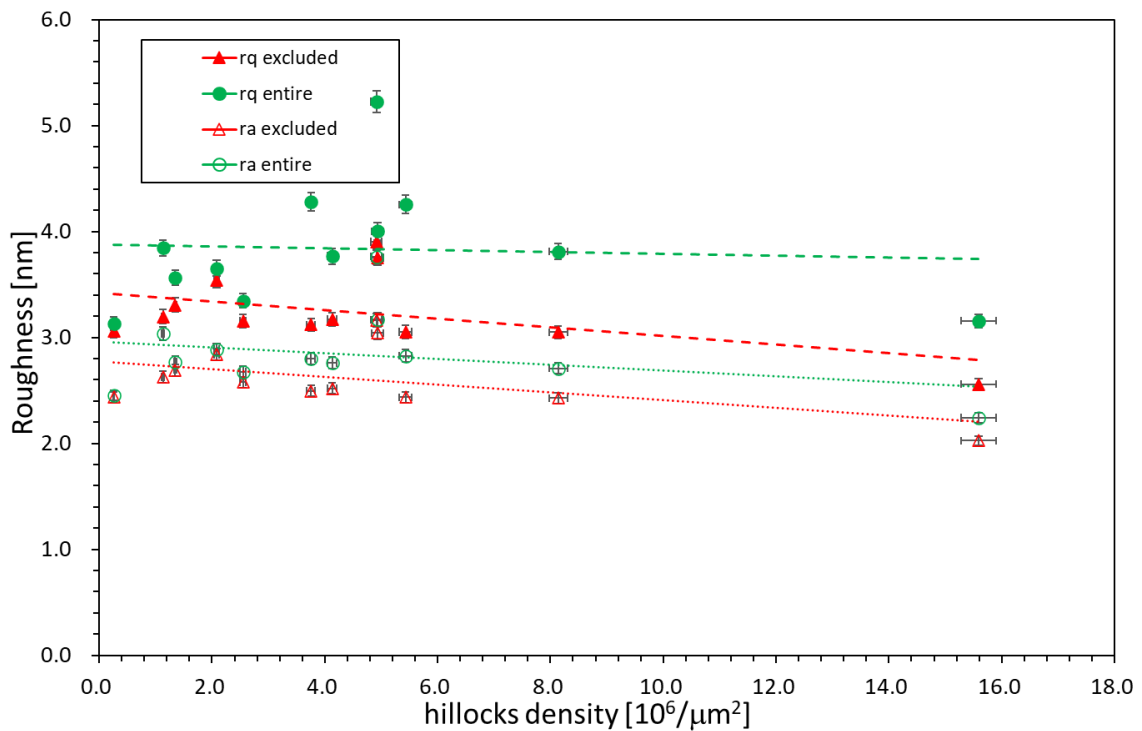
Figure 5.81. RMS and average roughness – the volume of hillocks graph. The red triangles are excluded hillocks volume with roughness, and the green dots are included hillocks volume with roughness(for the entire area) for 20x20 µm² images of the B5.
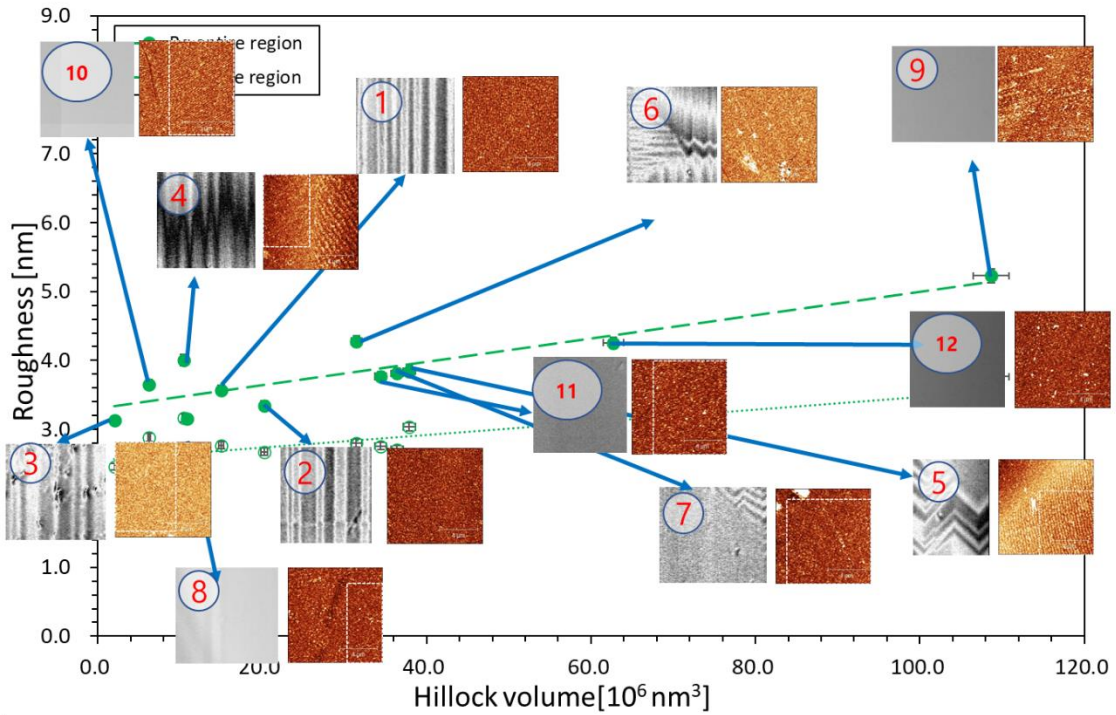

Figure 5.82. RMS and average roughness – the volume of hillocks graph with AFM and 3D Optical Profiler images for the entire area for 20x20 µm² images of the B5

Figure 5.83. The three regions, from low roughness in the top row to high roughness in the bottom row, excluded the hillock areas with location numbers of 20x20 µm^2 for B5.
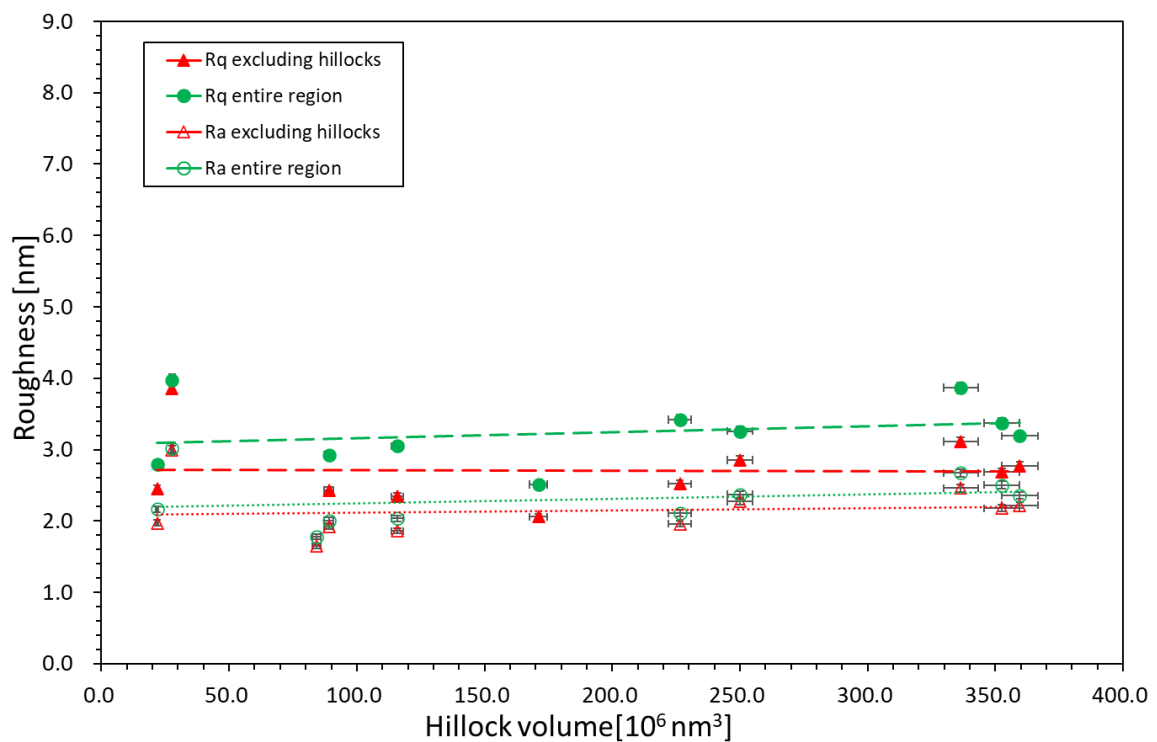
Figure 5.84. RMS and average roughness – the volume of hillocks graph. The red triangles are excluded hillocks volume with roughness, and the green dots are included hillocks volume with roughness (for the entire area) for 40x40 µm^2 images of the B5.
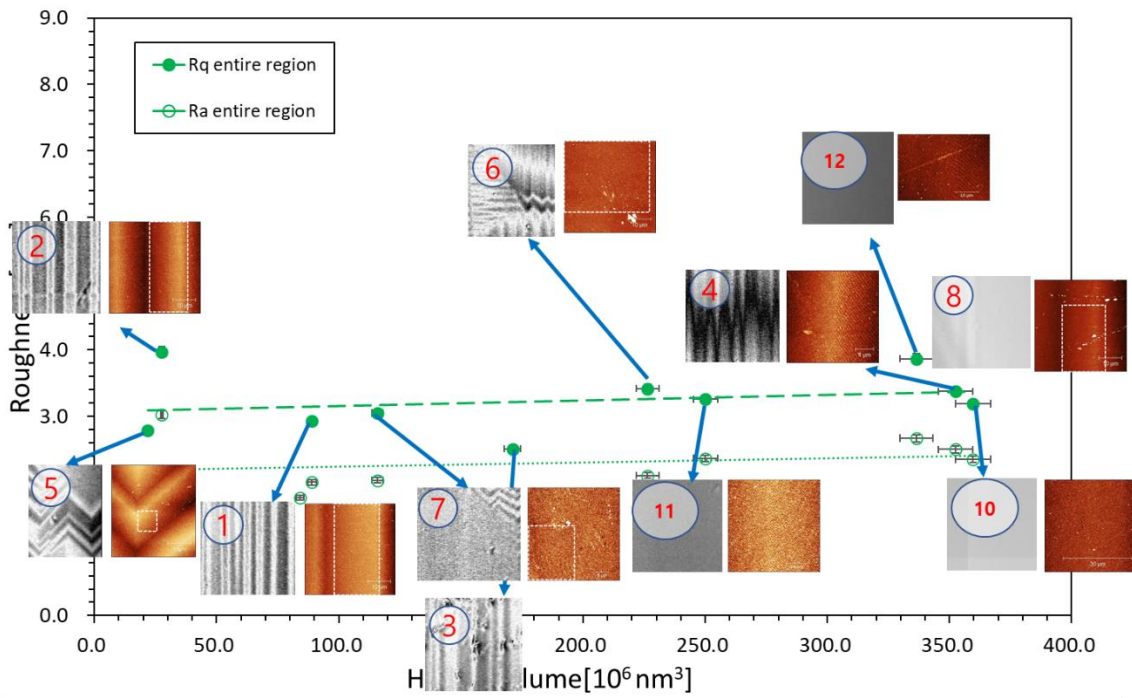
Figure 5.85. RMS and average roughness – the volume of hillocks graph with AFM and 3D Optical Profiler images for the entire area for 40x40 µm^2 images of the B5
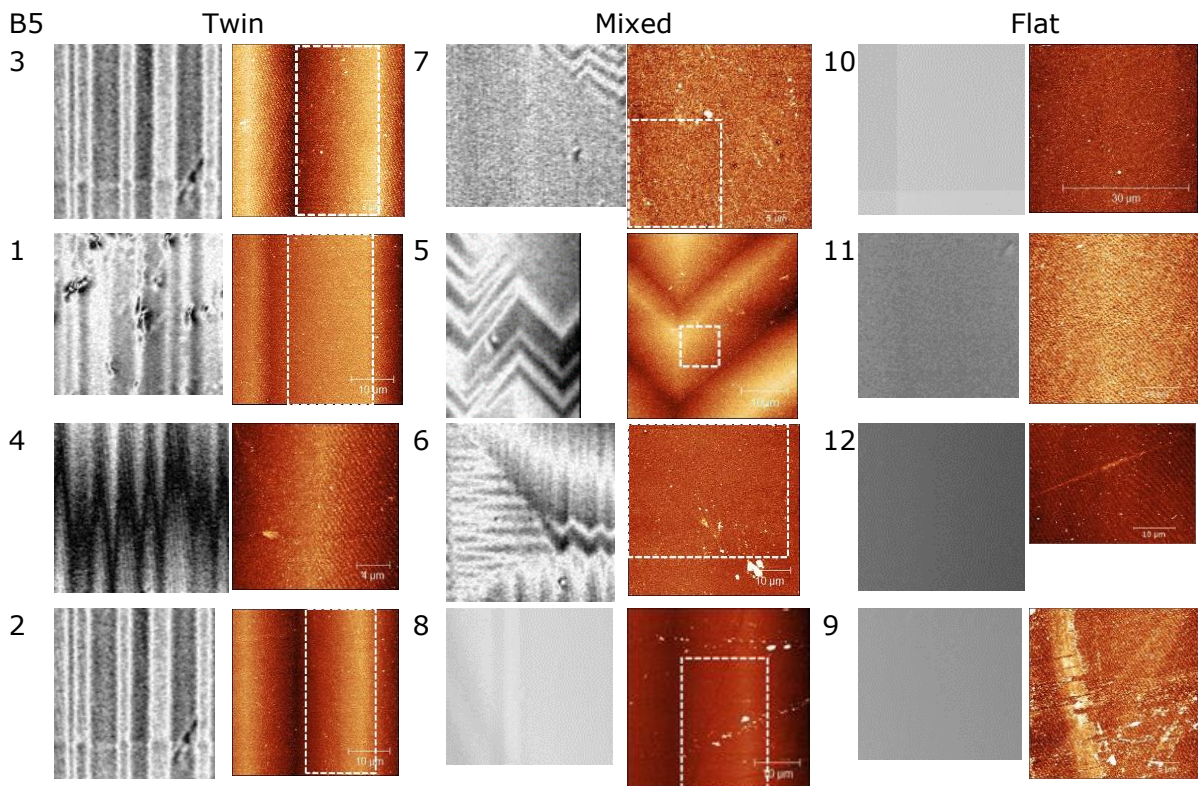
Figure 5.86. The three regions, from low roughness to high roughness, excluded the hillock areas with location numbers of 40x40 µm^2 for B5.
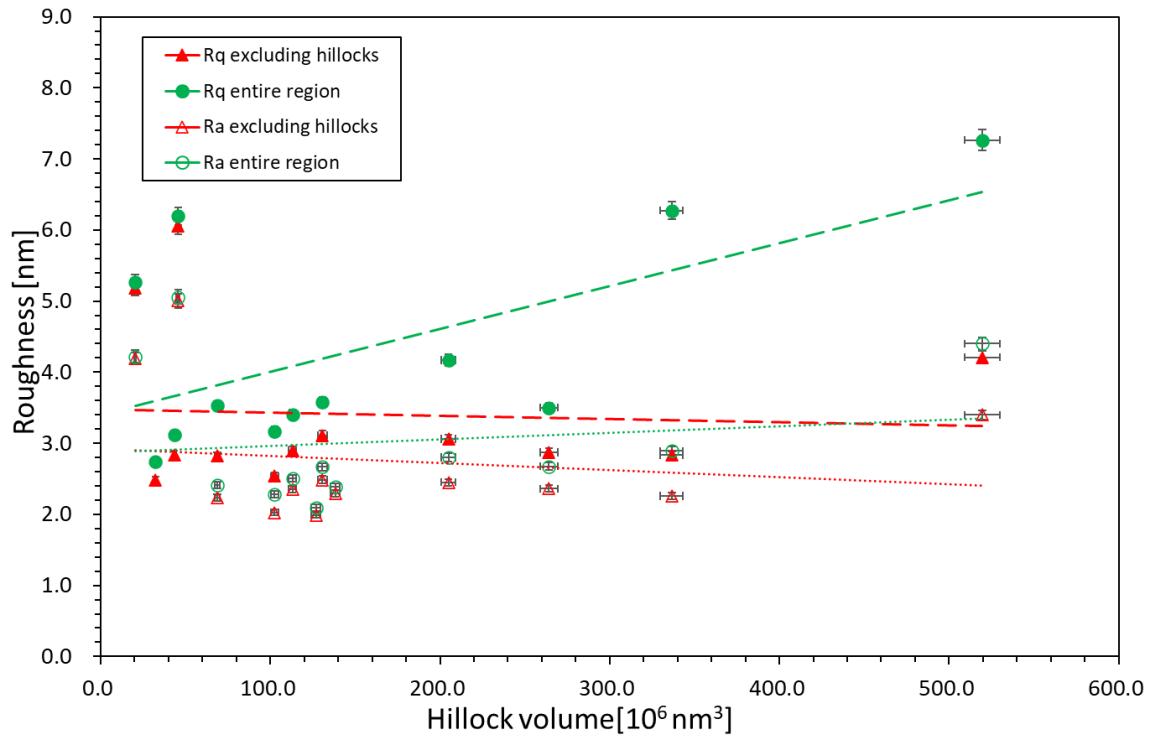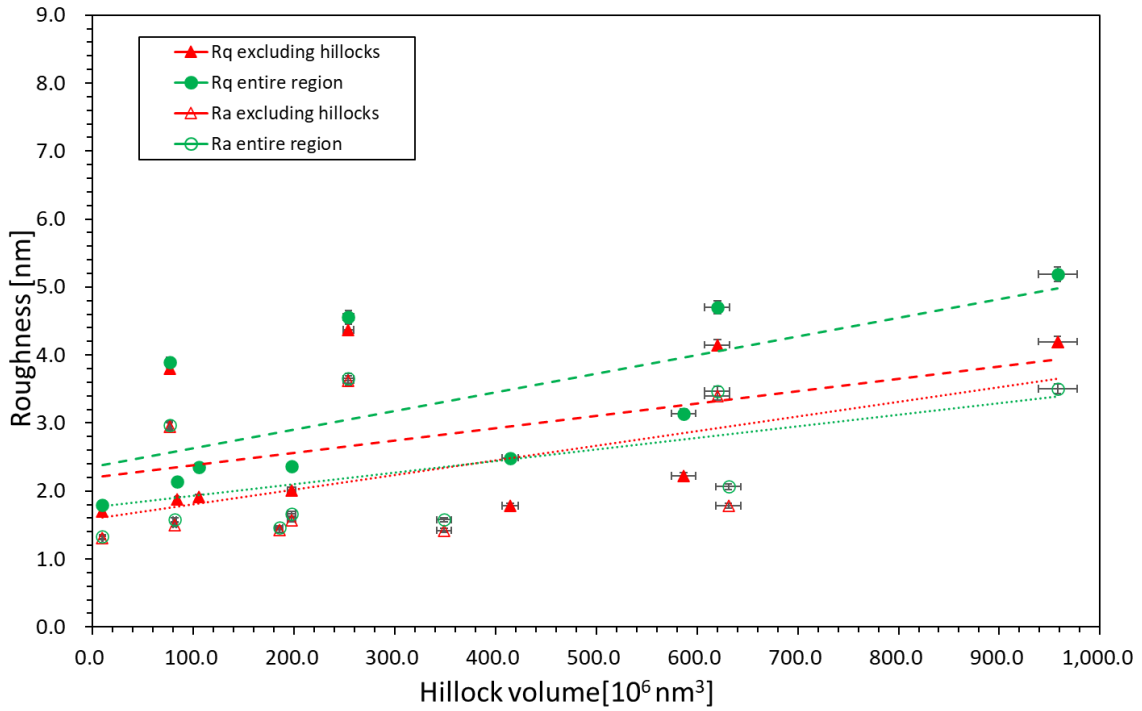
Figure 5.87. RMS and average roughness – the volume of hillocks graph. The red triangles are excluded hillocks volume with roughness, and the green dots are included hillocks volume with roughness(for the entire area) for 80x80 µm² images of the B5.
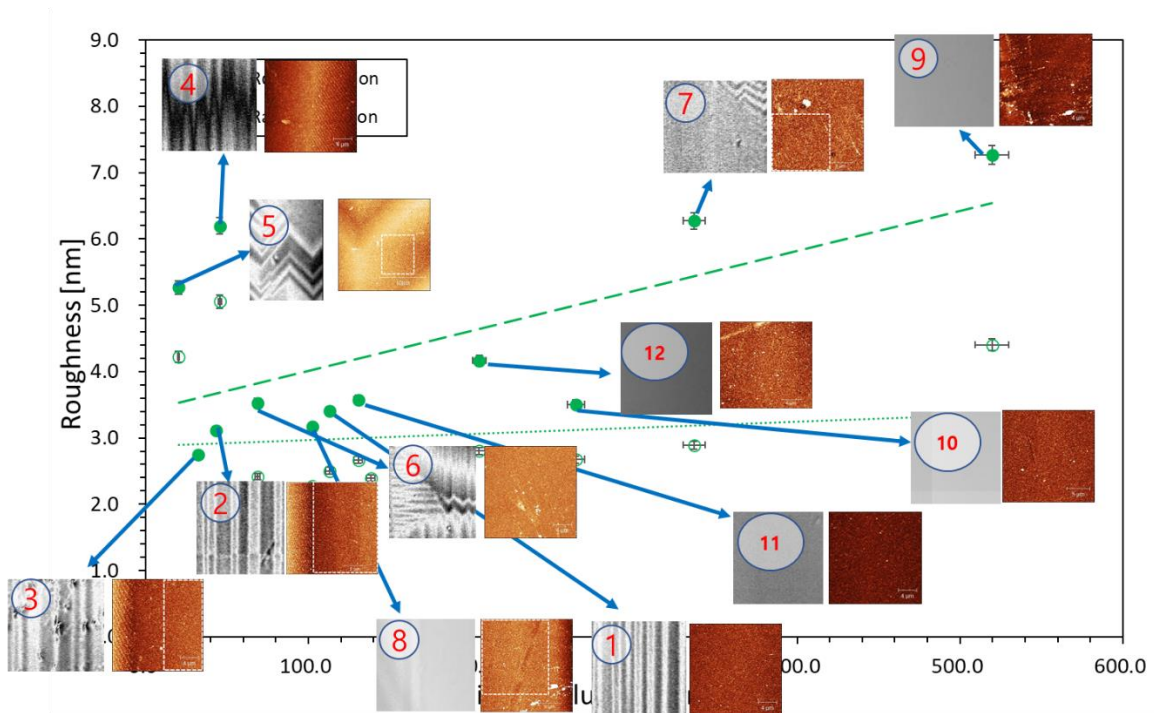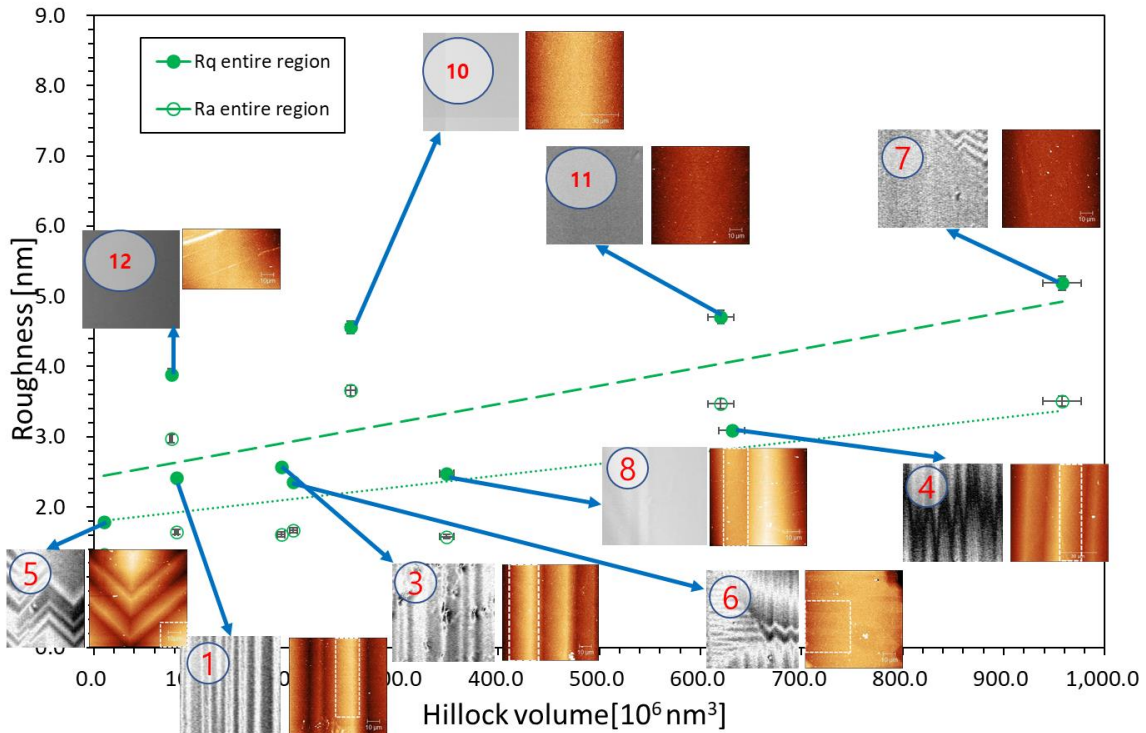

Figure 5.88. RMS and average roughness – the volume of hillocks graph with AFM and 3D Optical Profiler images for the entire area for 80x80 µm² images of the B5
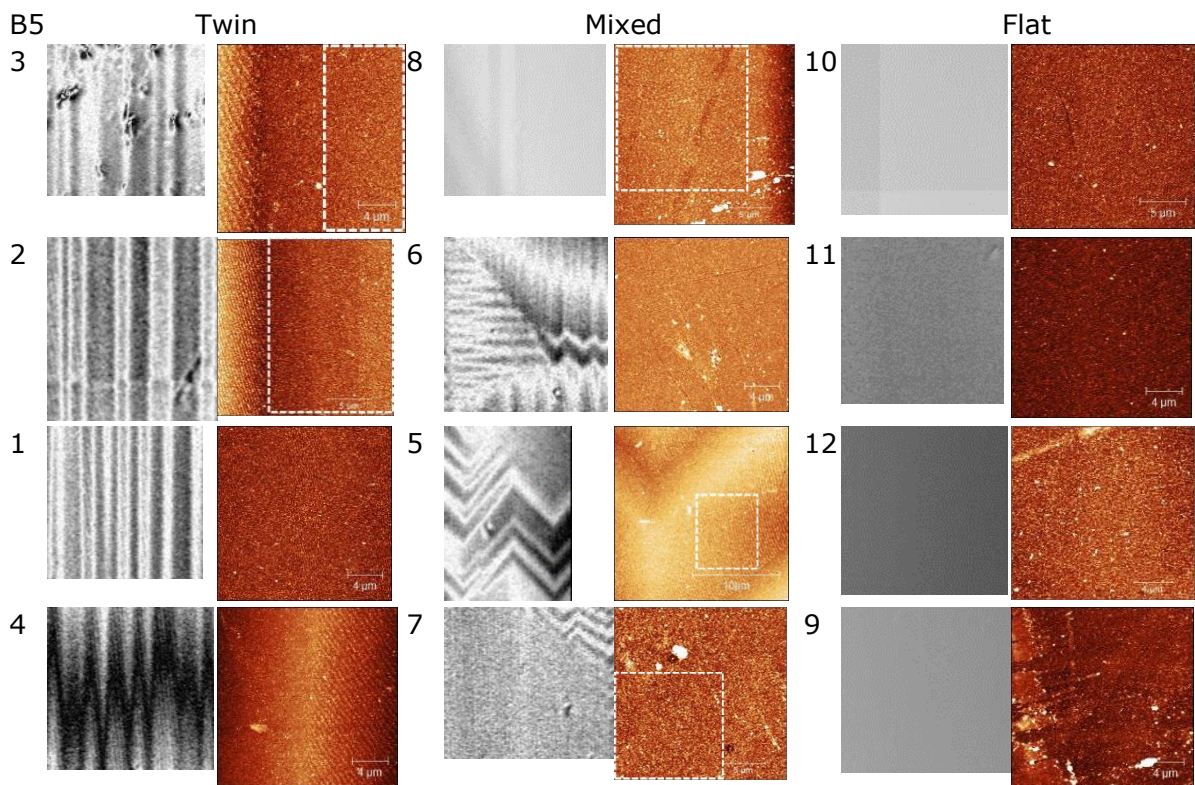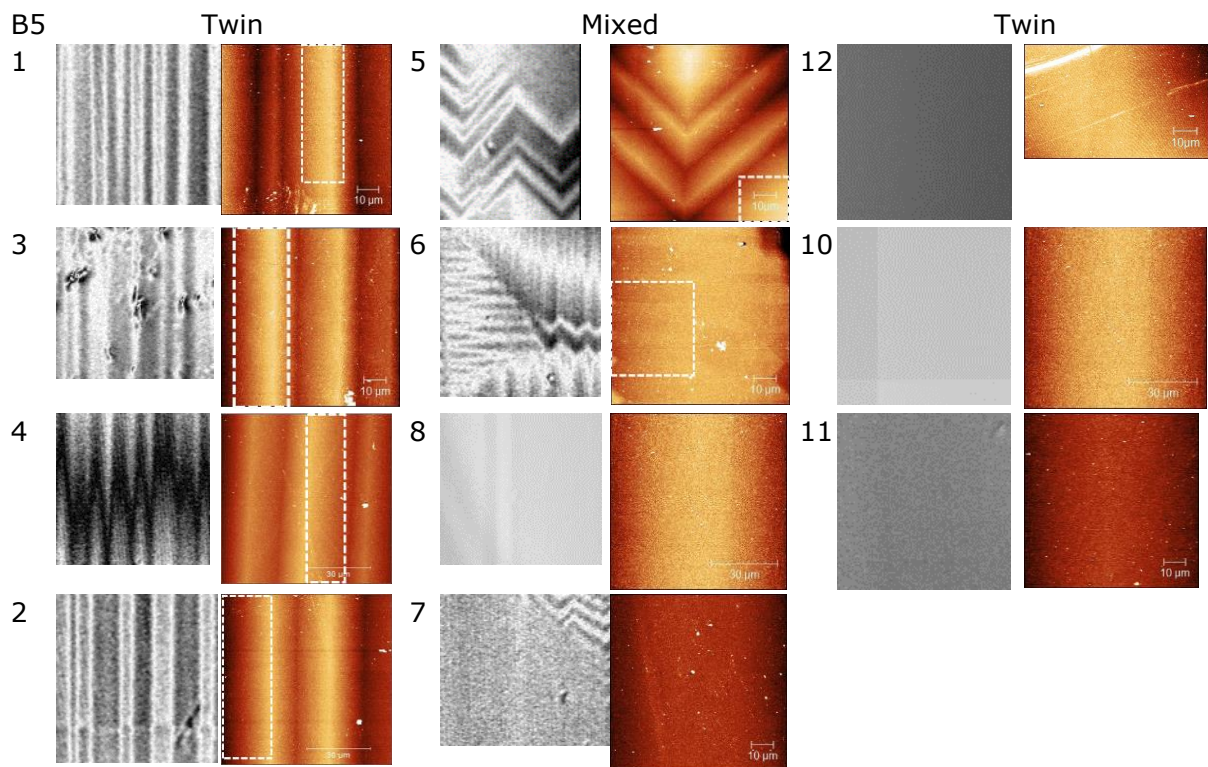
Figure 5.89. The three regions, from low roughness to high roughness, excluded the hillock areas with location numbers of 80x80 µm^2 for B5.

Discussion

Compare to B1, B5 is better-ordered; this means that the roughness of the large AFM image can be affected the LAO substrate. Thus, I could use the AFM images only partially, it might be affected the roughness value (i.e., it is pretty nonprecise) by increasing the large area. Like previous results, it also can not find any trend by the three different areas. I again repeat that if I could have measured more, I might have been able to conclude precisely.

6 Conclusions

All titania films on LAO, STO, sapphire, and silicon were scanned by 3D Optical Profiler, both the full stitching images and the four corners. Only the LAO series has various topography such as twin, flat, and footprint. The other series are pretty flat. From the full stitching image, we can see overview images with contaminations and some scratches, and four corner images show more detail.

To understand more titania films on LAO, we characterized them using AFM and 3D Optical Profiler. The AFM can zoom in on the image, and the 3D Optical Profiler can scan the vast area.

From the 3D Optical Profiler, we are able to see the flat, twin, footprint, the damage caused by polishing, and mixed area in general. Due to repeated re-heating and cooling in the substrate preparation and film deposition, the original twin domains remain, and the surface gets footprints from repeated heating above the critical temperature, in addition to new twin domains forming. According to the four corner images, we could see the damage caused by polishing and some contaminations. Since the films are thin, approximately 300nm for A-series, 600nm for B -series, the surface of the films is affected by the substrate surface. Therefore, the LAO series has varied topography, but the other series are flat.

I also used AFM, to study the nano-scale of the surface for B1 and B5 on LAO. The most significant feature is hillocks for B1. The hillocks are found only in the B1 on LAO. The B1 sample does not have enough oxygen due to the background gas ratio, so instead of fabricated TiO_2, titania suboxide nucleations are created and deposited on the substrate. The hillocks look like a needle or a cluster, and also the size of the hillocks varies. The number of hillocks is pretty similar between $23 \times 10^6/cm^2$ and $38 \times 10^6/cm^2$ in the flat and twin area of B1, yet the mixed areas have a diverse number of hillocks, the smallest and the largest, despite only twelve measurements. On the other hand, B5 on LAO shows the terrace pattern, and this means that B5 is better ordered than B1. We were able to find some striped pattern in B1, excluding the hillocks area, but it is faint. In the 2x2 μm^2 images for B5, the step width is a bit random, however for the 10x10 to 40x40 μm^2 image, the terrace patterns are rather periodic. For both 80x80 μm^2 images in B1 and B5, the images show the twin, flat and mixed area; thus, we are able to recognize that the 3D Optical Profiler images and the AFM images are linked.

I also plotted the roughness as a function of the (total) volume of the hillocks and as a function of hillock density. Because the B1 has hillocks and the B5 does not, I focused on the B1 for excluded hillock areas and the B5 for the entire regions. As increasing the hillock volume, the roughness also goes up from around 1nm to less than 5nm generally. To understand the relation between the roughness and the three different areas such as twin, mixed and flat, I plotted the roughness with hillock density by areas, but it is hard to find trends. Since I investigated only 3-5 locations for each of the three different area types, it is hard to conclude. Based on the data I have, there seems to be a similar variation in roughness <u>within</u> a region type (flat, mixed, or twin) as <u>between</u> the regions, meaning that there is no clear dependence on roughness with the region type.

7 Future work suggestions

Above all, I would like to add more measurements on more spots using AFM. For each B1 and B5 on LAO, the locations where I measured were only 12 regions. Even though I measured three different types of twin, mixed, and flat areas, they were not enough to decide the conclusion of their properties precisely. If I had been able to see more regions for each area, like more than ten areas, it would have been easier to comprehend the features of topography, trends, or properties of morphologies. To increase the accuracy of the results, measurement tools – 3D Optical Profiler and AFM- calibration and the error need to be more distinct.

For the fabrication, the deposition parameter has a significant gap in the ratio of ambient gases among the series. For instance, in B1 to B5 oxygen and argon ratio, there is no half; in other words, B2, B3, and B4, the oxygen ratio is 1, 2, and 10 %. Thus, it would be easier to understand the effect of the ambient gases on the surface if the oxygen and argon ratio is 50:50 so that we might understand more topography, stochiometry, etc. A series can also fabricate identical oxygen and argon ratio conditions and various pressures, or the same force with different oxygen and argon ratio would be attractive, leading to a better understanding of the effect of ambient gases and of the trends in the series.

In the case of measurement, it would be easier to comprehend and prove how the substrates affect the films if they are measured together. Firstly, if I could measure all the series using AFM, I would be able to understand how they changed the topography without twins, depending on substrates, etc.

Compared to the previous work, some results are disparate. For example, Sohaib's work was focused mainly on all the substrates of LAO before film deposition. On the other hand, I measured only B5 LAO substrate by the AFM at one location, and it is after the deposition. Therefore, the results of previous work and mine are different. Consequently, I could not be sure of the reasons why-whether because of the deposition or other reasons.

For 3D Optical Profiler, I could not obtain the thickness from the data because the surface area is pretty vast. So, I spent time on various methods such as line profiling or measuring the gap of the films and substrate height. However, I could not decide on the thickness; thus, it would be nice to determine it. Significantly, the B1 on the LAO has only one result; since it is too metallic, VASE cannot figure out the thickness. So, not only by 3D Optical Profiler but also using other instruments can help to make decisions about the thickness.

I was not able to describe the results for the Raman spectroscopy. Initially, I did experiments; however, I did not notice any differences among twin, mixed and flat areas. I was able to measure only five regions on LAO and did not use the mapping function. Therefore, the results seem almost identical. Due to a shortage of time, despite the measurement made, I decided not to explain the Raman spectroscopy results. Therefore, if I had been able to measure more and use the mapping function, it would have been able to prove the composition of the films more specifically.

References

1.	Dastagir, S., *Surface studies of LaAlO3 substrates for TiO2 thin film deposition*. 2020, Norwegian University of Science and Technology: Trondheim.

2.	Andrew Ciavarella, D.C., Peter Stott, Sarah Kew, Sjoukje Philip, Geert Jan van Oldenborgh, Amalie Skålevåg, Philip Lorenz, Yoann Robin, Friederike Otto, Mathias Hauser, Sonia I. Seneviratne, Flavio Lehner, Olga Zolina *Siberian heatwave of 2020 almost impossible without climate change*. 2020. [cited 2021 2021-02-10]; Available from: https://www.worldweatherattribution.org/siberian-heatwave-of-2020-almost-impossible-without-climate-change/.

3.	 [cited 2021 1.Feb]; Available from: www.bruker.com/ContourGT.

4.	Hansen, K. *Excessive Monsoon Rains Flood Asia*. 2020 [cited 2021 2021-02-11]; Available from: https://earthobservatory.nasa.gov/images/147006/excessive-monsoon-rains-flood-asia.

5.	 [cited 2021 2021-02-12]; Available from: https://www.who.int/news-room/air-pollution.

6.	Mousavi, S.M., E.S. Mostafavi, and P. Jiao, *Next generation prediction model for daily solar radiation on horizontal surface using a hybrid neural network and simulated annealing method.* Energy Conversion and Management, 2017. **153**: p. 671-682.

7.	*RENEWABLE CAPACITY STATISTICS 2021*. 2021, Abu Dhabi: International Renewable Energy Agency.

8.	Geisz, J.F., et al., *Six-junction III–V solar cells with 47.1% conversion efficiency under 143 Suns concentration.* Nature Energy, 2020. **5**(4): p. 326-335.

9.	Ohnishi, T., H. Koinuma, and M. Lippmaa, *Pulsed laser deposition of oxide thin films.* Applied Surface Science, 2006. **252**(7): p. 2466-2471.

10.	Eason, R., *Pulsed laser deposition of thin films : applications-led growth of functional materials*. [2nd ed.]. ed. 2007, Hoboken, N.J: Wiley-Interscience.

11.	Stafe, M., A. Marcu, and N.N. Puscas, *Pulsed Laser Ablation of Solids: Basics, Theory and Applications*. 2014 ed. Springer Series in Surface Sciences. Vol. 53. Berlin, Heidelberg: Berlin, Heidelberg: Springer Berlin Heidelberg.

12.	Heimdal, C.P.J., *Pulsed Laser Deposition of Zinc Sulfide Thin Films on Silicon*, in *Physics*. 2014, Norwegian University of Science and Technology: Trondheim. p. 41.

13.	Bao, Q., et al., *Pulsed laser deposition and its current research status in preparing hydroxyapatite thin films.* Applied Surface Science, 2005. **252**(5): p. 1538-1544.

14.	Hannaas, E., *Initial Studies of Strontium Titanate Substrates and Room Temperature Deposited Titanium Dioxide Thin Films*, in *Physics*. 2017, Norwegian University of Science and Technology: Torndheim.

15.	Posusta, R. *Correlating Advanced 3D Optical Profiling Surface Measurements to Traceable Standards*. 2016.

16.	Binnig, G., C.F. Quate, and C. Gerber, *Atomic Force Microscope.* Physical Review Letters, 1986. **56**(9): p. 930-933.

17.	R.R.L. De Oliveira, D.A.C.A., T.G.S. Cruz, F.M. Yamaji and F.L. Leite, *Measurement of the Nanoscale Roughness by Atomic Force Microscopy: Basic Principles and Applications*. 2012.

18.	Hurley, D. *Improved Surface Characterization with AFM Imaging*. 2017 [cited 2021 2021-04-03]; Available from: https://www.techbriefs.com/component/content/article/tb/supplements/pit/features/applications/27833.

19.	Krupski, K., et al., *Optimisation of anatase TiO2 thin film growth on LaAlO3(0 0 1) using pulsed laser deposition.* Applied Surface Science, 2016. **388**: p. 684-690.

20.   Kawanowa, H., et al., *Structure analysis of LaAlO3(001) surfaces by low energy neutral scattering spectroscopy.* Surface Science, 2002. **506**(1): p. 87-92.

21.   Bueble, S., et al., *Influence of the ferroelastic twin domain structure on the {100} surface morphology of LaAlO3 HTSC substrates.* Surface Science, 1998. **400**(1): p. 345-355.

22.   Landmann, M., E. Rauls, and W.G. Schmidt, *The electronic structure and optical response of rutile, anatase and brookite TiO2.* Journal of Physics: Condensed Matter, 2012. **24**(19): p. 195503.

23.   Rizwan, M., et al., *A review on perovskite lanthanum aluminate (LaAlO3), its properties and applications.* Materials Research Express, 2019. **6**(11): p. 112001.

24.   Bilde-Sørensen, J.B., *Tem method for identification of domains in materials which undergo a Pm3m → R3c or R3c phase transition.* physica status solidi (a), 1979. **55**(2): p. 747-750.

25.   Yao, G.-D., et al., *Synchrotron x-ray topography studies of twin structures in lanthanum aluminate single crystals.* Journal of Materials Research, 1992. **7**(7): p. 1847-1855.

26.   Dudley, M. and G.D. Yao, *Synchrotron topography of phase transitions in perovskite-like crystals.* Journal of Physics D: Applied Physics, 1993. **26**(4A): p. A120-A125.

27.   *Changing crystal orientation: SrTiO3 [110]*. 2019 [cited 2021-06-24; Available from: https://er-c.org/barthel/drprobe/example-celfile-sto110.html#ref01.

28.   Ngai, J.H., et al., *Achieving A-Site Termination on La0.18Sr0.82Al0.59Ta0.41O3 Substrates.* Advanced Materials, 2010. **22**(26-27): p. 2945-2948.

29.   Woo, S., et al., *Surface properties of atomically flat poly-crystalline SrTiO3.* Scientific Reports, 2015. **5**(1): p. 8822.

30.   Dolgaev, S.I., et al., *Fast etching of sapphire by a visible range quasi-cw laser radiation.* Applied Surface Science, 1996. **96-98**: p. 491-495.

31.   Kumar, P., et al., *Experimental characterization of plane and conformal hydrodynamic polishing of machined single crystal sapphire.* Manufacturing Letters, 2013. **1**(2): p. 70-73.

32.   Niu, X.-h., et al., *Method of surface treatment on sapphire substrate.* Transactions of Nonferrous Metals Society of China, 2006. **16**: p. s732-s734.

33.   *About Silicon*. [cited 2020 2020-06-23].

34.   Fujishima, A. and K. Honda, *Electrochemical Photolysis of Water at a Semiconductor Electrode.* Nature, 1972. **238**(5358): p. 37-38.

35.   Brandt, I.S., et al., *Influence of substrate on the structure of predominantly anatase TiO2 films grown by reactive sputtering.* RSC Advances, 2018. **8**(13): p. 7062-7071.

36.   Oi, L.E., et al., *Recent advances of titanium dioxide (TiO2) for green organic synthesis.* RSC Advances, 2016. **6**(110): p. 108741-108754.

37.   Zhang, J., et al., *New understanding of the difference of photocatalytic activity among anatase, rutile and brookite TiO2.* Physical Chemistry Chemical Physics, 2014. **16**(38): p. 20382-20386.

38.   Li, J., et al., *Contributions of oxygen vacancies and titanium interstitials to band-gap states of reduced titania.* Physical Review B, 2018. **97**(4): p. 041403.

39.   Samat, M.H., et al., *Hubbard U calculations on optical properties of 3d transition metal oxide TiO2.* Results in Physics, 2016. **6**: p. 891-896.

40.   Lin, Y., et al., *Nucleation dynamics of nanostructural TiO2films with controllable phases on (001) LaAlO3.* Nanotechnology, 2013. **25**(1): p. 014014.

41.   Petr Klapetek, D.N.c., and Christopher Anderson, *Gwyddion user guide*. 2014, GNU General Public License.

42.   *Understanding Surface Finish*. [cited 2021 2021-08-14]; Available from: https://www.destinytool.com/surface-finish.html.

43.   *The Surface Roughness Analysis Blog*. 2021 2021-08-15]; Available from: https://michmet.com/surface-roughness-analysis-average-roughness-basics.htm.

44.   Jorge, M.R., *Potential oxide-based intermediate band materials: fabrication and photoemission studies*. 2020, Norwegian University of Science and Technology: Trondheim.

45.   Xu, B., et al., *Structures, preparation and applications of titanium suboxides.* RSC Advances, 2016. **6**(83): p. 79706-79722.

46.   Wang, G., et al., *Synthesis, microstructural characterization, and electrochemical performance of novel rod-like Ti4O7 powders.* Journal of Alloys and Compounds, 2017. **704**: p. 18-25.